Photophysical studies of Zinc Phthalocyanine-Silica nanoparticles Conjugates

A thesis submitted in fulfillment of the requirements for the degree of

DOCTOR OF PHILOSOPHY

Of

RHODES UNIVERSITY

By

ADEDAYO FASHINA

January 2015

Dedication

To God:

Who is able to do exceedingly abundantly above all that we could ever ask or think, according to his power that is at work within us. Eph. 3:20.

And my Parents:

Mr. and Mrs. Fashina

Acknowledgments

I would like to appreciate God, "who declares the end from the very beginning", for his grace, strength and favor during this season.

My genuine appreciation goes to Distinguished Prof. Tebello Nyokong for giving me the opportunity to study under her tutelage. Thank you very much for all the encouragements and the opportunities you availed me.

I would also want to thank Dr. Edith Antunes for all her support and kindness.

To my family and folks, thank you very much for your constant calls and words of encouragement during this period.

To Dawi, Tendai, Fifi, Rosa, Toks, Tim, Tope, Favor, Seyi, Sunday, Stephen and Dolu, thank you very much for the friendship, kindness and gifts.

To my S22 colleagues, thank you for very much for the interesting times we had laughing and working in the Lab. Edith Amuhaya, Kay, Rachel, Papa Edward, Jess, Sarah, Phindi, I appreciate everyone of you.

I also appreciate the Chemistry department of Rhodes University, all staff members (especially Gail, Papa Francis, Bongani and Andre) and all the postgraduate students.

I also like to thank the Electron microscopy unit (EMU) especially Marvin and Shirley for their friendship.

Abstract

This thesis reports on the synthesis and characterization of both symmetrical and asymmetrical Zinc phthalocyanine complexes. The complexes contained groups such as carboxylic, amino and alkyne for covalent grafting to the surface of silica nanoparticles. The use of symmetrical and asymmetrical complexes was geared towards comparing the non-specific binding of the symmetrical complexes to the specific binding observed in the asymmetrical complexes. The complexes were also doped within the silica matrix and compared to the surface grafted conjugates. The complexes and the conjugates were well characterized with a variety of techniques.

The fluorescence lifetimes of the phthalocyanine complexes containing either terminal carboxylic groups or an alkyne group showed a mono-exponential decay while the amino containing phthalocyanine complexes gave a bi-exponential decay. A similar trend was observed for their respective conjugates.

Some of the conjugates of the asymmetrical complexes showed a decrease in fluorescence lifetimes and a corresponding decrease in fluorescence quantum yields. The fluorescence quantum yields for all the symmetrical complexes studied showed either an improvement or retained the luminescence of the grafted phthalocyanine complex. Most of the conjugates showed a faster intersystem crossing time in comparison to the complexes alone. The grafted or doped conjugates containing symmetrical phthalocyanine complexes with carboxyl groups showed improvements both in fluorescence and triplet quantum yields. All the conjugates except two showed an increase in triplet lifetimes when compared to their respective phthalocyanine complexes.

Optical nonlinearities of nine of the phthalocyanine complexes were studied and all the complexes showed characteristic reverse saturable absorption behavior. Complex **10** showed the most promising optical limiting behavior.

The aggregation and dissolution studies of the conjugates were also carried out in a simulated biological medium and the silicon level detected was noticed to have increased with incubation time.

CONTENT

Content

Content

List of Abbreviations

ALF	=	Artificial lysosomal fluid
APTES	=	3-aminopropyltriethoxysilane
BET	=	Brunauer-Emmet-Teller
DCC	=	Dicyclohexylcarbodiimide
DCM	=	Dichloromethane
DMAP	=	Dimethylaminopyridine
DMF	=	Dimethylformamide
DMSO	=	Dimethyl Sulfoxide
DMSO-d_6	=	Deuterated dimethylsulfoxide
ESA	=	Excited state absorption
H_2Pc	=	Metal free phthalocyanine complexes
HOMO	=	Highest molecular orbital
LUMO	=	Lowest unoccupied molecular orbital
ISC	=	Intersystem crossing
MCD	=	Magnetic circular dichroism
MPcs	=	Metallophthalocyanines
MPc-SiNPs	=	Metallophthalocyanine silica nanoparticles conjugate
NLA	=	Nonlinear Absorption
NLO	=	Nonlinear Optics
OA	=	Open Aperture
PXRD	=	Powder X-ray diffractometry
Pcs	=	Phthalocyanine complexes

Abbreviations

PDT	=	Photodynamic therapy
RSA	=	Reverse saturable absorption
SA	=	Saturable Absorption
SiNPs	=	Silica nanoparticles
SiNPs-COOH	=	Carboxyl-functionalized silica nanoparticles
SiNPs-NH$_2$	=	Amino-functionalized silica nanoparticles
SiNPs-N$_3$	=	Azide-functionalized silica nanoparticles
TCPC	=	Tetracarboxy phthalocyanine
TEM	=	Transmission electron microscope
TEOS	=	Tetraethyl orthosilicate
TGA	=	Thermo-gravimetric analysis
UV/vis	=	Ultraviolet/visible
XPS	=	X-ray photoelectron spectroscopy
Zn	=	Zinc
ZnPc	=	Zinc Phthalocyanine

List of Symbols

τ_{F1}	=	Longer lifetime
τ_{F2}	=	Shorter lifetime
τ_{avF}	=	Average lifetime
α	=	Non-peripheral position
β	=	Peripheral position
Φ_F	=	Quantum yield
Φ_T	=	Triplet quantum yield
τ_T	=	Triplet lifetime
Φ_Δ	=	Singlet oxygen quantum yield
Φ_{ic}	=	Quantum yield of Internal Conversion
τ_{isc}	=	Intersystem Crossing times
$I_m[\chi^{(3)}]$	=	Imaginary component of the third order susceptibility
γ	=	Second order hyperpolarizability
β_{eff}	=	Effective nonlinear absorption coefficient
I_{lim}	=	Limiting intensity threshold limit

List of Figures

List of Schemes

List of Tables

Chapter One

1. Introduction

This chapter highlights the general properties of silica nanoparticles (SiNPs), their diverse applications, synthesis, characterization and functionalization.

The synthesis of symmetrical and asymmetrical phthalocyanine complexes (Pcs) and their combination with silica nanoparticles (covalently and non-covalently) with possible applications are also presented.

1.1   Silica nanoparticles (SiNPs)

Nanoparticles are materials with diameter in the range of 1-100 nm. The continued research interest in nanoparticles is as a result of some of their versatile properties, which includes their tunable size, adjustable shape, large surface area and ease of functionalization. Some examples of nanoparticles include but are not limited to quantum dots, organic dyes, liposome, metal or metal oxide, up-conversion and silica nanoparticles [1-4].

Monodispersed silica nanoparticles were first synthesized by Kolbe in 1956 and subsequently reproduced and improved on by Stober et al in 1968 [5]. The research focus on SiNPs is due to their inherent properties which include [6-11]:

- Ease of synthesis and separation,

- Biocompatibility,

- Low toxicity,

- Porosity,

- Ease of surface functionalization due to the silanol groups,

- Chemical and thermal stability,

- Adsorption capacity,

- Capacity for encapsulation,

- Large surface area to volume ratio,

- Photophysical inertness and

- Hydrophilic nature.

The capacity to combine these properties has made silica nanoparticles a versatile platform for many applications [12].

1.1.1   Synthesis of SiNPs
Amorphous silica nanoparticles are generally synthesized via two protocols:

- Sol gel or Stober and

- Microemulsion method

The Stober method is used for synthesizing uniform sized spherical silica nanoparticles [5]. The method requires the use of an organo-silicate precursor (usually tetraethyl orthosilicate, TEOS), which undergoes hydrolysis in a mixture of water, ethanol and ammonia solution (acting as the catalyst) to produce silicic acid. The silicic acid undergoes condensation to produce di-silicic acid which also goes through condensation to form amorphous silica nanoparticles, Scheme 1.1. Over the years, a lot of studies have been carried out to improve on the size, shape and uniformity of the particles produced via the Stober protocol [13-17]. More recently, it was observed that the rate at which TEOS is added to the reaction mixture affects the size of the nanoparticles, at an increasing rate, a decrease in size was obtained while at a slow rate, an increase in size of the particles were observed [17].

It has also been reported that as the ratio of solvent (water and ethanol) to TEOS increases, the sizes of the synthesized particles decrease nonlinearly [18]. Rahman and co-workers controlled the size, size distribution and the yield of SiNPs by varying the concentration of reactants, feed rate of the catalyst, temperature and the mixing mode of the reactants [19]. The particles synthesized after optimization of the reaction conditions were homogenous and stable with a mean diameter of about ~7 nm [19]. It was also observed that freeze drying of the particles further improved the quality of powder compared to the heat drying method [20, 21]. The formation of silica nanoparticles by the Stober process may be described by the overall reaction as shown by equation 1.1.

$$Si(OC_2H_5)_4 \; + 2H_2O \; \rightleftharpoons \; SiO_2 + \; 4C_2H_5OH \qquad (1.1)$$
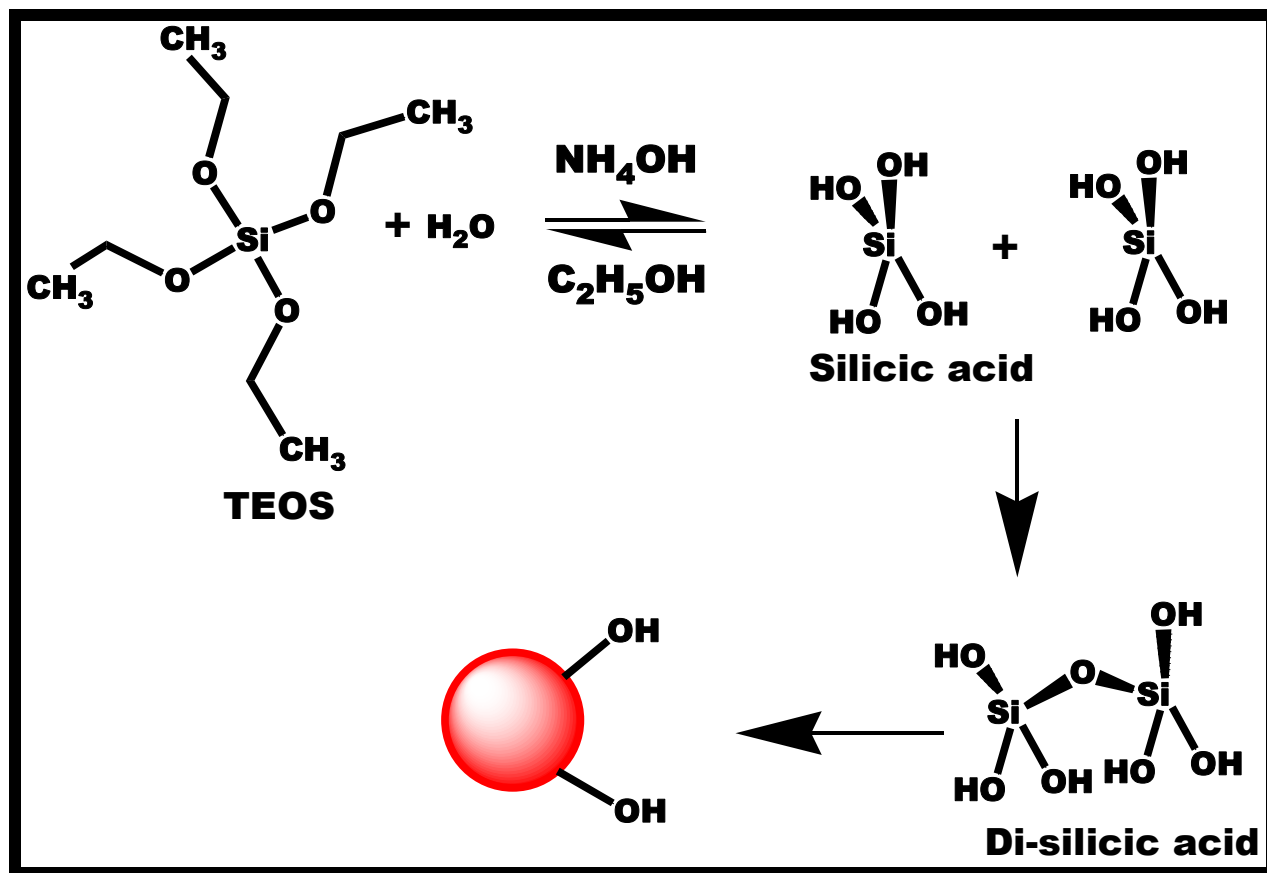
Scheme 1.1: Representation of a typical synthesis of SiNPs via the Stober protocol. TEOS: Tetraethyl orthosilicate.

In the reverse microemulsion protocol, TEOS is hydrolyzed in a reverse micelle or water in oil microemulsion system containing a homogenous mixture of water, oil and surfactant molecules. In this method, the water droplets are stabilized by the surfactant molecules thus allowing for dispersion in the oil. Due to the fact that water droplets control the nucleation and growth process, the resulting particles are highly monodispersed, uniform and spherical compared to the Stober method. The concentrations of both water and surfactant affect the size of silica particles synthesized in microemulsion [**16, 22-24**]. This method has been used to encapsulate materials ranging from dyes to other nanoparticles [**16, 25**]. Both the Stober and reverse microemulsion method were employed in this work.

1.1.2   Functionalization of SiNPs

The ease of functionalizing SiNPs is due to the presence of silanol on its surface which allows for both non-covalent and covalent interaction. Non covalent interaction could involve physical adsorption or entrapment of molecules via electrostatic interactions. The covalent interaction approach could be achieved by direct chemical reaction, linker strategy or click chemistry. The covalent method is preferable due to stability and reproducibility [**10, 16, 26-28**].

Furthermore, the high porosity of amorphous silica nanoparticles allows for the doping or encapsulation of functional materials and the porosity of these particles could be tailored to hold small molecules or large nanomaterials. The photophysical inertness of the SiNPs matrix also allows the dopants to retain or improve on their original properties [**16, 29**].

1.1.3   Applications of SiNPs

The ability to control the properties of SiNPs during synthesis and the ease of functionalizing these particles has led to the design of hybrid particles with diverse applications. In addition, the doping of materials within the matrix of SiNPs and the functionalization of the surface of the SiNPs has led to the development of multifunctional scaffolds for various applications [**28-31**]. In addressing the drawbacks (low fluorescence intensity and poor photostability) experienced by traditional photo-emitters such as organic dyes, fluorescent proteins, quantum dots and dyed polymer nanoparticles, SiNPs have been used to coat these fluorescent probes.

The SiNPs protects the encapsulated emitter from the environment and also enhances some of the photophysical properties of the emitters depending on the arrangement within the silica matrix [**3, 16, 29, 32, 33**]. These SiNPs containing fluorescent dyes have found applications as sensors [**34-40**], bio-markers for cells imaging [**41, 42**], in optical barcodes [**43**] and in bio-sensors [**44, 45**].

SiNPs have also found applications as drug delivery systems in photodynamic therapy (PDT) [**31, 46-48**]. SiNPs have been used to encapsulate: (i) DNA for gene therapy [**49**], (ii) gold nanoparticles for optical sensing [**50, 51**], (iii) magnetite for magnetic resonance imaging [**52, 53**], (iv) titanium oxide for photo-catalysis [**54, 55**] and (v) silver nanoparticles for sensing [**56**].

1.1.4   Characterization of SiNPs

The characterization of nanoparticles is important in elucidating the type of nanoparticles synthesized. The amorphous nature of silica nanoparticles can be determined using a powder X-ray diffractometry (PXRD). The SiNPs are normally characterized by a broad peak centred at around $2\theta = 23.0°$ [**57, 58**], Fig 1.1.
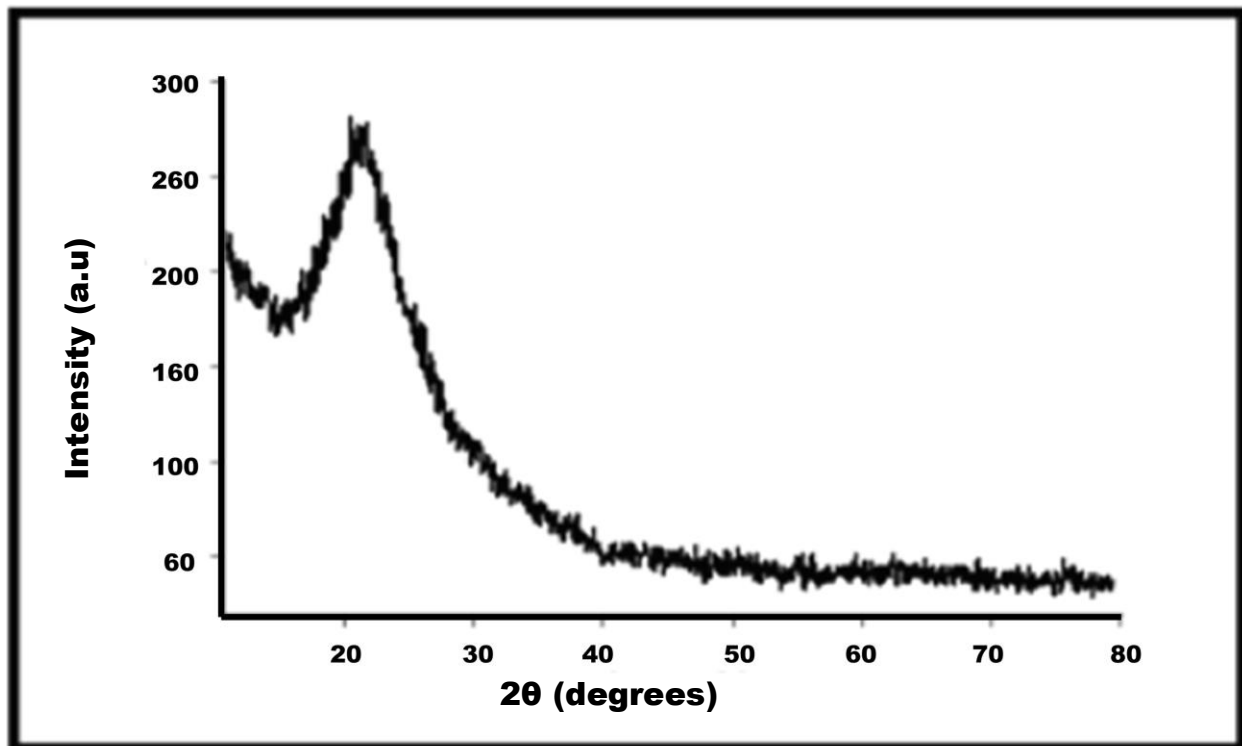
Figure 1.1: PXRD pattern of SiNPs prepared by the Stober method [57]

The size, size distribution and morphology of the amorphous silica nanoparticles can be determined using the transmission electron microscope (TEM) [**58, 59**]. Size distribution and TEM image of silica nanoparticles is shown in Figure 1.2.
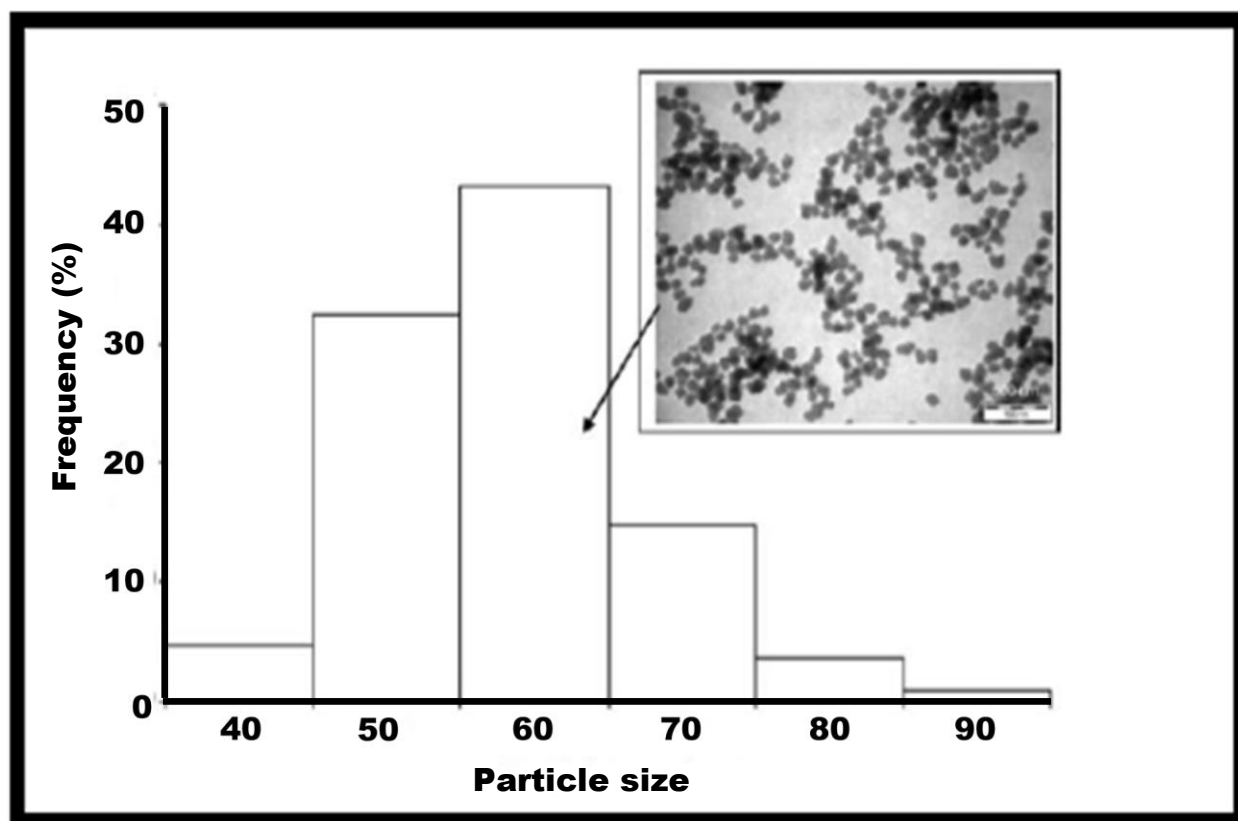
Figure 1.2: Particle size distribution of SiNPs (Inset TEM image of SiNPs) [58]

The surface area and porosity of nanoparticles can be determined using the Brunauer-Emmet-Teller (BET) method. The BET theory is an extension of the Langmuir theory (which relates to monolayer adsorption of gas molecules) and it has the following assumptions: the surface being measured is homogenous, no lateral interaction is occurring between particles, the upper layer of the surface is in equilibrium with the vapor phase, all the surface has the same adsorptive energy for the adsorbate (gas molecules), gas molecules adsorb on a solid layer in an infinite manner, the first interacting layer undergoes heat adsorption and while the upper layers undergo heat of

condensation [**60, 61**]. The data obtained from the BET is displayed in the form of an isotherm, which plots the amount of gas adsorbed as a function of the relative pressure. The BET relationship for the multilayer gas sorption at relative pressures, P/P_0 is given by equation 1.2.

$$\frac{1}{V[(P_0/P)-1]} = \frac{1}{V_m C} + \frac{C-1}{V_m C}\left(\frac{P}{P_0}\right)$$
(1.2)

where V is the volume of adsorbed gas quantity, P is the pressure, P_0 is the saturation pressure, V_m is the volume of gas required to form a monolayer (monolayer capacity) and C is the BET constant.

The surface area is given by equation 1.3.

$$S_t = \frac{V_m N_A A_m}{M_v}$$
(1.3)

where S_t, is the total surface area, N_A is the avogadro's number, A_m is the cross sectional area of the adsorbate, M_v is the molar volume. A typical BET isotherm for SiNPs is shown in Fig 1.3.
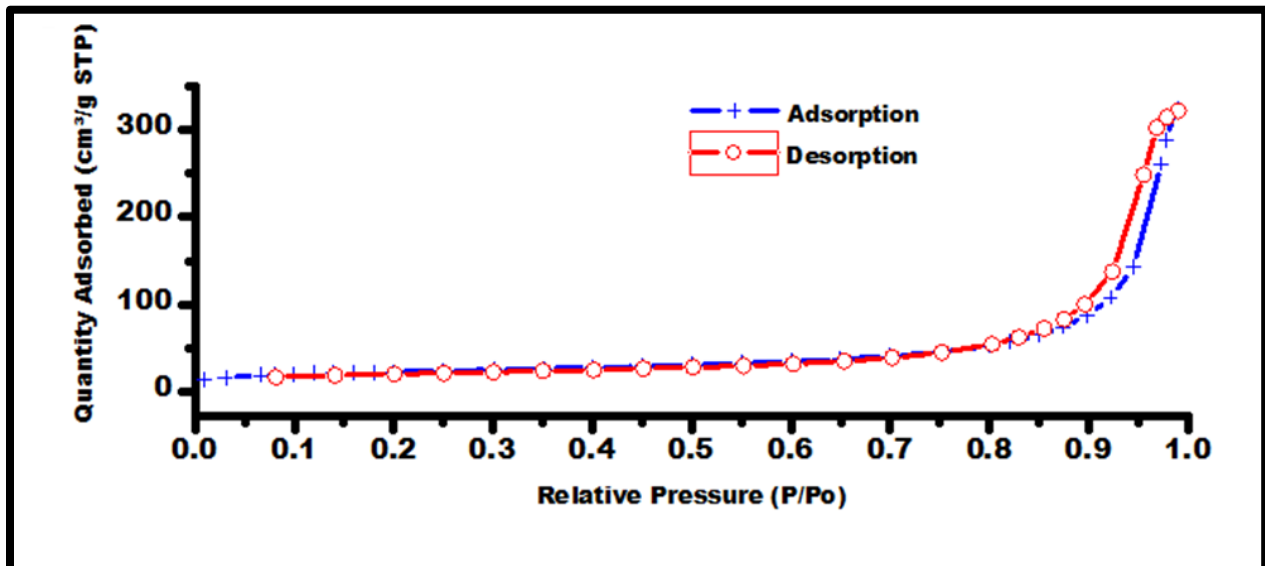
Figure 1.3: Nitrogen adsorption–desorption isotherms of SiNPs alone [unpublished work].

The chemical composition of the SiNPs surface in terms of electronic state could be determined using the X-ray photoelectron spectroscopy (XPS). The XPS is a non destructive technique that uses x-rays to induce photoelectron emission from the sample surface. The sensitivity of this technique is due to the fact that only photoelectrons close to the sample surface can escape without energy loss [62]. A typical XPS wide scan of SiNPs is shown in Fig 1.4 [63].
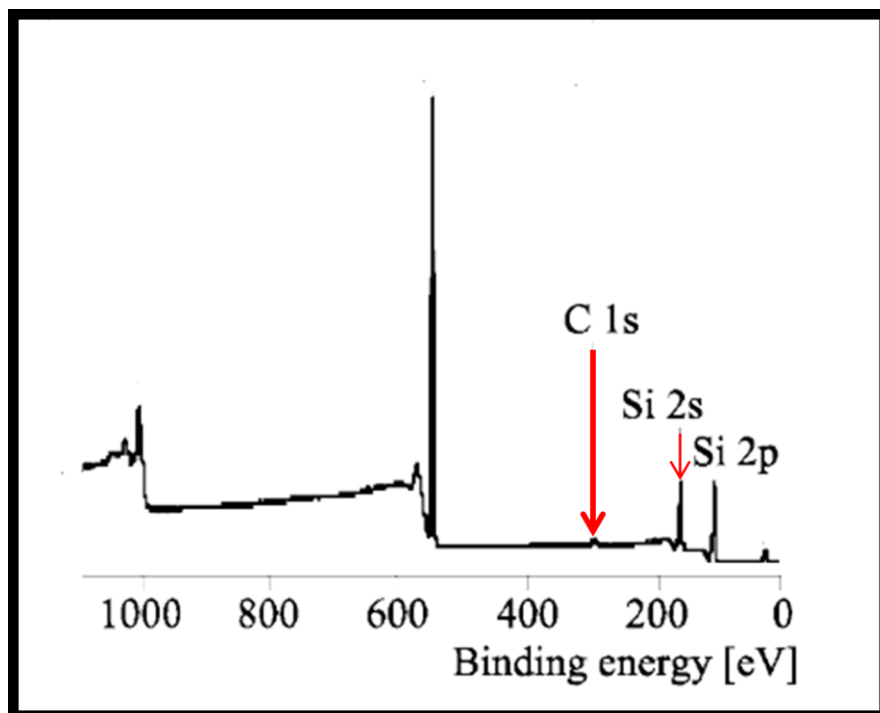
Figure 1.4: A typical wide scan XPS spectrum of uncoated SiNPs [63]

Other techniques such as thermogravimetric analysis (TGA), Fourier transform infrared spectroscopy (FTIR) and Raman spectroscopy can be used to determine the thermal stability, functional groups and the interaction between nanoparticles and functional materials respectively.

1.1.5   SiNPs to be employed in this work

The SiNPs used in the work were synthesized either by the Stober or microemulsion protocol. The microemulsion method was used for encapsulating dyes into the silica

matrix, while the Stober method was used for making particles that were functionalized on the surface after synthesis. Fig. 1.5 list the SiNPs used in this work.

The SiNPs were functionalized with 3-aminopropyltriethoxysilane (APTES) and 3-azidopropyltriethoxysilane. The amino functionalized SiNPs (APTES functionalized) were further modified using succinic anhydride to derive carboxylic acid containing SiNPs. The silanol, amino, azide and carboxylic acid groups on the SINPs were used for covalent grafting of substrates; these will be discussed in detail later.
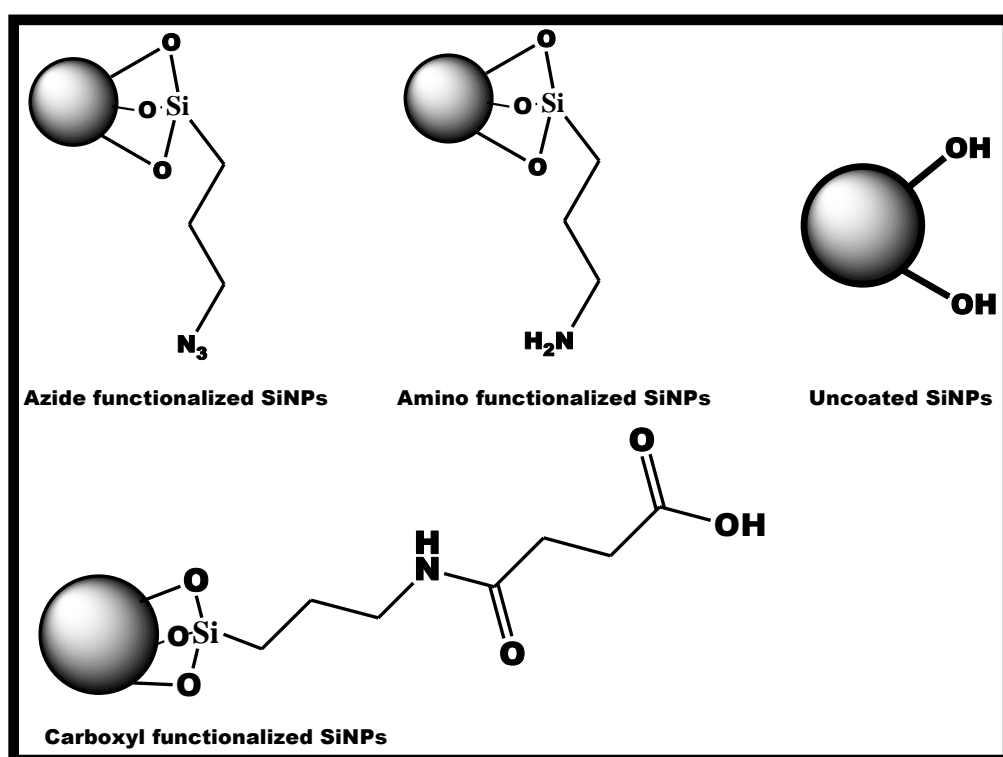
Fig. 1.5: List of surface functionalized SiNPs used in this work.

Sub Aim of the work:

- Synthesize SiNPs via the Stober protocol and functionalize the surface of the SiNPs with free hydroxyl, amino, carboxyl and azide groups

- Characterize the SiNPs and conjugate them with phthalocyanines (Pcs). Study and compare the photophysicochemical properties of both the phthalocyanine complex alone and the hybrid particles formed. The intention was to determine if the

11

properties of the phthalocyanine complexes would improve on grafting to the SiNPs via covalent bond.

- Dope the phthalocyanine complexes within the matrix of the SiNPs via reverse microemulsion, characterize and study the photophysics of the doped complexes.

1.2   Metallophthalocyanines (MPcs)

Phthalocyanines (Pcs) and their metallo-derivatives are macrocyclic compounds which consist of four isoindole units linked through nitrogen atoms and are two dimensional with 18 π electron system, Fig 1.6 [**64-66**]. About 70 metals in different oxidation states can be incorporated into the cavity of the Pc ring to form metallophthalocyanines. In addition, a wide range of substituent (s) or ligands can be attached to the Pc ring at positions designated α (non-peripheral), β (peripheral), Fig 1.6 and axially (depending on the oxidation state of the incorporated central metal). Due to the π-electron conjugated system, architectural flexibility, high molar absorptivity, high triplet lifetimes and quantum yields, absorption in the near infra-red region, chemical and thermal stability [**64, 65, 67**], Pcs have been used as optical limiters, electro-catalysts, dyes, photosensitizers in photodynamic therapy (PDT), sensors, in solar cells [**68-72**] and in combination with nanomaterials for various applications [**73**].
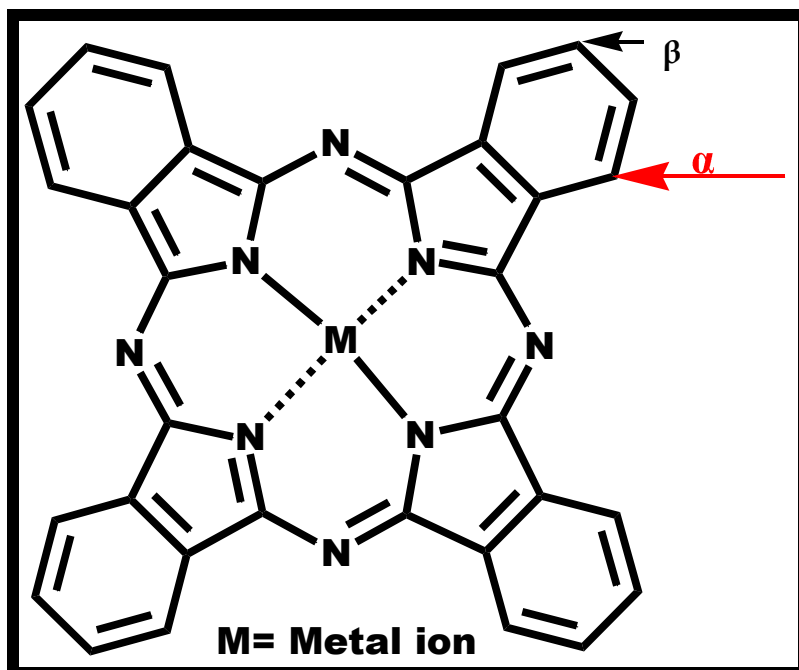
Fig. 1.6: General structure of phthalocyanine.

1.2.1 Electronic absorption spectra of MPcs

The electronic absorption spectrum of a typical metallated phthalocyanine (MPc) complex, Fig 1.7, is characterized by an intense absorption band in the visible region of the electromagnetic spectrum called Q-band and the less intense B-band (consisting of two bands) appearing between 300 – 400 nm [74-76]. For the metal free phthalocyanine complexes (H_2Pc), the lower symmetry, D_{2h}, results in a split in the Q-band. Also, the lowering of the symmetry of an MPc via insertion of a large central metal could also result in the splitting of the Q-band [64].
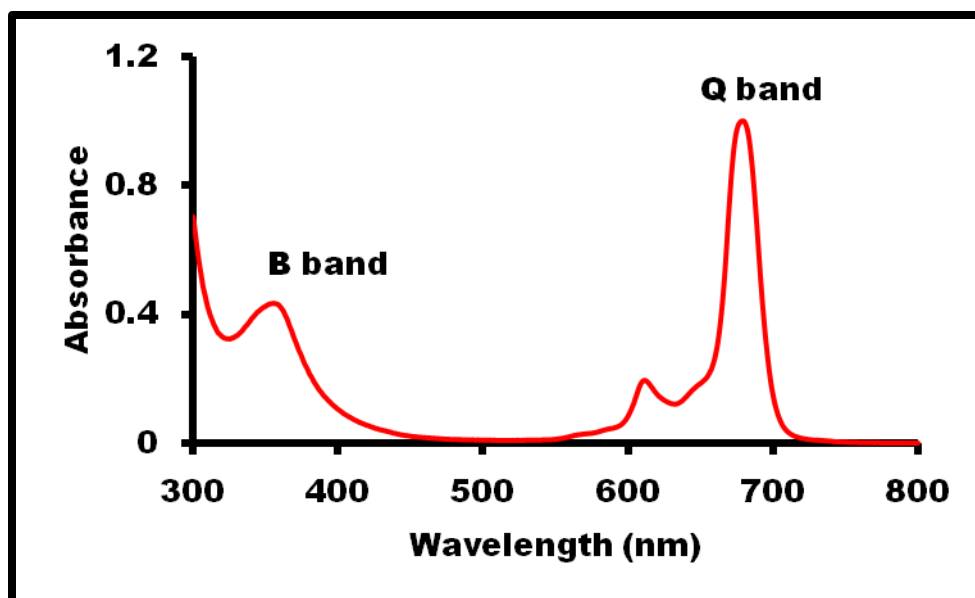
Fig. 1.7: Typical electronic absorption spectrum of MPc (unpublished work).

The Gouterman's model is used to explain the origin of the characteristic bands in MPcs and the model is based on the linear combination of atomic orbital. The Q band absorption is due to the excitation from the ground state (a_{1u}), which is the highest molecular orbital (HOMO) to the lowest unoccupied molecular orbital e_g, (LUMO). While the B bands (B_1 and B_2) result from transition between the a_{2u} or b_{2u} to the e_g of the LUMO [77-79], Fig. 1.8.
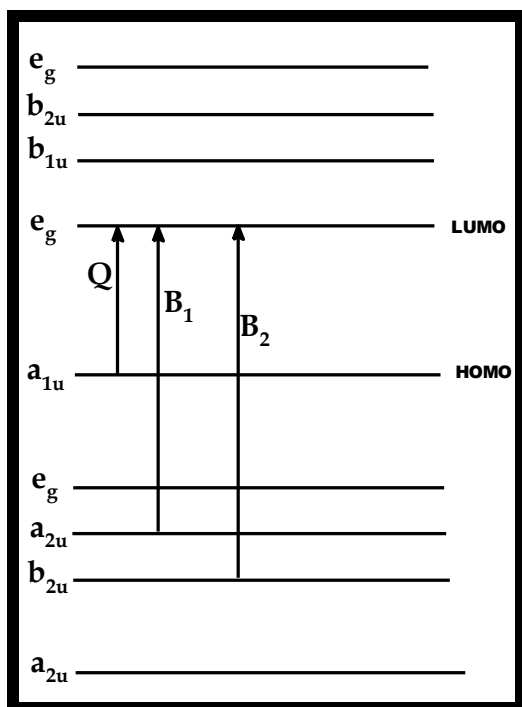
Figure 1.8: Electronic transitions in MPcs showing the origin of Q and B absorption bands

1.2.2   Synthesis of symmetrical and unsymmetrical MPcs

MPcs may be synthesized by the tetramerization of phthalonitrile precursors in the presence of metal salts [**80**, **81**]. Mono-substituted phthalonitriles (**2**, **5**), which are precursors for the formation of tetra-substituted Pcs (**3**, **6**) are synthesized by the base catalyzed nucleophilic aromatic substitution of the 4-nitrophthalonitrile or 3-nitrophthalonitrile precursor (**1**, **4**), Scheme 1.2, with substituent at either the 3 or 4 position [**82, 83**].
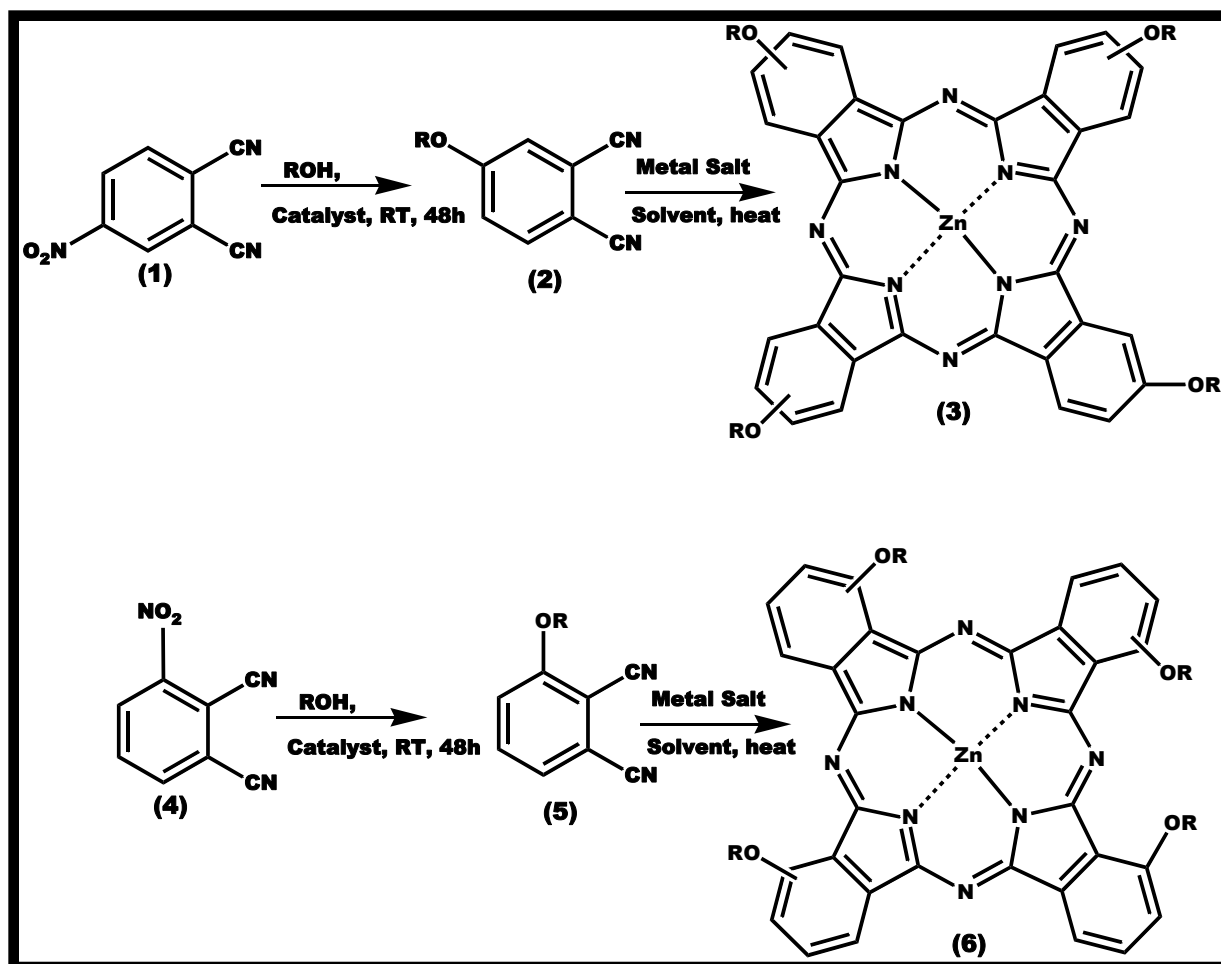
Scheme 1.2: Synthesis of peripheral (3) and non-peripheral (6) tetra-substituted MPcs from mono-substituted phthalonitriles (2) and (5).

Different approaches have been taken to synthesize unsymmetrical MPcs [84-88], however, the most common protocol for the formation of unsymmetrical Pcs is the statistical condensation reaction between two different phthalonitrile precursors to form compounds with A_4, A_2B_2, AB_3, A_3B, A_2B_2 and B_4 structures, Scheme 1.3. The desired unsymmetrical structure, AB_3 (7) is usually obtained by statistically combining the different phthalonitrile precursors and subsequent separation of the different fractions formed via chromatographic methods.
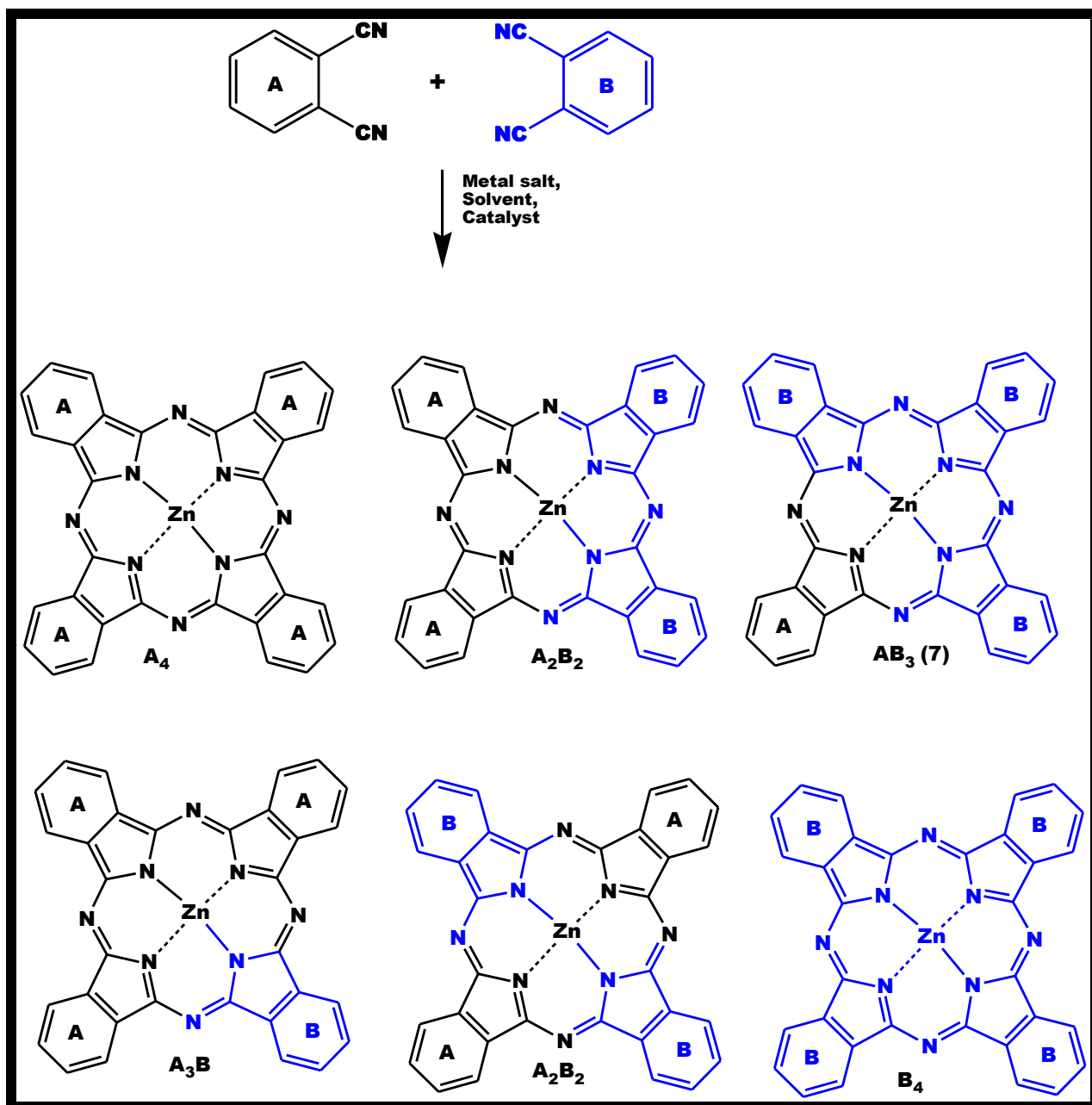
Scheme 1.3 Schematic representation of the synthesis of low symmetry phthalocyanines

In this work, tetra-substituted and mono-substituted MPc complexes were synthesized with the intention of grafting to the SiNPs surface via amide bond, ester bond and click

chemistry. The grafting was designed to range from non specific binding (via the tetra-substituted MPcs) to specific binding (via the mono-substituted MPcs).

1.2.3   Phthalocyanine molecules synthesized in this work

The structures of all the phthalocyanine complexes used in this work are shown in Fig. 1.9, while the substituent(s) are shown in **Table 1.1.**

The phthalocyanine complexes employed in this work were selected for the following reasons:

- To synthesize phthalocyanine complexes with substituent(s) that can be covalently grafted to the surface of SiNPs via amide bond, ester bond or click chemistry.
- To allow for more defined coordination between SiNPs and MPc, mono-substituted phthalocyanines (**13-15** and **19-21**) are employed in this work.
- To compare α (**8**) versus β (**10**) using symmetrical substitution with 3-carboxyphenoxy groups on **8** and **10.**
- To compare α (**11**) versus β (**12**) using symmetrical substitution with 4-aminophenoxy groups on **11** and **12**.
- The effect of the point of substitution on the phenoxy group: 3-position (**8**) versus 4-position (**9**).
- The effect of the point of substitution on the phenoxy group: 3-position (**19**) versus 4-position (**21**).
- To compare α (**13**) versus β (**14**) using asymmetrical substitution. Complexes **13** and **14** have 4-aminophenoxy group as a substituent.
- Complexes **16-18** were compared to complexes **19-21.** Complexes **16-18** are precursors for synthesizing complexes **19-21**
- To compare α (**19**) versus β (**20**) using asymmetrical substitution. Complexes **19** and **20** have 3-((hex-5-ynyl)-benzoate) phenoxy as substituent.

- To check the effect of direct attachment of the amino group (**15**) as opposed to when separated with a phenoxy group (**14**).

- To compare the effects of the amino (**11**) and carboxy (**9**) substituent (s). Both complexes are symmetrical and β substituted.

- To compare the effect of alkyne (**20**) and amino-phenoxy (**14**) group. Both complexes are asymmetrical and β substituted.

- To compare the effect of alkyne (**19 or 21**) and amino-phenoxy (**13**). Both complexes are asymmetrical and α substituted.

- Complexes **13, 19, 20** and **21** which are asymmetrical, are new compounds and complex **10** which is symmetrical is also new.

Zinc (Zn) metal was chosen as the central atom for the complexes because phthalocyanine complexes containing Zn usually produce high triplet yields with long lifetimes which are essential for different applications [**89**].
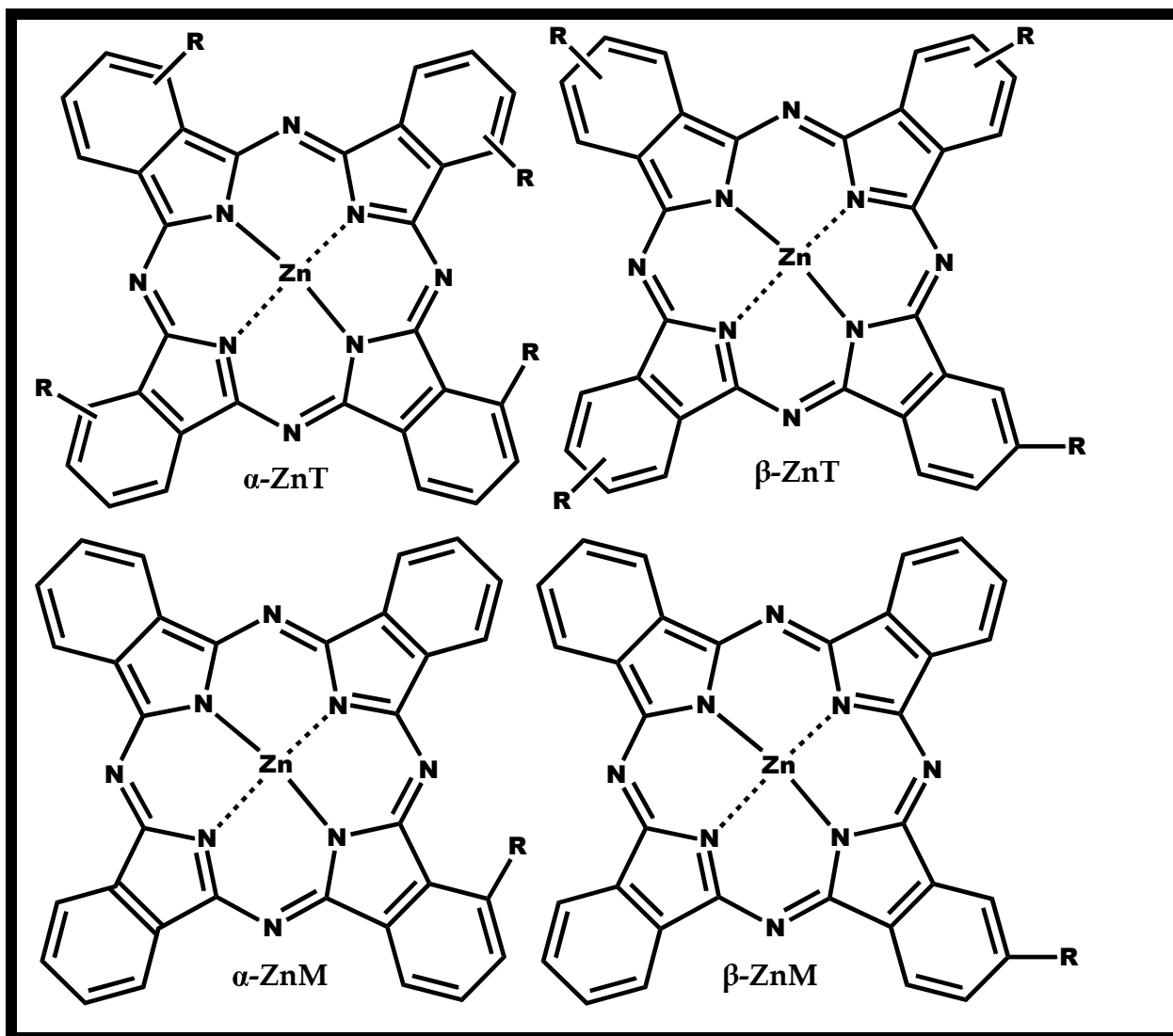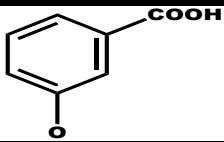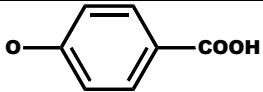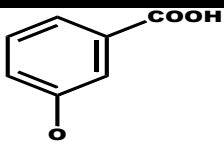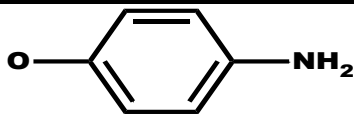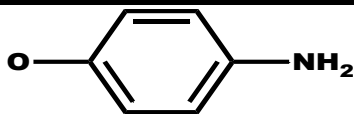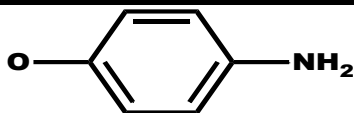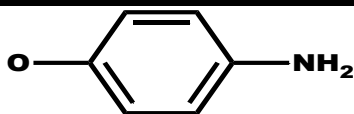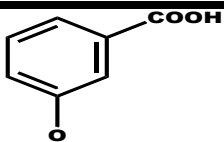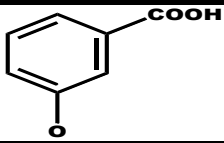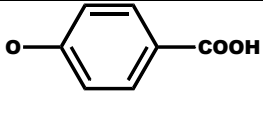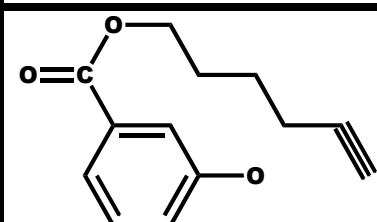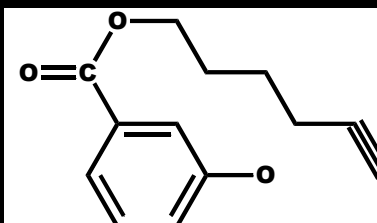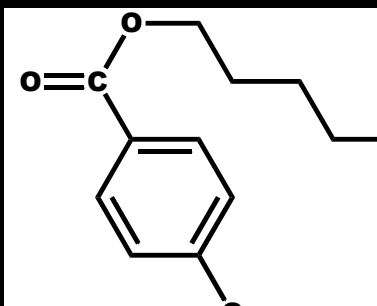
Fig. 1.9: Structures of phthalocyanines used in this work

Table 1.1 is key to structures shown in Figure 1.9.

Names of Complex (Abbreviation)	R =	Position	Complex number
1(4), 8(11), 15(18), 22(25)-tetrakis-(3-carboxyophenoxy)phthalocyaninato zinc (II) (**α-ZnT-3-CPPc**)		α	**(8)**
1(4), 8(11), 15(18), 22(25)-tetrakis-(4-carboxyophenoxy)phthalocyaninato zinc (II) (**α-ZnT-4-CPPc**)		α	**(9)**
2(3), 9(10), 16(17), 23(24)-tetrakis-(3-carboxyphenoxy)phthalocyaninato zinc (II) (**β-ZnT-3-CPPc**)		β	**(10)-New**
1(4), 8(11), 15(18), 22(25)-tetrakis-(4-aminophenoxy) phthalocyaninato zinc (II) (**α-ZnTAPPc**)		α	**(11)**
2(3), 9(10), 16(17), 23(24)-tetrakis-(4-aminophenoxy)phthalocyaninato zinc (II) (**β-ZnTAPPc**)		β	**(12)**
1-Mono-(4-aminophenoxy)phthalocyaninato zinc (II) (**α-ZnMAPPc**)		α	**(13)-New**
2-Mono-(4-aminophenoxy)phthalocyaninato zinc (II) (**β-ZnMAPPc**)		β	**(14)**
2-Mono-(4-amino)phthalocyaninato zinc (II) (**β-ZnMAPc**)	**NH₂**	β	**(15)**
1-Mono-(3-carboxyphenoxy)phthalocyaninato zinc (II) (**α-ZnM-3-CPPc**)		α	**(16)**
2-Mono-(3-carboxyphenoxy)phthalocyaninato zinc (II) (**β –ZnM-3-CPPc**)		β	**(17)**
1-Mono-(4-carboxyphenoxy)phthalocyaninato zinc (II) (**α-ZnM-4-CPPc**)		α	**(18)**

Names of Complex (Abbreviation)	R =	Position	Complex number
1-Mono-(3-((hex-5-ynyl)-benzoate)-1(4)-phenoxy)phthalocyaninato zinc (II) (**α-ZnM-3-CAPc**)		α	**(19)-New**
2-Mono-(3-((hex-5-ynyl)-benzoate)-2(3)-phenoxy)phthalocyaninato zinc (II**) (β-ZnM-3-CAPc)**		β	**(20)-New**
1-Mono-(4-((hex-5-ynyl)-benzoate)-1(4)-phenoxy)phthalocyaninato zinc (II) (**α-ZnM-4-CAPc**)		α	**(21)-New**

1.2.4   Photophysical and photochemical properties of MPcs

The photophysicochemical behavior of phthalocyanines can be conveniently described by the Jablonski diagram [**90**].
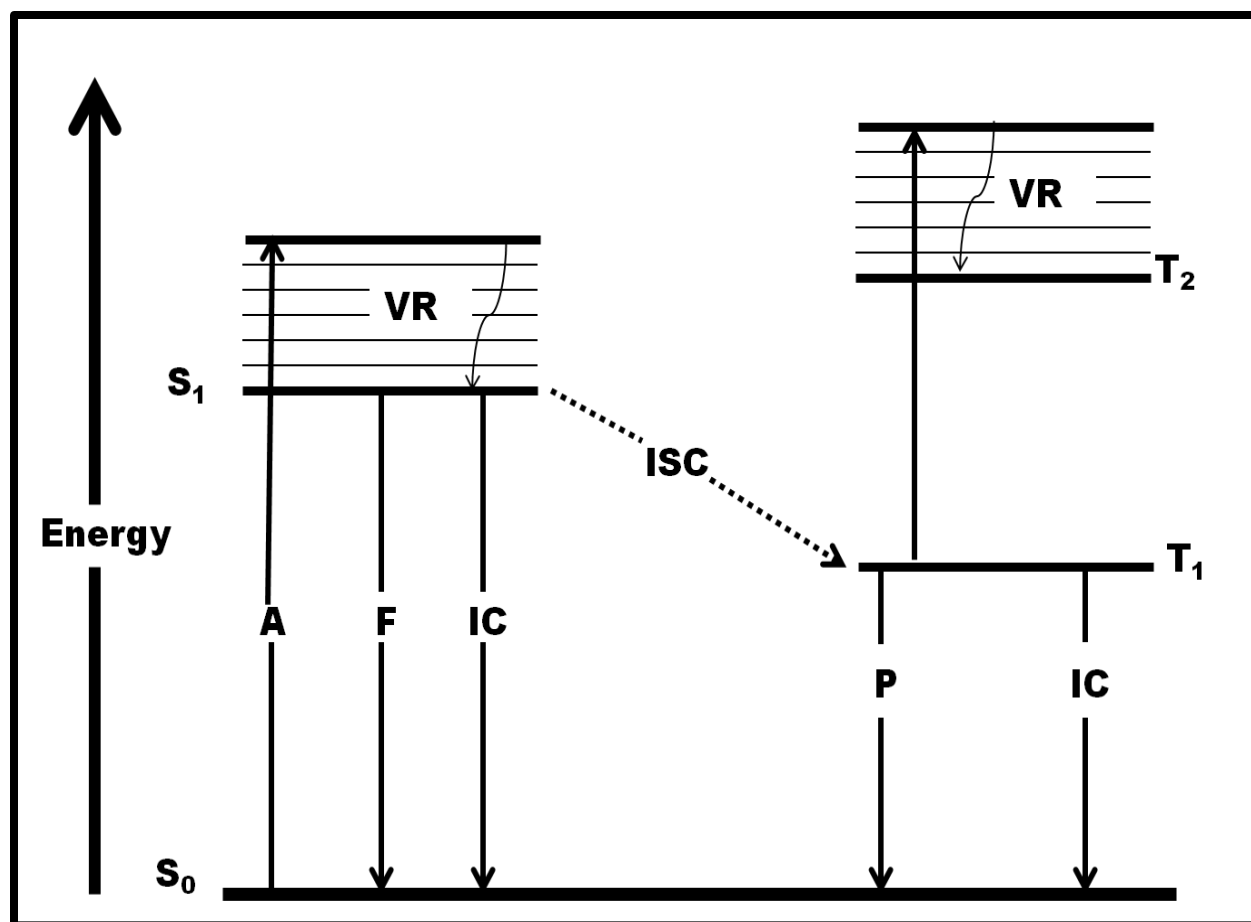
Figure 1.10: Jablonski diagram displaying transitions of a molecule from its lower ground state energy to its higher excited state energy following irradiation with light; A = absorption, VR = vibrational relaxation, ISC = intersystem crossing, F = fluorescence, IC = internal conversion, P = phosphorescence, S_0 = singlet ground state, S_1 = singlet excited state and T_1 = 1st excited triplet excited state, T_2 = second excited triplet state.

1.2.4.1   Fluorescence quantum yield (Φ_F) and lifetime (τ_F)

Fluorescence quantum yield (Φ_F) is defined as the number of fluorescence photons emitted per excitation photon absorbed [90]. Some of the factors that could affect the fluorescence behavior of MPcs include the size of the central metal, temperature,

substituent on the Pc ring, aggregation, extended π conjugated system, solvent polarity and pH. The fluorescence lifetime (τ_F) is the average time spent by the fluorophores in the excited singlet state [91-93]. In this work, the time–correlated single photon counting technique (TCSPC) is used in determining the τ_F.

Fluorescence quantum yields (Φ_F) may be determined by comparative methods [94, 95] using the fluorescence quantum yield of a known Pc as a standard. In this work, ZnPc in DMSO was used as a standard (Φ_F) = 0.20 [95]. The quantum yield of fluorescence is calculated using Equation 1.4. [94]

$$\Phi_F = \Phi_F^{Std} \frac{F A_{Std} n^2}{F_{Std} A n_{Std}^2} \qquad\qquad (1.4)$$

where F and F_{Std} are the areas under the fluorescence curves for sample and standard respectively. A and A_{Std} are the absorbances of the sample and reference at the excitation wavelength respectively, while n and n_{Std} are the refractive indices of solvents in which the sample and reference were dissolved, respectively.

1.2.4.2   Triplet quantum yield (Φ_T) and lifetimes (τ_T)

The triplet quantum yields were determined in DMSO using a comparative method [96], equation 1.5 with ZnPc as the standard.

$$\Phi_T = \Phi_T^{Std} \frac{\Delta A_T \; \varepsilon_T^{Std}}{\Delta A_T^{std} \; \varepsilon_T} \qquad\qquad (1.5)$$

where ΔA_T and ΔA_T^{std} are the changes in the triplet state absorbances of the sample and the standard, respectively. ε_T and ε_T^{Std} are the triplet state molar extinction coefficients of the sample and the standard respectively. Φ_T^{Std} is the triplet quantum yield for the standard, ZnPc (Φ_T^{Std} = 0.65 in DMSO) [96]. The values of ε_T and ε_T^{Std} are normally determined by use of the singlet depletion method [97], using equations 1.6 and 1.7.

$$\varepsilon_T = \varepsilon_S \frac{\Delta A_T}{\Delta A_S}$$ (1.6)

$$\varepsilon_T^{Std} = \varepsilon_S^{Std} \frac{\Delta A_T^{Std}}{\Delta A_S^{std}}$$ (1.7)

where ε_S and ε_S^{Std} are the molar extinction coefficient of the ground state for the sample and standard respectively. ΔA_S and ΔA_S^{std} are the changes in the singlet state absorbances of the sample and the standard, respectively. Other parameters in the equations have been defined in the paragraph above. The triplet decay (τ_T) is measured using laser flash photolysis and the data is analyzed using OriginPro 8.0 software.

1.2.4.3   Singlet oxygen quantum yield (Φ_Δ)

The process of generating singlet oxygen ($^1O_2$) by MPcs involves the absorption of light, the transition of the excited MPc molecule from the singlet excited state to the triplet state via intersystem crossing and the transfer of energy from the triplet state of the MPc to the ground state molecular oxygen [98-100]. The singlet oxygen quantum yield (Φ_Δ) could be defined as the amount of $^1O_2$ generated per photon absorbed by the phthalocyanine complex [101, 102].

Experimentally, the singlet oxygen quantum yield of phthalocyanine complexes can be determined using the optical (or the luminescence method) or chemical methods. In this work, we employed the optical method. The optical method involves the time-resolved phosphorescence decay of singlet oxygen at 1270 nm [103].

The dynamic course of the oxygen concentration [O_2 ($^1\Delta_g$)] can be monitored using equation 1.8 as described in literature [104].

$$I(t) = B \frac{\tau_D}{\tau_T - \tau_D}[e^{-t/\tau_T} - e^{-t/\tau_D}]$$ (1.8)

where, I(t) is the phosphorescence intensity of $^1O_2$ at time t, τ_D is the lifetime of $^1O_2$ phosphorescence decay, τ_T is the triplet state lifetime of the standard or sample and B is a coefficient involved in sensitizer concentration and $^1O_2$ quantum yield.

The singlet oxygen quantum yield, Φ_Δ, of the phthalocyanine is then determined by a comparative method using equation 1.9.

$$\Phi_\Delta = \Phi_\Delta^{Std} \cdot \frac{B}{B^{Std}}$$
$$\quad\text{(1.9)}$$

where Φ_Δ^{Std} is the singlet oxygen quantum yield for the standard ZnPc, B and B^{Std} are the coefficients of the sample and standard, respectively. In this work, ZnPc standard in DMSO was used (Φ_Δ^{Std} =0.67) [105].

1.2.4.4   Quantum yield of internal conversion (Φ_{ic}) and intersystem crossing times (τ_{isc})

The quantum yield of internal conversion (Φ_{IC}) is calculated using the equation 1.10,

$\Phi_{IC} = 1-(\Phi_T + \Phi_F)$
$\quad\text{(1.10)}$

where Φ_T is the triplet quantum yield and Φ_F is the fluorescence quantum yield. The equation assumes that only three processes (fluorescence, intersystem crossing and internal conversion) jointly deactivate the singlet excited states of the Pc complexes. The Φ_{IC} gives an estimate of the amount of energy lost via internal conversion.

The intersystem crossing time (τ_{isc}) is determined using equation 1.11 [106],

$\tau_{isc} = \tau_{avF} / \Phi_T$
$\quad\text{(1.11)}$

where τ_{avF} is the average singlet excited state lifetimes and Φ_T is the triplet quantum yields. τ_{isc} gives an indciation of how fast the transition from the singlet excited state to the triplet excited state is.

1.2.5   Silica nanoparticles-phthalocyanine conjugates and their applications

Phthalocyanine complexes have mostly been doped within SiNPs or physically adsorbed to the surface of SiNPs. In other instances; materials such as magnetic nanoparticles, folic acid have also been doped alongside Pcs to form a multi-functional nanoparticle [**107-115**]. In this thesis, we report for the first time the covalent grafting of Pcs to the surface of SiNPs, their characterization and the comparative photophysical study of the hybrid particles. The effects of the number, type and position of the substituent (s) on the photophysical properties of the novel conjugates are also evaluated. Phthalocyanine complexes are also doped within the silica matrix and compared to the surface grafted and the phthalocyanine complexes alone.

The hybrid particles formed on conjugating SiNPs with Pcs have found application as delivery systems for drugs in PDT, sensors, fluorescent probes and bio-labels [**106-110, 112, 113, 116-119**]. Table 1.2 shows some typical applications of phthalocyanine functionalized SiNPs. As Table 1.2 shows, only un-substituted or symmetrically substituted Pcs have been linked to SiNPs. No asymmetrical (mono-substituted) Pcs have been linked to SiNPs. Mono-substituted Pcs allow for a more defined linking to Pcs and are synthesized in this work. No detailed photophysical behavior of Pcs in the presence of SiNPs have been reported, such studies are crucial for the application of Pcs in many areas such as PDT and optical limiting. Hence, the photophysical properties of the Pcs in the presence of SiNPs are reported in this work.

Table 1.2: Examples of known phthalocyanines functionalized with SiNPs and their applications.

Compound	Application(s)	Reference
Tetra-tert-butyl zinc(II) phthalocyanine	PDT	[107]
Tetra-substituted carboxyl aluminum phthalocyanine (AlTCPc)	PDT, Imaging	[108]
Silicon phthalocyanine 4 (Pc4)	PDT	[109]
Zinc(II) phthalocyanine (ZnPc)	PDT, Imaging	[110]
2(3),9(10),1617(),23(24)-tetraamino-phthalocyanine Zinc II (ZnPc(NH$_2$)$_4$)	PDT	[111]
Aluminum phthalocyanine (AlPc) and Zinc (II) phthalocyanine (ZnPc)	-	[112]
Chloroaluminiumphthalocyanine (ClAlPc)	Optical limiting	[113]
Copper(II) phthalocyanine tetrasulfonic acid, tetrasodium salt (CuPc(SO$_3$Na$^+$)$_4$	Sensor	[114]
2(3),9(10),16(17),23(14)-tetrasulfophthalocyanine, MTSPc (M=Fe, Co, Ni, Cu and Al)	-	[115]
Zinc (II) phthalocyanine (ZnPc)	PDT	[116]

Sub Aim of the work:

- Synthesize and characterize tetra-substituted and asymmetrical Zinc phthalocyanine complexes substituted at the α and β positions with carboxyphenoxy, aminophenoxy, amino and terminal alkyne groups.
- For the first time covalently conjugate Pcs to the surface of the SiNPs.
- Compare systematically the effects of the number, type and position of the Pc substituent on the photophysicochemical properties of the newly formed conjugates.

28

- The optical limiting behavior of the tetra-substituted Pcs will be compared to the asymmetrical complexes.

- The behavior of the silica nanoparticles-phthalocyanine conjugates in a simulated biological medium will also be studied.

1.3   Nonlinear Optics (NLO)

Nonlinear optics is an area of optics that deals with the interaction of light (high intensity laser beams) with matter. Each nonlinear process may involve the intense laser light inducing a nonlinear response in a material and the material reacting by modifying the optical fields in a nonlinear way [**120, 121**]. Materials that display nonlinearity achieve this by exhibiting at least one of the following nonlinear optical mechanisms: nonlinear absorption (NLA), nonlinear refraction (NLR), induced scattering and phase transitions. These mechanisms also originate from processes such as two-photon absorption (TPA), excited state absorption (ESA), free carrier absorption (FCA), molecular reorientation, Kerr effect, excitation of free carriers, photo-refraction and optically induced heating [**122-126**].

Two major categories of passive devices known are optical switches and optical limiters. In this work, we focused on the optical limiting (OL) behavior of phthalocyanine complexes. Optical limiting is observed when the intensity of a light beam is strongly attenuated by a system acting as optical limiter once the intensity exceeds a threshold value, indicated as I_{lim}, Fig 1.11 [**127**].

An ideal optical limiter is a material that displays a linear transmittance below a specific fluence threshold but above this threshold, the output intensity becomes constant. Fig 1.11 shows the response of an ideal optical limiter to incident fluence.

It should be noted that under practical circumstances the limiting threshold will be less well defined and the output fluence will not be as constant as for the ideal case, but will slowly change from high to low transmittance [**124, 127**].
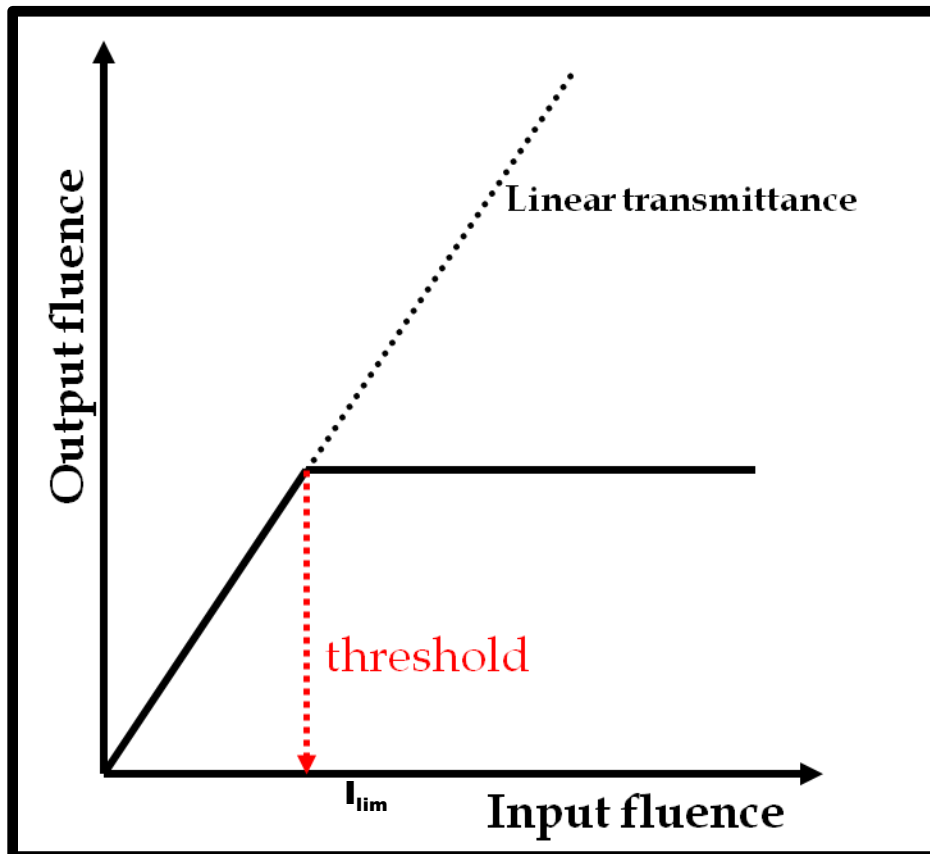
Fig. 1.11: The Optical response of an ideal limiter to incident fluence [124, 127]

Researchers have studied the nonlinear optical response of diverse materials over the years; some of the materials studied include inorganic crystals, organic molecules, nanoparticles, polymeric systems, organometallics and semi-conductors [**128-135**]. The preference for organic materials result from ease of modifying/optimizing the chemical structure to achieve desired NLO behavior, ease of processing into optical devices, fast response time and large nonlinear susceptibilities [**66, 123, 136, 137**].

Some of the applications of optical limiting materials include: photo-electronics, photonics and optical sensors [**124, 137-140**].

The nonlinear optical behavior of the materials can be characterized using the Z-scan technique with nanosecond and picosecond laser pulses. The Z-scan technique typically measures both the absorptive (open aperture system) and refractive (closed aperture system) nonlinearities. The open aperture system highlights the strength of the nonlinear absorption while the closed aperture system provides an understanding of the size of the nonlinear refractive index [**141, 142**]. In the Z-scan experiment, the material within the sample holder is moved from one side of the focus to the other side along the path (Z) of a tightly focused Gaussian beam and the closed and open transmittance of the material is measured as a function of the sample's position relative to the focus. A simplified schematic diagram of the Z-scan technique is shown in Fig 1.12.

The materials studied in this work were characterized with the open aperture Z-scan system using a nanosecond laser system.
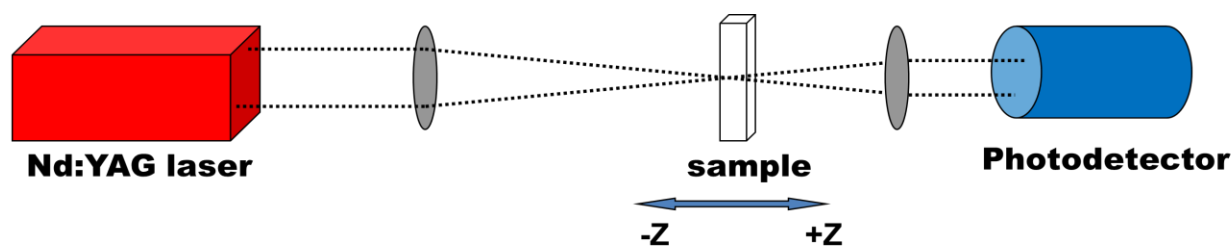
Fig. 1.12: A simplified schematic diagram of the Z-scan technique.

1.3.1   Optical limiting behavior of phthalocyanines

The large optical nonlinearities observed in organic molecules generally arise from their highly delocalized π-electron systems. MPcs which have 18 π-electron systems, conform to this requirement and have been studied extensively for NLO applications [**127, 128, 142-147**]. MPcs also have additional advantages which include architectural flexibility to achieve desired NLO response, planar structure, ease of processing into thin films/optical devices, ultrafast response time, high yields, purity and stability [**127, 143,**

148, 149]. There are three basic requirements for a material such as Pcs to be a good optical limiter; (1) An excited state absorption cross-section that exceeds the ground state absorption cross-section, (2) fast response and (3) high damage threshold [**136**].

OL for phthalocyanines occurs via nonlinear absorption (NLA) at 532 nm laser irradiation. The NLA mechanism observed is due to the population of the excited states through multi-photon absorption resulting in reverse saturable absorption (RSA) [**127, 130, 136, 144-149**].

The RSA mechanism in phthalocyanine complexes has been well described in literature by the five band model shown in Fig. 1.13 [**124, 136**].
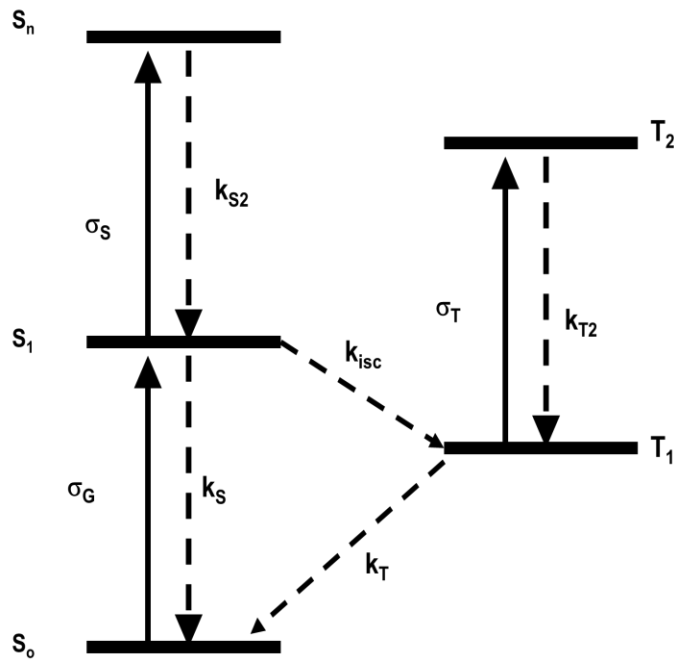
Fig 1.13: Generalized five-level system used in deriving the excited state absorption model used to simulate RSA in phthalocyanine system. S_i represents the singlet levels and T_i represents the triplet levels. The solid arrows imply an excitation resulting from photon absorption while the dashed arrows represent relaxations [123, 135].

RSA usually occurs in a system when the absorption cross section of the excited state (σ_s or σ_T) exceeds the cross section of the ground state (σ_G), this implies that absorption increase with input fluence. If σ_s or σ_T is smaller than the σ_G, the material becomes transparent or bleaches and it is referred to as saturable absorption (SA) [124]. The contribution of the excited states (singlet and triplet) to the nonlinear behavior of Pcs is dependent on the pulse width of the nanosecond laser used and the intersystem crossing times (τ_{isc}). If the pulse width of the nanosecond laser and the τ_{isc} are of the same order, the contribution to nonlinearity will be from both the excited singlet and triplet states. However, if the τ_{isc} is of higher order than the pulse width of the laser, the contribution is mainly from the singlet excited state [106, 149]. Fig 1.14 shows an open aperture (OA) Z-scan for a compound undergoing RSA.
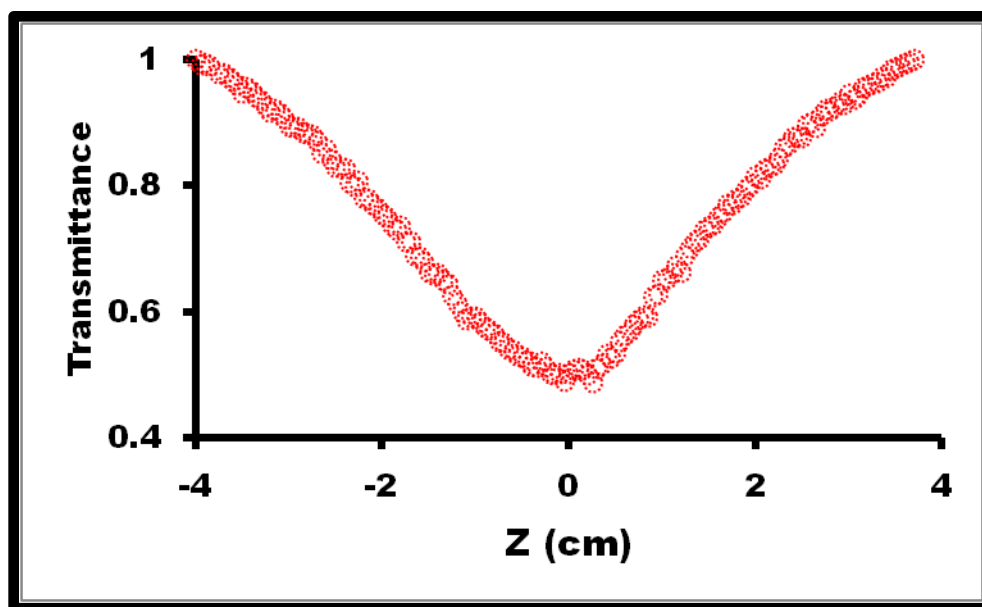
Fig 1.14: Example of an open aperture Z-scan for a compound undergoing RSA [unpublished data].

MPcs with heavy metals such as indium, lead and titanium have been found to possess a large triplet excited state due enhanced intersystem crossing, thus improving the NLO behavior of MPcs [122, 128, 136, 150]. Asymmetrical MPcs have also shown improved

NLO behavior compared to their symmetrical analogue due to their increased molecular dipole moments [151, 152]. In this work, the NLO behaviors of zinc phthalocyanine complexes with different numbers and types of substituent(s) (at either the peripheral or non-peripheral position) have been studied. The effects of the number, type and position of the substituent on the NLA behavior have been systematically studied. A detailed approach to the study has been outlined in Section 1.2.3.

1.3.2   Nonlinear Optical Parameters – equations utilized in this work

In this work, we used the open aperture set-up and the Z-Scan experiments were performed according to the method described by Sheik-Bahae et al [140, 141, 153], using equation 1.12

$$T(z) = \frac{1}{\sqrt{\pi}q_0(z)} \int_{-\infty}^{\infty} ln\left[1 + q_0(z)e^{-\tau^2}\right]d\tau \qquad (1.12)$$

where T(z) is the normalized transmittance of the sample and $q_0(z)$ is given by equation 1.13

$$q_0(z) = \beta_{eff}I_{00}L_{eff}/(1 + \frac{z^2}{z_o^2}) \qquad (1.13)$$

and L$_{eff}$ by equation 1.14

$$L_{eff} = \frac{1 - e^{-\alpha L}}{\alpha} \qquad (1.14)$$

where I_{00} is the on-focus peak input irradiance; β_{eff} is the effective non linear absorption coefficient and L_{eff}, Z and Zo are the effective path length in the sample of length L,

translation distance of the sample relative to the focus and Raleigh length, respectively. Raleigh length is defined as $\pi w_o^2/\lambda$, where λ is the wavelength of the laser beam and w_o is the beam waist at the focus (z=0). α is the linear absorption coefficient of the sample. Generally, equation 1.12 is not usually used because it is not well suited to fit experimental data directly.

A numerical form of equation 1.12, which is equation 1.15 is usually employed as a fit function to the experimental data.

$$T(z)= 0.363e^{\left(-\frac{q_0(z)}{5.60}\right)} + 0.286e^{\left(-\frac{q_0(z)}{1.21}\right)} + 0.213e^{\left(-\frac{q_0(z)}{24.62}\right)} + 0.096e^{\left(-\frac{q_0(z)}{115.95}\right)} + 0.038e^{\left(-\frac{q_0(z)}{965.08}\right)}$$

$$(1.15)$$

Another parameter related to the nonlinear absorption coefficient is the imaginary component of the third order susceptibility ($I_m[\chi^{(3)}]$), calculated using equation 1.16 [154]

$$I_m[\chi^{(3)}] = n^2\varepsilon_0 c\lambda\beta_{eff}/2\pi \qquad\qquad (1.16)$$

where n and c are the linear refractive index and the speed of light, respectively, ε_0 is the permittivity of free space, λ and β_{eff} terms are as described above.

Another term considered is the second order hyperpolarizability (γ), which gives the nonlinear absorption of per mole of compound, and is important when comparing the effectiveness of multiple compounds. The second order hyperpolarizability (γ) was determined using equation 1.17 [153, 154].

$$\gamma = \frac{I_m[\chi^{(3)}]}{f^4 C_{mol} N_A} \qquad\qquad (1.17)$$

where N_A is the Avogadro constant as defined above, C is the concentration of the active species in the triplet state per mole and f is the Lorentz local field factor given as $f = (n^2 + 2)/3$.

The limiting intensity threshold limit (I_{lim}), defines the maximum incident intensity from which the output intensity becomes relatively constant with increasing intensity. The I_{lim} may be derived from equation 1.18 [155].

$$I_{lim}=h\omega^*/2\pi\sigma_s\tau_T \hspace{4cm} \text{(1.18)}$$

where ω^*, σ_s and τ_T are the frequency of the laser, singlet state absorption cross section and triplet lifetimes respectively. The lower the I_{lim} values obtained the better the material as an optical limiter. The I_{lim} values for this work were obtained graphically from plotting incident intensities (I_o) against emergent intensities (I_{out}) of the sample.

1.4   Summary of aims of thesis

The aims of this thesis are summarized below:

1.   Syntheses, surface functionalization and characterization of SiNPs,

2.   Syntheses and characterization of symmetrical and asymmetrical metallophthalocyanine complexes (MPcs) with different substituent at the α and β positions of the Pc ring,

3.   Covalent grafting of the complexes to the surface of the SiNPs via click chemistry, ester bond and amide bond,

4.   Doping of the complexes within the silica matrix and the characterization of both the grafted and doped conjugates,

5.   Study the behavior of the silica nanoparticles-phthalocyanine conjugates in a simulated biological medium,

6. Comparative studies of the photophysical and photochemical properties of the phthalocyanine complexes and the conjugates in solution,

7. Study of the NLO behavior of the MPcs in solution and comparing NLO parameters such as incident intensity threshold limit (I_{lim}), third order susceptibility ($I_m[\chi^{(3)}]$), second-order hyperpolarizability (γ) and effective nonlinear absorption coefficient (β_{eff}), and

8. Assessing the contribution of the excited singlet state absorption (ESA) and excited triplet state absorption (ETA) to the NLA behavior of the complexes.

Chapter Two

2.   EXPERIMENTAL

This chapter provides information on the materials, instrumentation and synthetic procedures used in this work.

2.1   Materials

2.1.1   SiNPs synthesis

Tetraethyl orthosilicate (TEOS), (3-aminopropyl)-triethoxysilane (APTES), (3-chloropropyl)-triethoxysilane, succinic acid anhydride, Triton X-100 and ammonia (25%) were purchased from Sigma Aldrich. Absolute ethanol (99.5 %) was purchased from SAARCHEM. Ultra-pure water was obtained from (Milli-Q water system, Millipore Corp., Bedford, MA, USA).

2.1.2   Solvents

Dichloromethane (DCM), toluene, methanol, dimethylformamide (DMF), dimethylsulfoxide (DMSO), ethanol, tetrahydrofuran (THF), ethyl acetate, hydrochloric acid (HCl), cyclohexane, hexanol, acetonitrile, hexane and acetone were purchased from SAARCHEM. 1-Pentanol and trifluoroacetic acid (TFA) were from Sigma Aldrich.

2.1.3   MPc synthesis, conjugation to SiNPs and other reagents

Quinoline, zinc chloride (ZnCl$_2$), zinc acetate dihydrate (Zn(CH$_3$COO)$_2 \cdot$ 2H$_2$O), urea, 1,8-diazabicyclo[5.4.0] undec-7-ene (DBU), dicyclohexylcarbodiimide (DCC) (99%), dimethylamino pyridine (DMAP), deuterated dimethylsulfoxide (DMSO-d6), 5-hexyn-1-ol, phthalonitrile, copper sulphate and sodium ascorbate (C$_6$H$_7$NaO$_6$) were from Sigma Aldrich. Silica gel 60PF254 was purchased from Merck. Phenomenex reverse phase strata C18-E Sep-Pak columns (55 mm, 70A) were purchased from Phenomenex. The simulated media, artificial lysosomal fluid (ALF) was prepared according to the method described in the literature [**156**].

2.1.4   Previously synthesized phthalocyanines and their precursors

4-(3-carboxyphenoxy) phthalonitrile (**5a**) [**149**] Scheme 3.3, 3-(4-aminophenoxy) phthalonitrile (**5b**) [**157**] Scheme 3.4, 1(4), 8(11), 15(18), 22(25)-tetrakis-(3-carboxyophenoxy)phthalocyaninato zinc (II) - α-ZnT-3-CPPc (**8**) [**149**], 1(4), 8(11), 15(18), 22(25)-tetrakis-(4-carboxyophenoxy)phthalocyaninato zinc (II) -α-ZnT-4-CPPc (**9**) [**149**, **158**], 1(4), 8(11), 15(18), 22(25)-tetrakis-(4-aminophenoxy) phthalocyaninato zinc (II) - α-ZnTAPPc (**11**) [**157**], 2(3), 9(10), 16(17), 23(24)-tetrakis-(4-aminophenoxy)phthalocyaninato zinc (II) - β-ZnTAPPc (**12**) [**159**], 2(3)-Mono-(4-aminophenoxy)phthalocyaninato zinc (II) - β-ZnMAPPc (**14**) [**160**], 2(3)-Mono-(4-amino)phthalocyaninato zinc (II) - β-ZnMAPc (**15**) [**161**], 1(4)-Mono-(3-carboxyphenoxy)phthalocyaninato zinc (II) - α-ZnM-3-CPPc (**16**) [**149**], 2(3)-Mono-(3-carboxyphenoxy)phthalocyaninato zinc (II) - β –ZnM-3-CPPc (**17**) [**149**] and 1(4)-Mono-(4-carboxyphenoxy)phthalocyaninato zinc (II) - α-ZnM-4-CPPc (**18**) [**149**] were synthesized according to literature procedures. Zinc phthalocyanine (ZnPc) was purchased from Sigma Aldrich.

2.2   Instrumentation

a) Elemental analyses for CHNS were done using a Vario-Elementar Microcube ELIII Series.

b) Mass spectral data for the characterization of phthalocyanines were collected with a Bruker AutoFLEX III Smart beam TOF/TOF mass spectrometer. The instrument was operated in the positive ion mode using an m/z range of 400-3000 amu. The voltage of the ion sources were set at 19 and 16.7 kV for ion sources 1 and 2 respectively, while the lens was set at 8.50 kV. The reflector 1 and 2 voltages were set at 21 and 9.7 kV respectively. The spectra were acquired using α-cyano-4-hydroxycinnamic acid as the MALDI matrix and a 354 nm nitrogen laser as ionizing source.

c) Ground state electronic absorption spectra were recorded on a Shimadzu UV-2550 UV/Vis spectrophotometer in the range of 300 - 800 nm. Quartz cells of 1 cm path length were employed.

d) Magnetic circular dichroism (MCD) spectra were measured with a Chirascan plus spectrodichrometer equipped with a 1 T (tesla) permanent magnet by using both the parallel and anti-parallel fields.

e) Infrared (IR) spectra were recorded using either Perkin-Elmer Fourier transform–IR (100 FT-IR) or Perkin-Elmer Fourier transform-IR (2000 FT-IR) spectrophotometer.

f) Proton-nuclear magnetic resonance spectra (^{1}H-NMR) were recorded in deuterated solvent (DMSO-d_6) using either Bruker EMX400 MHz NMR spectrometer or a Bruker ADVANCE II 600 MHz spectrometer

g) Raman data was obtained using a Bruker Vertex 70-Ram II spectrometer equipped a Nd:YAG laser that emit at 1064 nm and liquid nitrogen cooled germanium detector.

h) Transmission electron microscope (TEM) micrographs for the nanoparticles were obtained using a Zeiss Libra 120 TEM operating at 80kV from ethanol solutions. The sizes of the nanoparticles were measured using the Olympus measureIT software and the size distribution plotted using Origin 8 software.

i) Thermo-gravimetric analysis (TGA) was performed using a Shimadzu simultaneous DTA-TG apparatus (DTG-60A) or a Perkin Elmer TGA 4000 analyzer. The analysis was carried out under nitrogen at a flow rate of 120 cm^{-3} min^{-1}. The weighed sample masses were heated from 100 to 800 ^{0}C at a heating rate of 10 ^{0}C min^{-1}.

j) X-ray photoelectron spectroscopy (XPS) was done using a Kratos Axis Ultra DLD, using an Al (monochromatic) anode, equipped with charge neutralizer and the operating pressure kept below 5 x10^{-9} torr. For wide/survey XPS scans, the following parameters were used: emission current was kept at 10 mA and the anode (HT) voltage at 15 kV. The resolution used to acquire wide/survey scans was at 160 eV pass energy using a hybrid lens in the slot mode. The center used for the scans was at 520 eV and the width at 1205 eV, with steps at 1 eV and dwell times at 300 ms. For the high resolution scans, the resolution was changed to 40 eV pass energy

in the slot mode. For the N1s spectra, the center was kept at 402 eV and the width at 12 eV, with a step size at 0.1 eV and dwell time at 500 ms.

k) X-ray powder diffraction patterns were recorded on a Bruker D8 Discover equipped with a proportional counter, using Cu-K$_\alpha$ radiation (λ = 1.5405 Å, nickel filter). Data were collected at various 2θ ranges, scanning at 1° min-1 with a filter time-constant of 2.5 s per step and a slit width of 6.0 mm. Samples were placed on a zero background silicon wafer slide. The X-ray diffraction (XRD) data were treated using Eva (evaluation curve fitting) software. Baseline correction was performed on each diffraction pattern by subtracting a spline fitted to the curved background and the full-width at half-maximum values used in this study were obtained from the fitted curves.

l) Fluorescence emission and excitation spectra were obtained on a Varian Eclipse spectrofluorimeter.

m) Fluorescence lifetime measurements were carried out using a time correlated single photon counting (TCSPC) setup (FluoTime 200, Picoquant GmbH), Fig. 2.1. The excitation source was a diode laser (LDH-P-670 driven by PDL 800-B, 670 nm, 20 MHz repetition rate, Picoquant GmbH). Fluorescence was detected under the magic angle with a peltier cooled photomultiplier tube (PMT) (PMA-C 192-N-M, Picoquant) and integrated electronics (PicoHarp 300E, Picoquant GmbH). A monochromator with a spectral width of about 4 nm was used to select the required emission wavelength band. A scattering Ludox solution (DuPont) was used to measure the response function of the system and had a full width at half maximum (FWHM) of about 280 ps. To obtain good statistics, the ratio of stop to start pulses was kept low (below 0.05). Measurement of the entire luminescence decay curve (range 0 to 200 ns) was at the maximum of the emission peak. Data analysis was done using the program Fluofit (Picoquant GmbH). Estimation of the decay error times was carried out using the support plane approach [90].
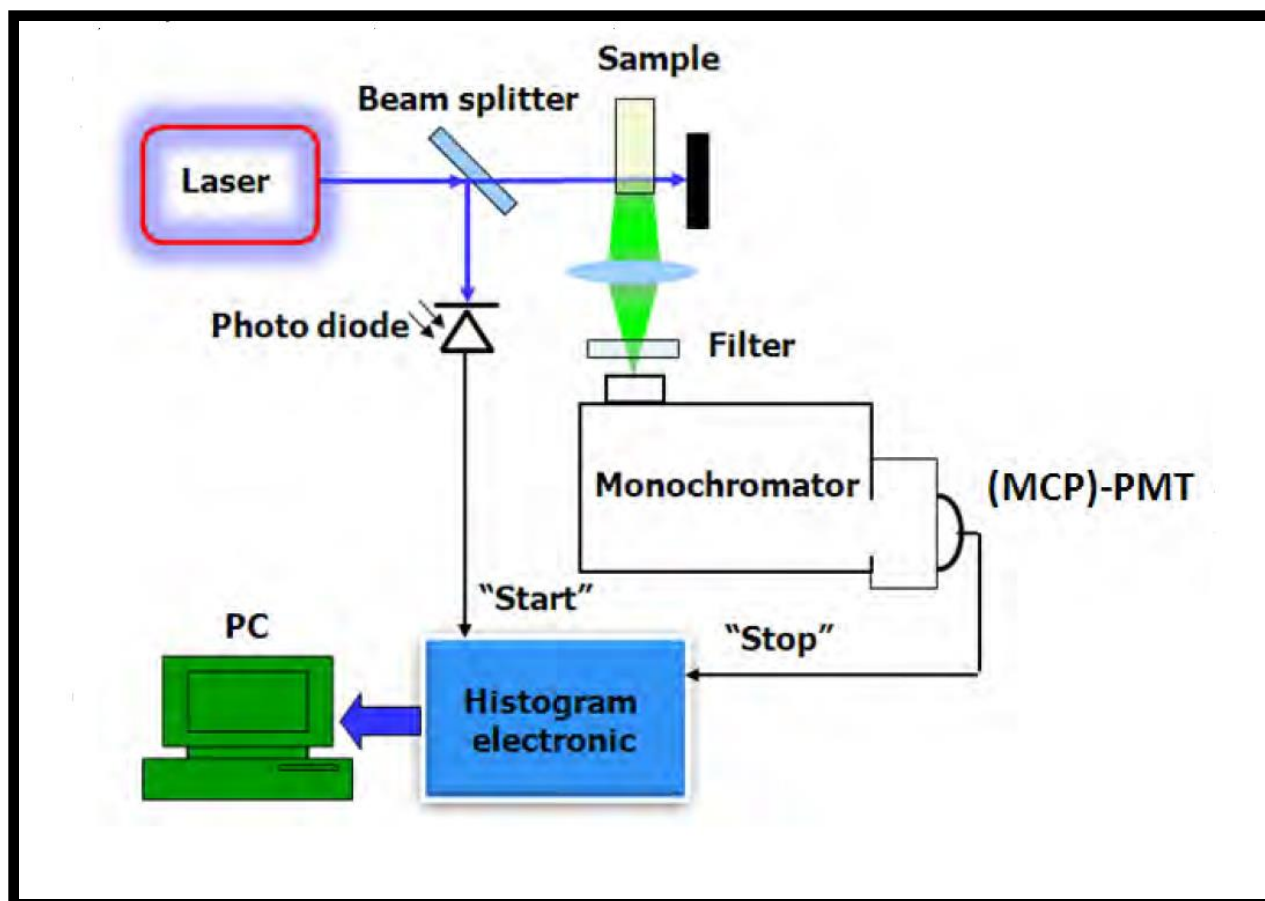
Figure 2.1: Schematic diagram of time-correlated single photon counting (TCSPC) setup. (MCP)-PMT = (Multi channel plate detector)-Photomultiplier tube, PC = Personal computer

n) Laser flash photolysis experiments, Fig. 2.2, were performed with light pulses produced by a Quanta-Ray Nd:YAG laser providing 400 mJ, 9 ns pulses of laser light at 10 Hz, pumping a Lambda-Physik FL3002 dye laser (Pyridin 1 dye in methanol). Single pulse energy ranged from 2 to 7 mJ. The analyzing beam source was from a Thermo Oriel Xenon arc lamp, and photomultiplier tube (a Kratos Lis Projekte MLIS-X3) was used as a detector. Signals were recorded with a two channel 300 MHz digital real time oscilloscope (Tektronix TDS 3032C); the kinetic curves were averaged over 256 laser pulses.
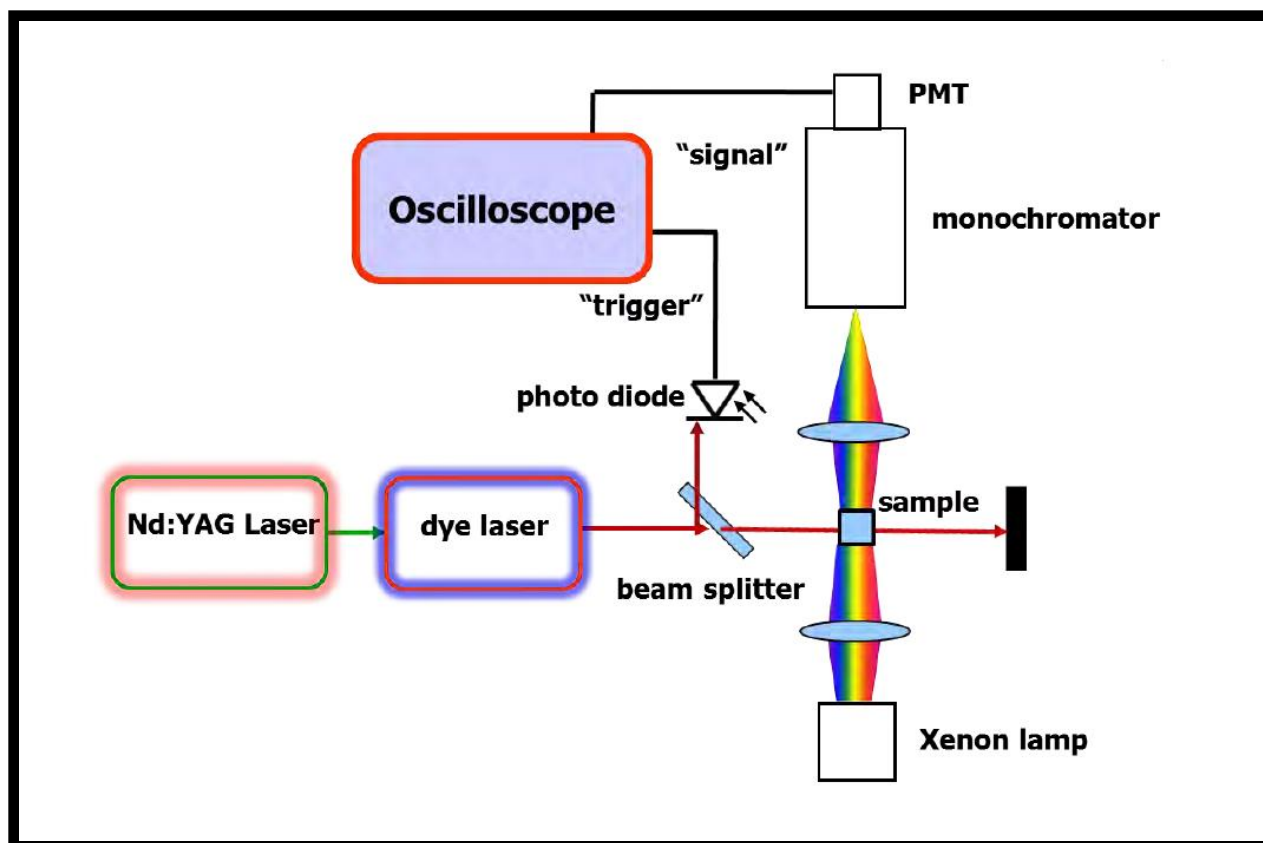
Figure 2.2: Schematic diagram for a laser flash photolysis setup. PMT = Photomultiplier tube

o) Time resolved phosphorescence decay of singlet oxygen at 1270 nm was used to determine singlet oxygen quantum yield in either DMF or THF. The dynamic phosphorescence decay of singlet oxygen (O_2 ($^1\Delta_g$)), was demonstrated using time resolved phosphorescence of O_2 ($^1\Delta_g$) at 1270 nm. For these studies an ultra sensitive germanium detector (Edinburgh Instruments, EI-P) combined with a 1000 nm long pass filter (Omega, RD 1000 CP) and a 1270 nm band-pass filter (Omega, C1275, BP50) was used to detect O_2($^1\Delta_g$) phosphorescence under the excitation using Quanta-Ray Nd:YAG laser providing 400 mJ, 90 ns pulses of laser light at 10 Hz pumping a Lambda-Physik FL3002 dye laser (Pyridin 1 dye in methanol), with a pulse period of 7 ns and repetition rate of 10 Hz. The near-infrared phosphorescence of the samples were focused onto the germanium detector by a lens (Edmund, NT 48-157) with detection direction perpendicular to the excitation laser beam. The

detected signals were averaged with a digital oscilloscope (Tektronics, TDS 360) to show the dynamic decay of O_2 $(^1\Delta_g)$.

p) The Brunauer-Emmett Teller (BET) method was employed to determine surface area and porosity. Nitrogen adsorption/desorption isotherms were measured at 77 K using a Micromeritics ASAP 2020 Surface Area and Porosity Analyzer. Prior to each measurement, degassing was carried at 90 ^{o}C for four days. The BET surface area and total pore volume were calculated from the isotherms obtained.

q) The Z-scan equipment employed in this work was fabricated at the University of Stellenbosch in South Africa. All Z-scan experiments described in this study were performed using a frequency-doubled Nd:YAG laser (Quanta-Ray, 1.5 J/10 ns fwhm pulse duration) as the excitation source. The laser was operated in a near Gaussian transverse mode at 532 nm (second harmonic), with a pulse repetition rate of 10 Hz and an energy range of 0.1 µJ–0.1 mJ, limited by the energy detectors (Coherent J5-09). The low repetition rate of the laser prevents cumulative thermal nonlinearities. The beam was spatially filtered to remove the higher order modes and tightly focused with a 15 cm focal length lens. The Z-scan system size (l × w × h) used was 600 mm × 300 mm × 350 mm (excluding the computer, energy meter, translation stage driver and laser system). The liquid samples were placed in a cuvette (internal dimensions: 2 mm × 10 mm × 55 mm, 0.7 mL) and a path length of 2 mm (Starna 21-G-2).

r) Dissolution studies were conducted using inductively coupled plasma optical emission spectrometry (ICP-OES), (Thermo Electron Corp. ICAP 6000 series). The analysis was carried out in duplicates and three wavelengths (212.4, 251.6 and 288.1 nm) were selected to determine the silicon content in the simulated media.

2.3   Synthesis of functionalized SiNPs, Schemes 3.1 and 3.2

The uncapped SiNPs were synthesized according to a reported procedure [**19, 20**].

The amino-functionalized SiNPs (SiNPs-NH$_2$), carboxyl-functionalized (SiNPs-COOH) and the azide-functionalized SiNPs (SiNPs-N$_3$) were synthesized according to literature procedures [**27, 162-164**]. For amino-functionalized SiNPs (SiNP-NH$_2$), 1g of uncapped SiNPs was dispersed in a mixture of toluene (7 ml) and APTES (1.5 ml) and the mixture was stirred at 60°C for 5 h. The resulting SiNPs was obtained by centrifugation and washed several times with ethanol and acetonitrile. The SiNPs-NH$_2$ obtained was air dried in the fume hood, Scheme 3.1.

The carboxyl-functionalized SiNPs (SiNPs-COOH) were synthesized by adding 1g of SiNP-NH$_2$ in DMF to 30 ml of 0.1M succinic acid anhydride. The mixture was stirred for 24 h, the resulting SiNP-COOH were obtained by centrifugation and washed several times using DMF, Scheme 3.1. The SiNPs-COOH obtained were air dried in the fume hood.

3-Azidopropyltriethoxysilane used for functionalizing uncapped SiNPs was prepared from 3-chloropropyltriethoxysilane according to literature procedures [**163, 164**].

The azide-functionalized SiNPs (SiNPs-N$_3$) was synthesized by adding 2ml of 3-azidopropyltriethoxysilane to a solution containing 1 g of uncapped SiNPs dispersed in 30 ml of toluene. The reaction mixture was heated under reflux for 24 h, Scheme 3.2. The resulting SiNPs-N$_3$ was obtained by centrifugation and washed several times using DCM. The SiNPs-N$_3$ obtained was air dried in the fume hood.

2.4   Syntheses of Phthalocyanines

2.4.1   2(3), 9(10), 16(17), 23(24)-tetrakis-(3-carboxyphenoxy)phthalocyaninato zinc (II) - β-ZnT-3-CPPc (10) – Scheme 3.3

The synthesis of 4-(3-carboxyphenoxy) phthalonitrile (**5a**) has been reported [**149**].

A mixture of Zn chloride (181 mg, 1.33 mmol), 4-(3-phenoxycarboxy) phthalonitrile, (**5a**) (351 mg, 1.33 mmol) and urea (1.5 g 11.61 mmol) in quinoline (3 ml) was refluxed for 7 h under nitrogen atmosphere. After cooling, the crude product was precipitated with methanol, filtered and washed with excess methanol, ethanol, 1 M HCl and water to obtain a clean product.

Yield: 5%. IR [(KBr) v_{max}/cm^{-1}]: 745, 825, 950, 1043 (Pc ring), 1224, 1333, 1390 (C–O–C), 1660 (C=O), 2160, 2536 (C-H, aromatic), 3340 (0-H). UV-Vis (DMSO): λ_{max}/nm (log ε): 356 (5.19), 611 (4.82), 681 (5.46), calcd for $C_{60}H_{32}N_8O_{12}Zn.4H_2O$; C 60.30, H 3.35, N 9.37. Found C 60.15, H 3.96, N 9.52 %; ^{1}H NMR (DMSO-d_6): δ, ppm 13.12 (4H, s, carboxylic), 8.09 – 8.90 (12H, m, Pc-H), 7.59 – 7.87 (16H, m Phenyl-H). MS (MALDI-TOF) (m/z): calc. 1122; found: 1123 [M + H]$^+$.

2.4.2   1-Mono-(4-aminophenoxy)phthalocyaninato zinc (II) - α-ZnMAPPc (13) - Scheme 3.4

The synthesis of 3-(4-aminophenoxy) phthalonitrile, (**5b**) has been reported [**160**].

A mixture of Zn acetate dihydrate (286 mg, 1.30 mmol), phthalonitrile (500 mg, 3.91 mmol) and 3-(4 aminophenoxy) phthalonitrile (**5b**) (302 mg, 1.30 mmol) in DMF (2.5 ml) was refluxed for 7 h under nitrogen atmosphere in the presence of two drops of DBU as catalyst. After cooling, the crude product was precipitated with methanol, filtered and washed with excess methanol and then dried in air. The product was further purified using a reverse phase C18 Sep-Pak column with 0.05% of TFA in methanol as the eluting solvent.

Yield: 13%. IR [(KBr) v_{max}/cm^{-1}]: 3200 - 3056 (N-H str.), 1602 (NH bend), 1086 (C–O–C), 1472, 1363 and 1314 (C-N). UV-Vis (DMSO): λ_{max}/nm (log ε): 365 (4.80), 610 (4.60), 681 (5.17), calcd for C$_{38}$H$_{21}$N$_9$OZn. 3CH$_3$OH; C 63.04, H 4.26, N 16.14. Found C 62.81, H 3.81, N 15.71 %; ^{1}H NMR (DMSO-d$_6$): δ, ppm 9.08 – 9.19 (4H, m, Ph-H), 7.75 – 8.12 (4H, m, Pc-H), 7.37 – 7.68 (8H, m Pc-H), 6.89 – 7.03 (3H, m, Pc-H), 6.62 (2-H, br, N-H). MS (MALDI-TOF) (m/z): calc. 684; found: 686 [M + 2H]$^+$.

2.4.3   1-Mono-(3-((hex-5-ynyl)-benzoate)-1(4)-phenoxy)phthalocyaninato zinc (II) - α-ZnM-3-CAPc **(19) - Scheme 3.5A**

Phthalocyanine complex **19 (α-ZnM-3-CAPc)** was derivatized from complex **16** (α-ZnM-3-CPPc) **[149]** as follows: A mixture of **16** (16.7 mg, 0.02 mmol)**,** DCC (4.35 mg, 0.002 mmol), and DMAP (2.6mg, 0.02mmol) in DMF (4 ml) was stirred for 24 h. After activating the carboxylic group for 24 h, 5-hexyn-1-ol (2.29 mg, 0.02 mmol) was added to the mixture. The reaction was left stirring for 10 days and the product was then extracted with 1:1 DCM and water. The extracted product was allowed to dry in the fume hood, dissolved in DCM and then subjected to column chromatography using hexane/ethyl acetate (3:2) as eluent to obtain a clean product.

Yield: 58%. IR [(KBr) v_{max}/cm^{-1}]: 775, 891, 980, 1088 (Pc ring), 1115, 1186, 1242, 1309 (C–O–C), 1726 (C=O), 2160 (C≡C) 2850, 2926 (C-H, methylene), 3322 (C-H, alkyne). UV-Vis (DMSO): λ_{max}/nm (log ε): 610 (4.77), 677 (5.36). ^{1}H NMR (DMSO-d$_6$): δ, ppm 9.33-9.36 (4H, m Phenyl-H), 7.94-8.36 (15H, m, Pc-H), 4.13–4.15 (2H, t methylene - H), 2.24-2.62(6H, m, methylene-H), 1.92 (1H, s, acetylene-H). MS (MALDI-TOF) (m/z): calc. 794; found: 796 [M + 2H]$^+$.

2.4.4 2-Mono-(3-((hex-5-ynyl)-benzoate)-2(3)-phenoxy)phthalocyaninato zinc (II)- β-ZnM-3-CAPc **(20) - Scheme 3.5B**

Phthalocyanine complex **20** (β -ZnM-3-CAPc) was synthesized and purified as described above for **19**, except that **17** instead of **16** was employed as the starting material. The amounts employed were the same.

Yield: 46%. IR [(KBr) v_{max}/cm^{-1}]: 751, 887, 959, 1054 (Pc ring), 1111, 1161, 1228, 1282 (C–O–C), 1713 (C=O), 2161 (C≡C) 2851, 2924 (C-H, methylene), 3320 (C-H, alkyne). UV-Vis (DMSO): λ_{max}/nm (log Ɛ): 611 (4.43), 674 (5.15). ^{1}H NMR (DMSO-d$_6$): δ, ppm 9.36 – 9.39 (4H, m Phenyl-H), 7.49 – 8.26 (15H, m, Pc-H), 5.23 – 5.31 (2H, t methylene - H), 2.05 – 2.48 (6H, m, methylene-H), 1.83 (1H, s, acetylene-H). MS (MALDI-TOF) (m/z): calc. 794; found: 796 [M +2H]$^+$.

2.4.5 1-Mono-(4-((hex-5-ynyl)-benzoate)-1(4)-phenoxy)phthalocyaninato zinc (II)- α-ZnM-4-CAPc **(21) - Scheme 3.5C**

Phthalocyanine complex **21 (**α-ZnM-4-CAPc**)** was synthesized and purified as described above for **19**, except that **18** instead of **16** was employed as the starting material. The amounts employed were the same.

Yield: 58%. IR [(KBr) v_{max}/cm^{-1}]: 750, 842, 973, 1090 (Pc ring), 1113, 1166, 1245, 1330 (C–O–C), 1724 (C=O), 2160 (C≡C) 2852, 2926 (C-H, methylene), 3275 (C-H, alkyne). UV-Vis (DMSO): λ_{max}/nm (log Ɛ): 611 (4.65), 677 (5.22). ^{1}H NMR (DMSO-d$_6$): δ, ppm, 9.21 – 9.28 (4H, m Phenyl-H), 7.36 – 8.14 (15H, m, Pc-H), 5.23 – 5.31 (2H, t methylene - H), 2.26 – 2.72 (6H, m, methylene-H), 1.22 (1H, s, acetylene-H). MS (MALDI-TOF) (m/z): calc. 794; found: 797 [M + 3H]$^+$.

2.5   Conjugation

2.5.1   Conjugation of MPcs (8-10) to SiNPs-NH₂ for amide bond formation - Scheme 3.6

The conjugates were synthesized by dissolving 0.5 mg (0.00045 mmol) of **8 (**α-ZnT-3-CPPc), **9 (**α-ZnT-4-CPPc**)** or **10 (**β-ZnT-3-CPPc**)** in 5 ml of DMF. Then 15 mg (0.073 mmol) of dicyclohexylcarbodiimide (DCC) was added and the resulting solution was stirred for 2 h. This was done to activate the carbonyl of the carboxylic acid functional group for amide bond formation. Afterwards, 0.7 mg (0.0057 mmol) of dimethylaminopyridine (DMAP) and 0.25 g of SiNPs-NH₂ were added and the reaction was stirred for 24 h at room temperature. The nanoparticles were obtained by centrifuging at 3500 rpm for 10 min, while the Pc remained in the DMF solution as the supernatant and washed thrice with ethanol. The choice of ethanol as a washing solvent is due to the solubility of DCC and DMAP in ethanol. The product was allowed to dry for 24 h in the fume hood. The linked conjugates are represented as **8-SiNPs** (linked amide) or **9-SiNPs** (linked amide) or **10-SiNPs** (linked amide). Similar experiments were also performed where **8** (α-ZnT-3-CPPc), **9** (α-ZnT-4-CPPc) or **10** (β-ZnT-3-CPPc) were simply mixed with SiNPs-NH₂ without coupling agents. The mixed complexes are represented as **8-SiNPs** (mixed) or **9-SiNPs** (mixed) or **10-SiNPs** (mixed).

2.5.2   Conjugation of MPcs (11-15) to SiNPs-COOH for amide bond formation - Scheme 3.7

The method used is similar to the one described in section 2.5.1 except that DCC and DMAP were used to activate the carboxylic groups on the surface of the SiNPs. SiNPs-COOH (0.15g) was dispersed in 5 mL of DMF, then 40 mg (0.194 mmol) of DCC was added, followed by 0.7 mg (0.0057 mmol) of DMAP. The resulting solution was stirred for 24 h. After 24 h, each of complexes **11 or 12 (**6.1 mg, 0.0061 mmol), or **13** or **14** (6.1 mg, 0.00891 mmol), or **15** (6.1 mg, 0.0102 mmol) were added to the SiNPs suspension

and the mixture was stirred for 24 h at room temperature. The purification procedure is same as described in section 2.5.1. The linked conjugates are represented as **11-SiNPs** (linked), **12-SiNPs** (linked amide), **13-SiNPs** (linked amide), **14-SiNPs** (linked amide) or **15-SiNPs** (linked amide). Similar experiments were also performed where each of **11 (α-**ZnTAPPc**)**, **12 (**β-ZnTAPPc**)**, **13** (α-ZnMAPPc), **14** (β-ZnMAPPc) or **15** (β-ZnMAPc) were simply mixed with **SiNPs-COOH** without coupling agents. The mixed complexes are represented as **11-SiNPs** (mixed) or **12-SiNPs** (mixed) or **13-SiNPs** (mixed) or **14-SiNPs** (mixed) or **15-SiNPs** (mixed).

2.5.3   Conjugation of MPcs (8 and 9) to uncoated SiNPs for ester bond formation – Scheme 3.8

The approach used is similar to the one described in section 2.5.1 except that silica nanoparticles used are uncoated. The purification procedure and amounts used are same as described in section 2.5.1. The linked conjugate is represented as **8-SiNPs** (linked ester) or **9-SiNPs** (linked ester). Similar experiments were also performed where each of **8 (α-ZnT-3-CPPc**) or **9 (α-ZnT-4-CPPc)** was simply mixed with **SiNPs** without coupling agents. The mixed complexes are represented as **8-SiNPs** (mixed) or **9-SiNPs** (mixed).

2.5.4   Conjugation of MPcs (19-21) to SiNPs-N$_3$ via click chemistry- Scheme 3.9

A slight modification to previously reported click chemistry approach was employed [**165, 166**]. For the conjugation, a mixture of 25.3 mg SiNPs-N$_3$, 9.2 mg (0.012 mmol) of **19**, **20** or **21**, 0.09 mg (0.0006 mmol) of CuSO$_4$, 0.23 mg (0.0012 mmol) of C$_6$H$_7$NaO$_6$ in 5 ml of THF and water (1:1) was stirred at room temperature for 24 h. The colored hybrid particles were obtained as a solid by centrifuging at 3500 rpm for 10 min while the

unlinked Pc remained in the THF/water solution as the supernatant. The solid nano-conjugates were then washed several times with ethanol, water and acetone. The samples were air dried in the fume hood. The linked conjugates are represented as **19-SiNPs** (linked click), **20-SiNPs** (linked click) or **21-SiNPs** (linked click).

The mixed samples were prepared using the same amount of starting materials as stated above for the linked conjugates, but in the absence of $CuSO_4$ and $C_6H_7NaO_6$. The mixed conjugates are represented as **19-SiNPs** (mixed), **20-SiNPs** (mixed) or **21-SiNPs** (mixed).

2.5.5   Doping of MPcs (8-10) with the SiNPs - Scheme 3.10

The doped silica nanoparticles were synthesized based on a slight modification to the microemulsion protocol reported in literature [**167**].

The preparation was carried out as follows, under vigorous stirring, 160 μL of 0.0098 mmol of complex **8**, **9** or **10** in DMF was added to a liquid system containing 1.77g of Triton X-100, 1.6 ml of hexanol, 400 μL of water, 60 μL of NH_3. After 30 minutes, 100 μL of TEOS was added and the reaction was allowed to stir for 24 h to produce a Pc-rich core. After 24 h, 100 μL of TEOS was added drop wise to provide an additional shell that protects the core and Pcs within it. The reaction was allowed to stir for another 24 h followed by addition of ethanol to break the microemulsion and recover the particles via centrifugation. The particles were washed two times with ethanol and one time with water. Ultrasonication was performed while washing the SiNPs in order to remove any physically absorbed dyes from the surface of SiNPs. The doped SiNPs is represented as **8-SiNPs** (doped), **9-SiNPs** (doped) or **10-SiNPs** (doped)**.

2.6   Dissolution studies of the conjugates in artificial lysosomal fluid (ALF)

The MPcs-SiNPs conjugates were incubated in artificial lysosomal fluid for up to 96 h and at concentrations of 0.2 or 2 mg/mL following the literature methods reported for silver nanoparticles [**168**].

2.7   Photophysichemical methods

2.7.1   Fluorescence quantum yields (Φ_F)

Fluorescence quantum yields (Φ_F) of the MPcs and conjugates were determined using a comparative method in DMSO, Equation 1.4. Unsubstituted ZnPc (Φ_F = 0.20) [**95**] in DMSO was employed as a standard. Both the samples and the standard were excited at the same wavelength. The absorbances of the solutions at the excitation wavelength were about 0.05 to avoid any inner filter effects.

2.7.2   Triplet quantum yields (Φ_T) and lifetimes (τ_F)

The decay kinetics of the triplet absorption of the phthalocyanine complexes and conjugates were recorded using a laser flash photolysis setup. The absorbance of sample solutions and that of the standard were adjusted to be approximately 1.5 at their Q-band maximum. After introducing the solution to a 1 cm quartz cell, argon was bubbled through the solution for 30 minutes to remove dissolved oxygen before taking readings. The triplet quantum yields of the sample phthalocyanines were determined using equation 1.5. Unsubstituted ZnPc in DMSO Φ_T^{Std}= 0.65 [**96**]. Triplet lifetimes were determined from the kinetic data obtained, using ORIGIN Pro 8 software.

2.7.3   Singlet oxygen quantum yield (Φ_Δ)

The determination of Φ_Δ was achieved by employing an optical chemical method. The optical method involves the observation of the fluorescence kinetic decay of the singlet oxygen generated at 1270 nm in air. The singlet oxygen quantum yield (Φ_Δ) determinations for the MPcs and conjugates were carried out in DMSO. For MPc or conjugates in aqueous solution, sodium azide (NaN_3) was used as singlet oxygen quencher. The dynamic course of the singlet oxygen concentrations were clearly recorded following equation 1.8. The Φ_Δ values were then determined using equation 1.9 and employing unsubstituted ZnPc in DMSO (Φ_Δ^{Std} = 0.67) [105]) as a standard.

Results and Discussions

3. Synthesis and characterization

4. Photophysical and photochemical properties

5. Nonlinear optics

6. Dissolution Studies

7. Conclusions and future prospects

Publications

The results presented in the following chapters have either been published or submitted for publication. These articles are not referenced in this thesis.

1. **Adedayo Fashina**, Edith Antunes and Tebello Nyokong, Characterization and photophysical behavior of phthalocyanines when grafted onto silica nanoparticles. *Polyhedron*, 53 (2013) 278.

2. **Adedayo Fashina**, Edith Antunes and Tebello Nyokong, Silica nanoparticles grafted with phthalocyanines: photophysical properties and studies in artificial lysosomal fluid. *New J. Chem.*, 37 (2013) 2800.

3. **Adedayo Fashina**, Edith Antunes and Tebello Nyokong, A comparative photophysicochemical study of mono-substituted phthalocyanines grafted onto silica nanoparticles. *J. Porphyrins Phthalocyanines* 18 (2014) 1

4. **Adedayo Fashina**, Edith Antunes and Tebello Nyokong, Photophysical behavior of Zn aminophenoxy substituted phthalocyanine conjugates with carboxylic acid-coated silica nanoparticles: Effect of point of substitution. *J. Mol. Struct.* 1068 (2014) 245.

5. **Adedayo Fashina**, Edith Amuhaya and Tebello Nyokong, A comparative photophysicochemical study of phthalocyanines encapsulated in core–shell silica nanoparticles. *Spectrochim. Acta Part A*, 137 (2015) 294.

6. **Adedayo Fashina**, Edith Amuhaya and Tebello Nyokong, Synthesis, Characterization and physicochemical studies of newly derivatized mono-substituted phthalocyanines grafted to Silica nanoparticles via click chemistry. *Spectrochim. Acta Part A*, in press.

7. **Adedayo Fashina** and Tebello Nyokong, Nonlinear optical responses of tetra and mono-substituted zinc phthalocyanine complexes. *Opt. Mat.*, Submitted 11-11-2014.

Chapter Three

3.   Synthesis and characterization

This chapter reports on the synthesis and characterization of SiNPs, MPcs and SiNPs-MPc conjugates

3.1.   SiNPs (SiNPs-NH₂, SiNPs-COOH and SiNPs-N₃)

3.1.1.   Syntheses

The surface functionalized SiNPs employed in this work were synthesized using the Stober protocol [**19, 20**]. The uncapped SiNPs were silanized with APTES to yield SiNPs-NH₂, Scheme 3.1, step 1. The SiNPs-NH₂ obtained from step 1 was further treated with succinic anhydride in DMF to obtain SiNPs-COOH, Scheme 3.1, step 2. The SiNPs-N₃ was obtained by reacting 3-azidopropyltriethoxysilane with uncapped SiNPs, Scheme 3.2. The surface functionalization of the nanoparticles facilitates the covalent grafting of the MPcs to the nanoparticle surface.
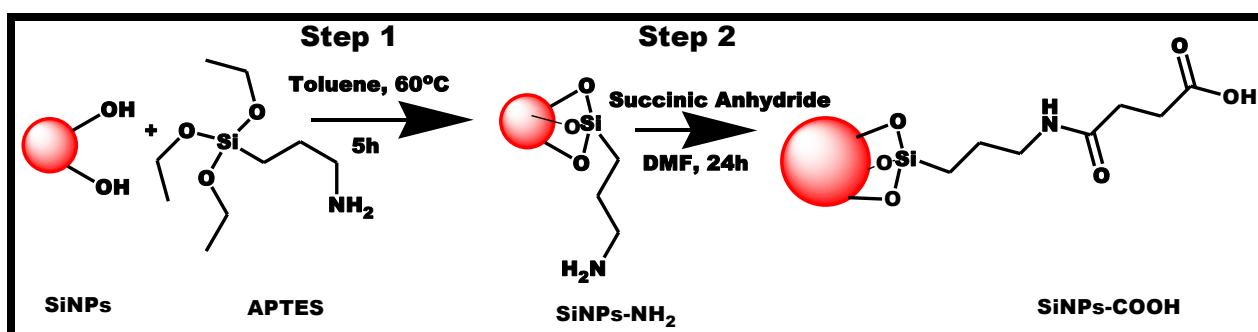
Scheme 3.1: Syntheses of amino functionalized silica nanoparticles (SiNPs-NH₂) and carboxylic acid functionalized SiNPs (SiNPs-COOH). APTES= 3-aminopropyl triethoxysilane.
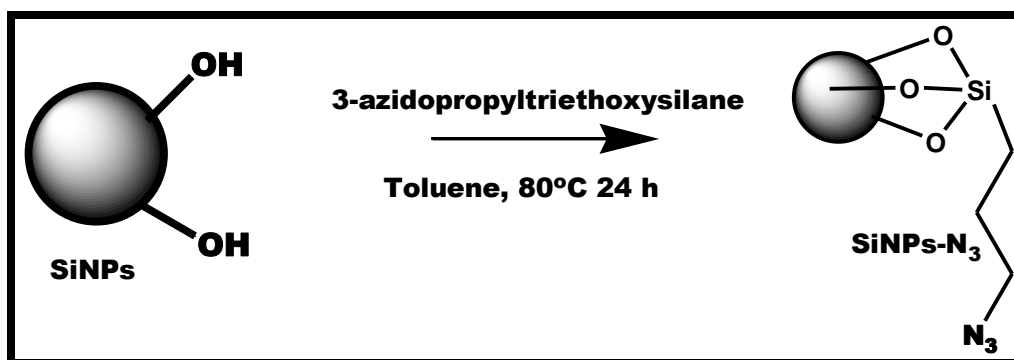
Scheme 3.2: Synthesis of azide functionalized silica nanoparticles (SiNPs-N₃).

3.1.2. Characterization

3.1.2.1.   XRD

X-ray powder diffraction (XRD) was employed to provide information about the nature of SiNPs nanoparticles synthesized in this work. Fig. 3.1 shows the XRD pattern of SiNPs-COOH as a representative of SiNPs synthesized.
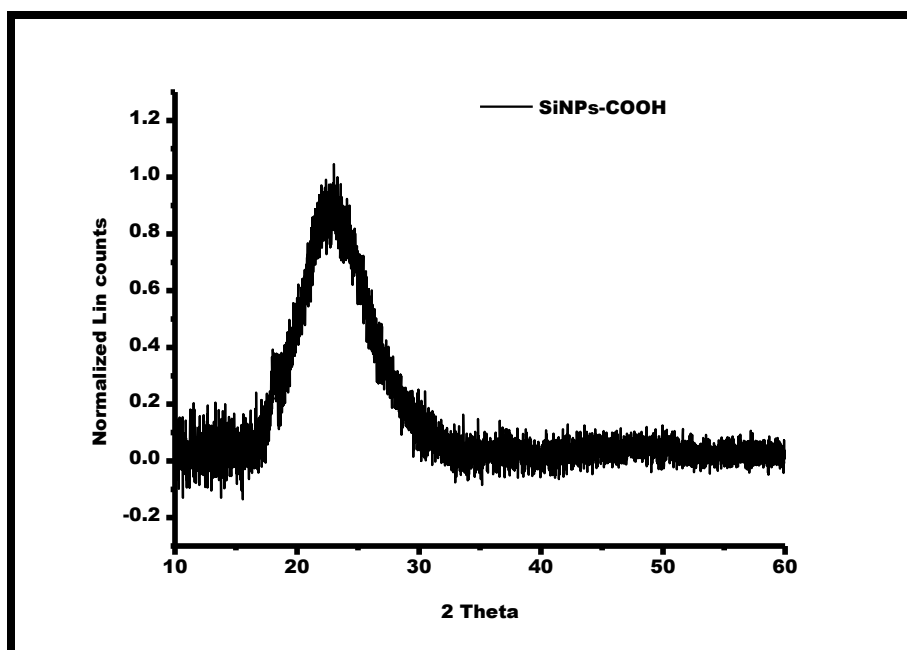
Fig. 3.1: Powder XRD spectrum of SiNPs-COOH.

The XRD spectrum show a broad peak centred at $2\theta = 22.4°$ for the SiNPs-COOH. The broad peak reflects that the nanoparticles are amorphous in nature [**57, 58, 169**]. Similar broad peaks were obtained for the other nanoparticles (uncapped SiNPs, SiNPs-NH$_2$ and SiNPs-N$_3$) synthesized in this work. The peaks for the nanoparticles were centred at $2\theta = 23.0°$, $22.0°$ and $22.4°$ for SiNPs, SiNPs-NH$_2$ and SiNPs-N$_3$ respectively.

3.1.2.2.   TEM measurements

The size and morphology of the nanoparticles studied in this work were assessed using transmission electron microscope (TEM). Fig 3.2A and 3.2B show examples of the TEM images of the SiNPs and their respective size distribution.
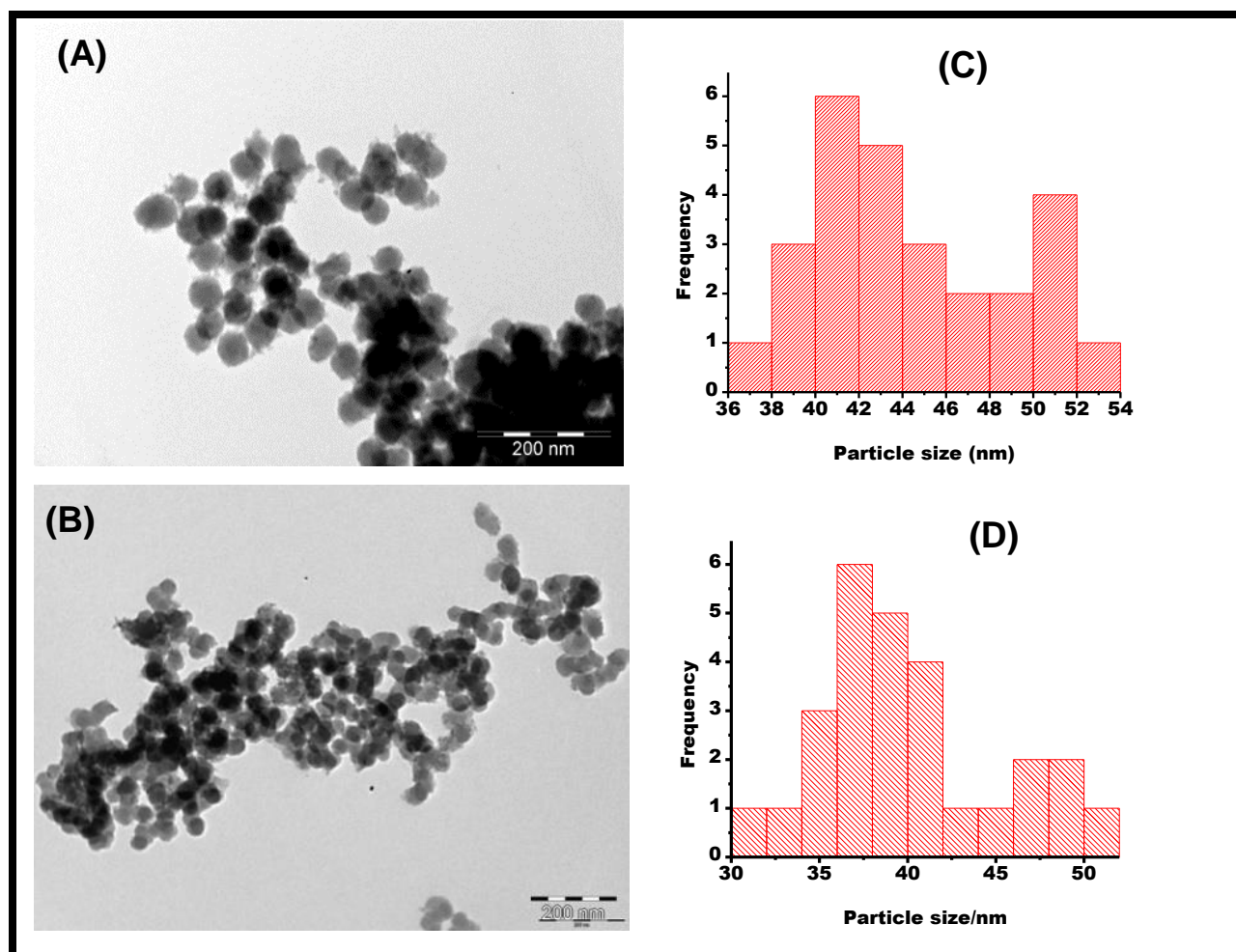
Fig. 3.2: TEM images for uncapped SiNPs (A), SiNPs-N₃ (B) and their corresponding histogram (C and D).

The TEM images of the uncapped SiNPs (Fig 3.2A) and SiNPs-N₃ (Fig. 3.2B) show that the particles are spherical in shape and are slightly aggregated, more in the case of SiNPs-N₃. Similar spherical shaped particles were obtained for the rest of nanoparticles

employed in this work. The corresponding histogram of the nanoparticles is shown in Fig 3.2C and D. The particle size distribution of the functionalized nanoparticles employed in this work is shown in Table 3.1.

Table 3.1: Particle size distribution of the functionalized nanoparticles.

SiNPs	Size range (nm)
Uncapped SiNPs	36 - 54
SiNPs-NH$_2$	39 - 54
SiNPs-COOH	10 - 35
SiNPs-N$_3$	30 - 60

3.1.2.3.   FTIR spectra

The functional groups on the surface of the functionalized SiNPs were assessed using the FTIR. Fig. 3.3 shows a representative FTIR spectra of two of the nanoparticles (SiNPs and SiNPs-COOH) employed in this work. The spectrum for the SiNPs, Fig. 3.3A, showed the following peaks: the Si-OH peak at ~3400 cm^{-1}, Si- O-Si peak at ~1039 cm^{-1}, and the Si-O peak at ~794 cm^{-1}. The SiNPs-COOH, Fig. 3.3B, also showed the carbonyl peak at 1662 cm^{-1} in addition to the other characteristic silica peak (Si-O and Si-O-Si) [170]. For the SiNPs-NH$_2$, the N-H peaks were observed at 1636 cm^{-1} and 3380 cm^{-1} while the characteristic N$_3$ peak of the SiNPs-N$_3$ was observed at 2101 cm^{-1} [171].
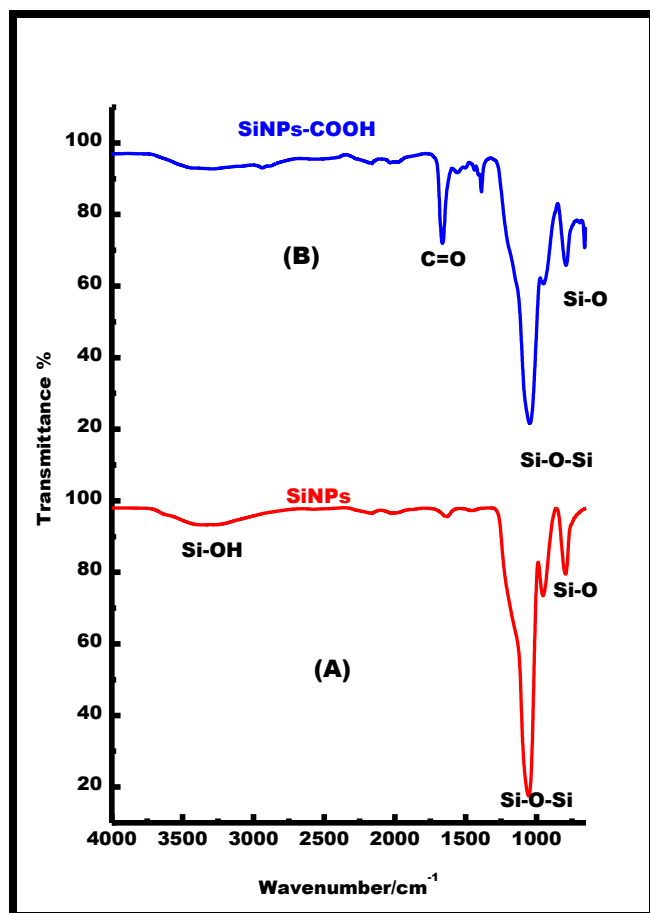
Fig. 3.3: FT-IR spectra of SiNPs alone (A) and SiNPs-COOH (B)

3.1.2.4.   Thermogravimetric (TGA) Analysis

The thermal stability of the nanoparticles was assessed using the TGA, Fig. 3.4. The TGA curve for the SiNPs, Fig. 3.4, show an approximate 2.0% weight loss from 120-180 $^{\circ}$C and a further loss of approximately 1.3% from 320 $^{\circ}$C - 550 $^{\circ}$C. Processes that may be taking place as the temperature increases include the elimination of adsorbed water, oxidation of residual organics and relaxation of the silica matrix [**172, 173**]. Similar thermogravimetric curves were obtained for SiNPs-NH$_2$, SiNPs-COOH and SiNPs-N$_3$. The approximate total % weight losses observed in the other nanoparticles synthesized are as follow: 3.5%, 21.0% and 33.5% for SiNPs-NH$_2$ SiNPs-COOH and SiNPs-N$_3$ respectively at 550 $^{\circ}$C.
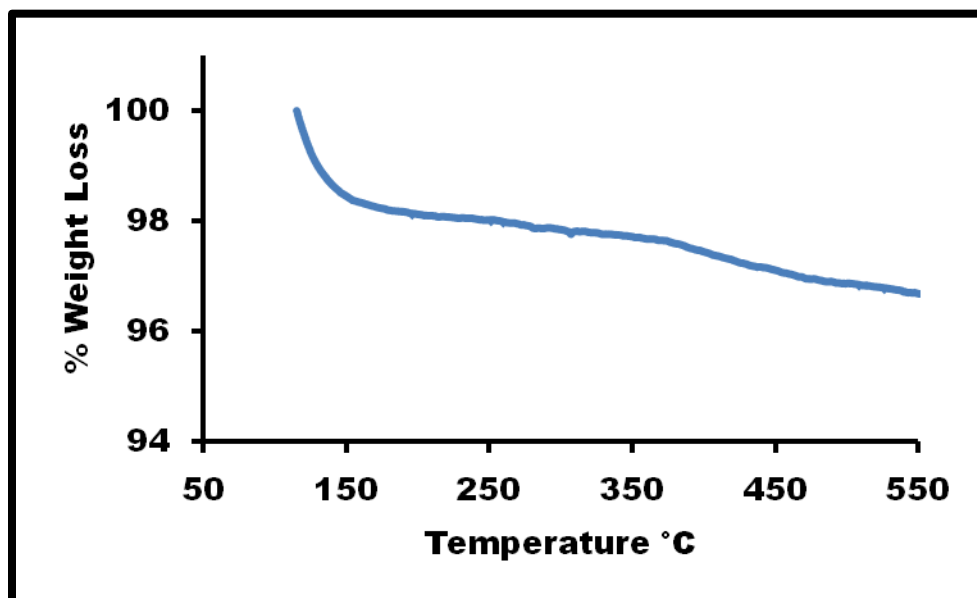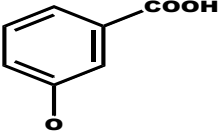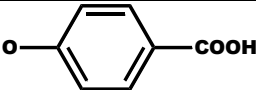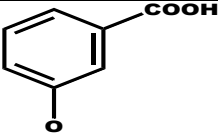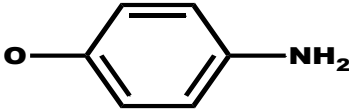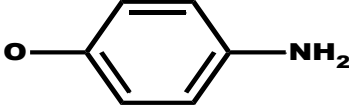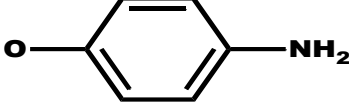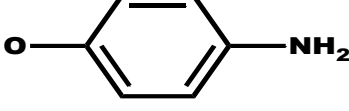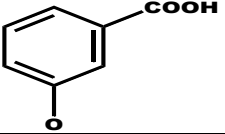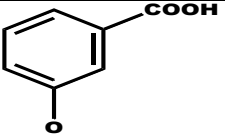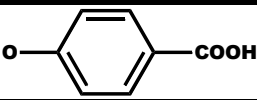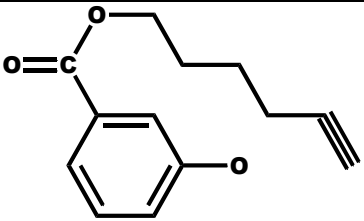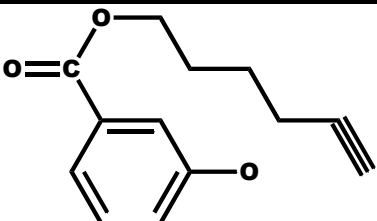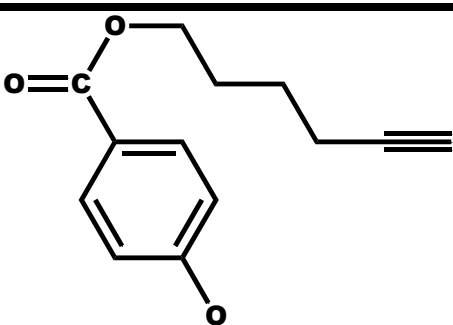
Fig 3.4 shows the TGA measurements for SiNPs alone.

3.2.   Syntheses and Characterization of MPcs

As stated previously only complexes **10**, **13**, **19-21** are new and hence discussed in detail. Listed in Table 3.2 are the MPcs and the conjugates employed in this work.

Table 3.2: List of MPcs and conjugates employed in this work.

R =	Position	Complex number	Conjugates with SiNPs
(benzene ring with COOH and O substituents)	α (Tetra)	(8)	**8-SiNPs** (linked amide), **8-SiNPs** (linked ester), **8-SiNPs** (doped) and **8-SiNPs** (mixed)
(benzene ring with O and COOH substituents)	α (Tetra)	(9)	**9-SiNPs** (linked amide), **9-SiNPs** (linked ester), **9-SiNPs** (doped) and **9-SiNPs** (mixed)
(benzene ring with COOH and O substituents)	β (Tetra)	(10)	**10-SiNPs** (linked amide), **10-SiNPs** (doped) and **10-SiNPs** (mixed)
(benzene ring with O and NH₂ substituents)	α (Tetra)	(11)	**11-SiNPs** (linked amide) and **11-SiNPs** (mixed)
(benzene ring with O and NH₂ substituents)	β (Tetra)	(12)	**12-SiNPs** (linked amide) and **12-SiNPs** (mixed)
(benzene ring with O and NH₂ substituents)	α (Mono)	(13)	**13-SiNPs** (linked amide) and **13-SiNPs** (mixed)
(benzene ring with O and NH₂ substituents)	β (Mono)	(14)	**14-SiNPs** (linked amide) and **14-SiNPs** (mixed)

R =	Position	Complex number	Conjugates with SiNPs
NH₂	β (Mono)	(15)	15-SiNPs (linked amide) and 15-SiNPs (mixed)
	α (Mono)	(16)	-
	β (Mono)	(17)	-
	α (Mono)	(18)	-
	α (Mono)	(19)	19-SiNPs (linked click) and 19-SiNPs (mixed)
	β (Mono)	(20)	20-SiNPs (linked click) and 20-SiNPs (mixed)
	α (Mono)	(21)	21-SiNPs (linked click) and 21-SiNPs (mixed)

The UV/vis absorption spectra of compounds **8** and **11** (as examples for the previously synthesized compounds) with Q-band maxima at 692 nm and 701 nm for complexes **8** and **11** respectively are displayed in Fig. 3.5. The Q band maximum for all the synthesized compounds is shown in Table 3.3 [**149, 157-161**]. The Q band of complex **11**

67

is red shifted compared to **12** due to α substitution in the former. Similar red shifts in Q band were also observed in complexes **16** and **18** compared to **17** alone, the same applies to **13** and **14**. Complexes **8** and **9** have ~ the same Q band showing that the effect of the point of substitution on the phenoxy ring is negligible. Complexes **14** and **15** have ~ the same Q band hence the presence of the spacer makes no difference.
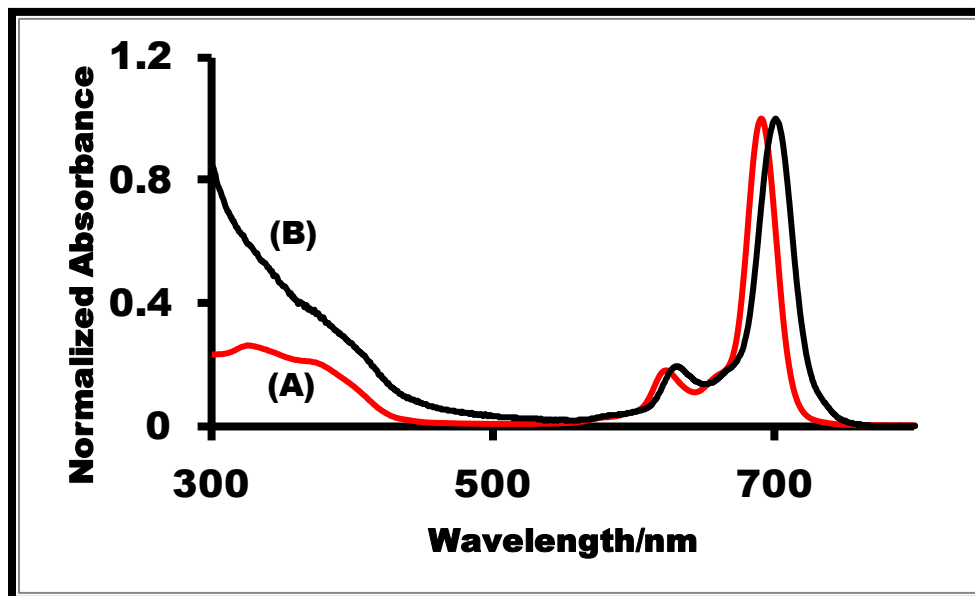
Fig 3.5 Electronic absorption spectra of compounds 8 (α-ZnT-3-CPPc) **(A)** and **11** (α-ZnTAPPc) **(B)**.

Table 3.3: Q band maximum for the previously synthesized complexes in DMSO.

Compound	Q-band maximum (nm)	Reference (s)
8 (α-ZnT-3-CPPc)	692	[149]
9 (α-ZnT-4-CPPc)	691	[149, 158]
10 (β-ZnT-3-CPPc)	679	-
11 (α-ZnTAPPc)	701	[157]
12 (β-ZnTAPPc)	685	[159]
13 (α-ZnMAPPc)	681	-
14 (β-ZnMAPPc)	676	[160]
15 (β-ZnMAPc)	678	[161]
16 (α-ZnM-3-CPPc)	677	[149]
17 (β –ZnM-3-CPPc)	674	[149]
18 (α-ZnM-4-CPPc)	677	[149]
19 (α-ZnM-3-CAPc)	677	-
20 (β –ZnM-3-CAPc)	674	-
21 (α-ZnM-4-CAPc)	677	-

3.2.1. Synthesis and Characterization of 2(3), 9(10), 16(17), 23(24)-tetrakis-(3-carboxyphenoxy)phthalocyaninato zinc (II) - β-ZnT-3-CPPc (10) – Scheme 3.3

Scheme 3.3 shows the route used in the synthesis of complex **10,** the complex was obtained from cyclotetramerization of the substituted phthalonitrile (**5a**).

The compound was characterized by UV/vis, IR, ^{1}H NMR, elemental analysis and MALDI-TOF mass spectroscopy, all of which showed agreement with the expected results. Complex **10** showed a molecular ion peak corresponding to a protonated specie

[M+H]+ at 1123 amu which is consistent with the calculated value at 1122 amu. ^{1}H NMR data was consistent with structure for complex **10.** All the protons were observed in their respective regions. The phthalocyanine ring protons integrated for 12, the phenyl protons for 16 and the carboxylic protons for 4 as expected.

The UV/vis spectrum of compound **10** in DMSO is displayed in Fig. 3.6. The spectrum exhibited a monomeric Q band maximum with excellent solubility in DMSO, with a Q band at 679 nm, Table 3.3. The Q band maximum is blue shifted compared to those of known complexes **8** and **9** (also containing carboxyphenoxy), due to β substitution on the Pc ring of complex **10**.
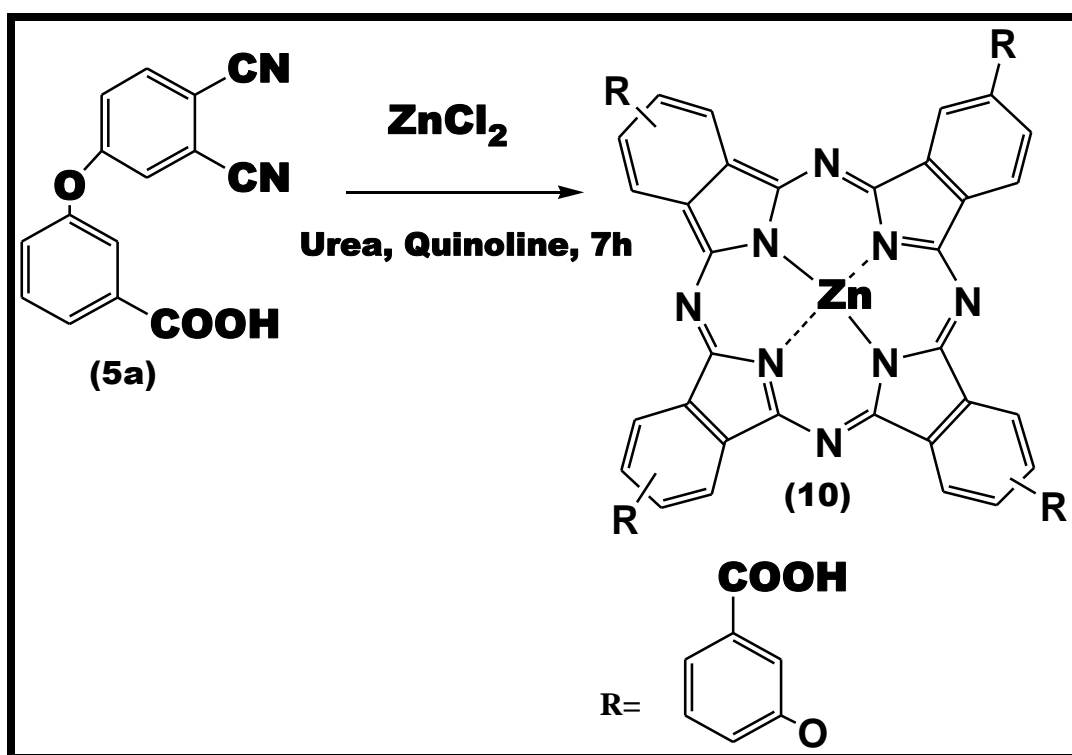
Scheme 3.3: Synthetic route for the formation of β-ZnT-3-CPPc (10)
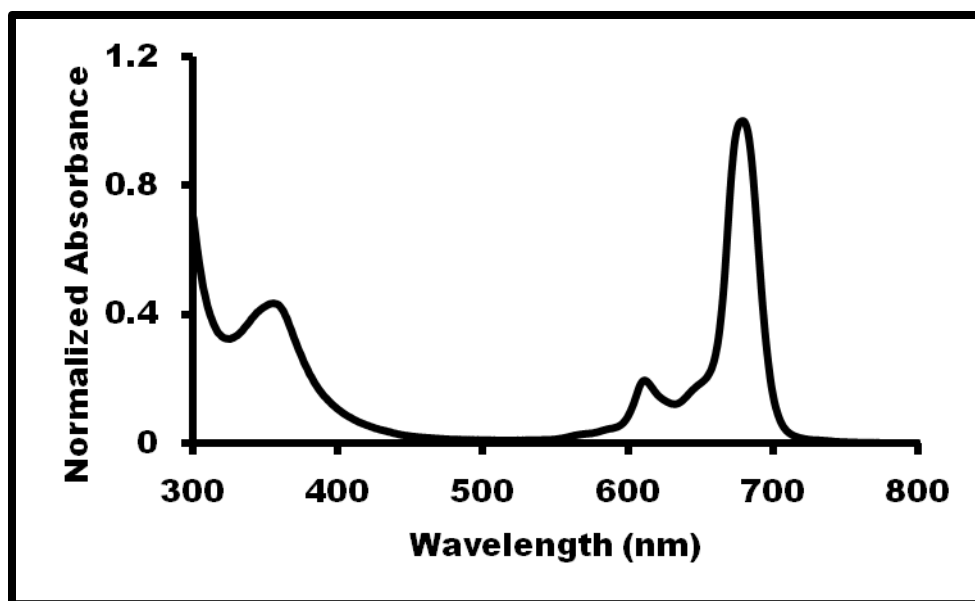
Fig 3.6 Electronic absorption spectrum of compound 10 (β-ZnT-3-CPPc) in DMSO.

3.2.2. 1(4), -Mono-(4-aminophenoxy)phthalocyaninato zinc (II) - α-ZnMAPPc (13) - Scheme 3.4

The synthesis of **α-ZnMAPPc** (**13**), is reported here for the first time, Scheme 3.4 and was characterized by 1H-NMR, mass and IR spectroscopy, as well as elemental analysis. Complex **13** showed a molecular ion peak corresponding to protonated specie $[M+2H]^+$ at 686 amu which is consistent with the calculated value at 684 amu.

Infrared spectroscopic analysis of **α-ZnMAPPc** (**13**), showed a broad peak around 3200 cm^{-1} which is characteristic of the N-H stretch of a primary amine [**170**]. This was supported by a corresponding N-H bending mode at 1602 cm^{-1}. The peak at 1086 cm^{-1} is attributed to C-O-C bond while the C-N vibrations due to the phthalocyanine ring were observed at 1472, 1363 and 1314 cm^{-1}. All the protons were observed in their respective regions. The phthalocyanine ring protons integrated for 15 (12 protons for the un-substituted benzene ring and 3 for the substituted ring), the phenyl protons for 4 and the amine protons for 2 as expected.

The UV/vis spectrum of compound **13** in DMSO is displayed in Fig. 3.7. The spectrum exhibited a monomeric Q band maximum at 681 nm in DMSO, Table 3.3. The charge transfer band of the complex could be seen between 400-500 nm. The Q band is red shifted compared to the corresponding complex **14** due to α substitution in **13**.
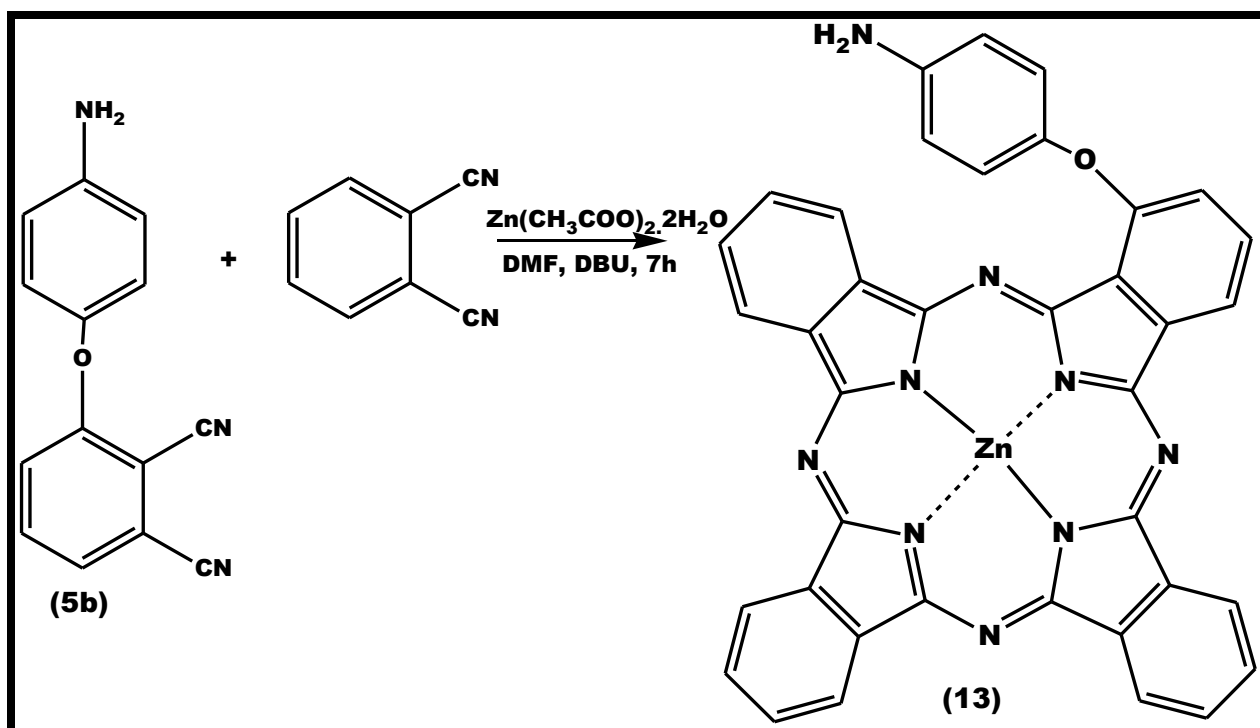
Scheme 3.4: Synthetic route for the formation of 13 (α-ZnMAPPc)
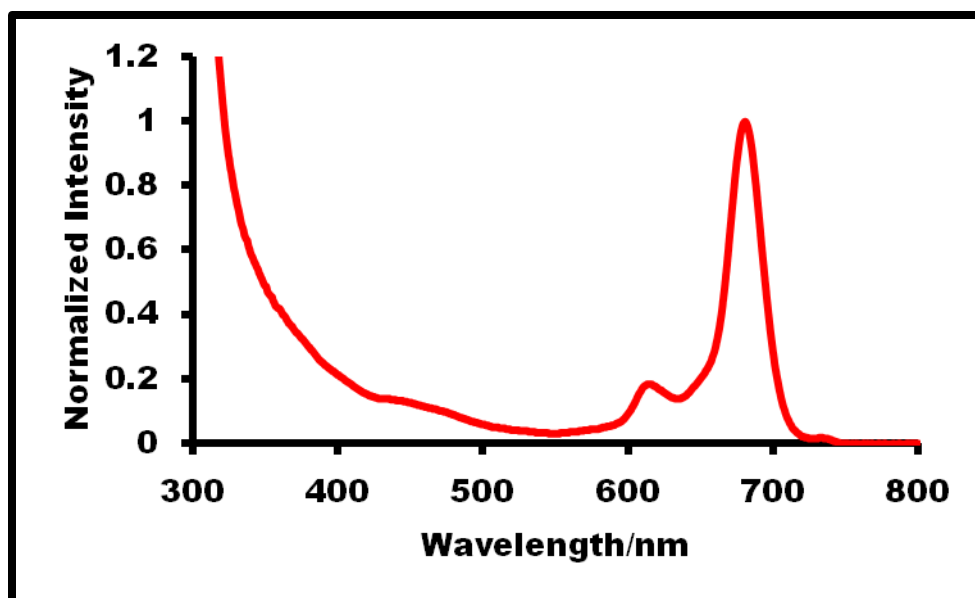
Fig 3.7 Electronic absorption spectrum of compound 13 (α-ZnMAPPc) in DMSO.

3.2.3. Syntheses and Characterization of complexes 19 (α-ZnM-3-CAPc), 20 (β -ZnM-3-CAPc) and 21(α -ZnM-4-CAPc) - Schemes 3.5a, 3.5b and 3.5b

Schemes 3.5 show the routes used in the syntheses of complexes **19**, **20** and **21.**

Complexes **19**, **20** and **21** were synthesized from complexes **16**, **17** and **18 [149]** respectively via the formation of an ester bond between the carboxylic acid of the MPcs and the hydroxyl group on the 5-hexyn-1-ol. The cleavage of the carboxylic acid group was facilitated using DCC and DMAP.

Complexes **19**, **20** and **21** showed molecular ion peaks corresponding to protonated species at 796 amu [M+2H]+, 796 amu [M+2H]+ and 797 amu [M+3H]+ for complexes **19**, **20** and **21** respectively. The molecular ion peaks are consistent with the calculated value at 794 amu. Following the formation of **19**, **20**, and **21**, the following IR peaks were observed : the C-O ether stretch at ranging from 1228 to 1243 cm^{-1}, the carbonyl ester peak ranging from 1713 to 1726 cm^{-1}, the C≡C peak ranging from 2160 to 2161 cm^{-1},

methylene C-H stretch of the hexyne chain at ~2850 and 2926 cm^{-1} and the C-H stretch of the alkyne group at ~3320 cm^{-1}, confirming the conjugation of the 5-hexyn-1-ol [170].

The ^{1}H NMR spectra for **19**, **20**, and **21** were in good agreement with the structure of the newly formed compound. The aromatic protons were integrated for 19 protons (phenyl ring and the Pc ring), the methylene protons were integrated for 8 protons while the acetylene proton integrated for 1 as expected.

The UV/vis spectrum of compound **19**, **20**, and **21** in DMSO is displayed in Fig. 3.8. The spectrum exhibited a monomeric Q band maximum in DMSO. Fig. 8B (ii) shows the MCD spectrum of complex **19**, an A term type of spectrum for the Q band is observed. This indicates that the excited state of the complex is degenerate and as such exists in a monomeric form in DMSO [174, 175].

(A)

5-Hexyn-1-ol

DCC, DMAP, DMF
10 days

(16)

(19)

(B)

5-Hexyn-1-ol

DCC, DMAP, DMF
10 days

(17)

(20)
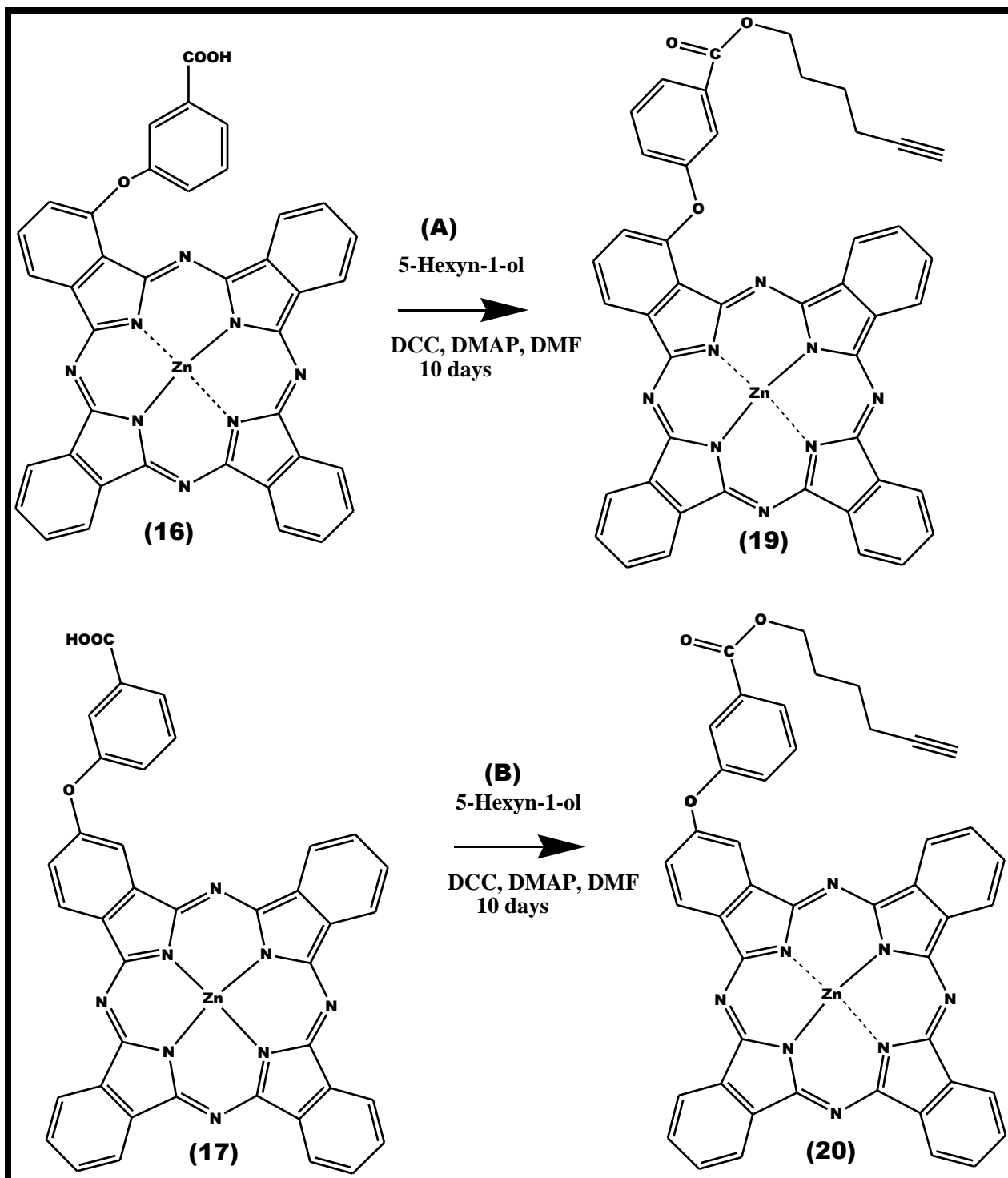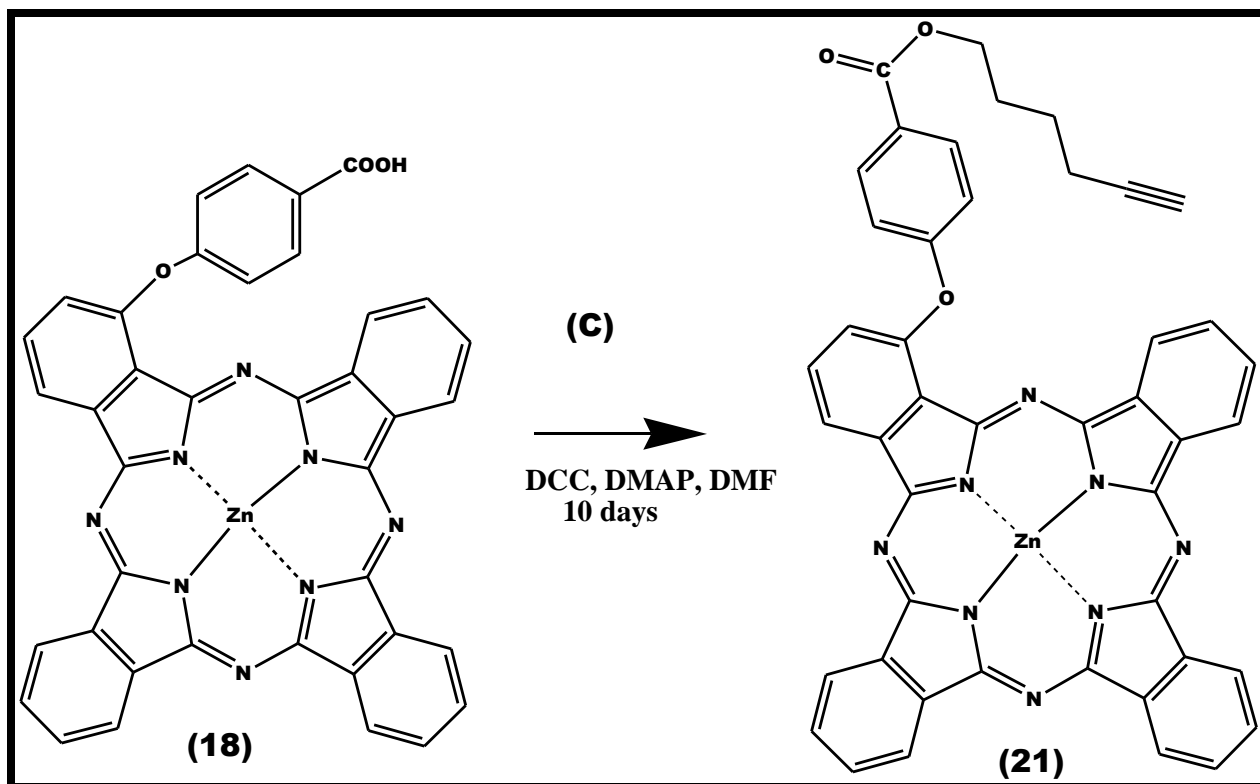
Scheme 3.5: Synthetic route for the formation of (A) α-ZnM-3-CAPc **(19), (B)** β-ZnM-3-CAPc **(20) and (C)** α-ZnM-4-CAPc **(21)**
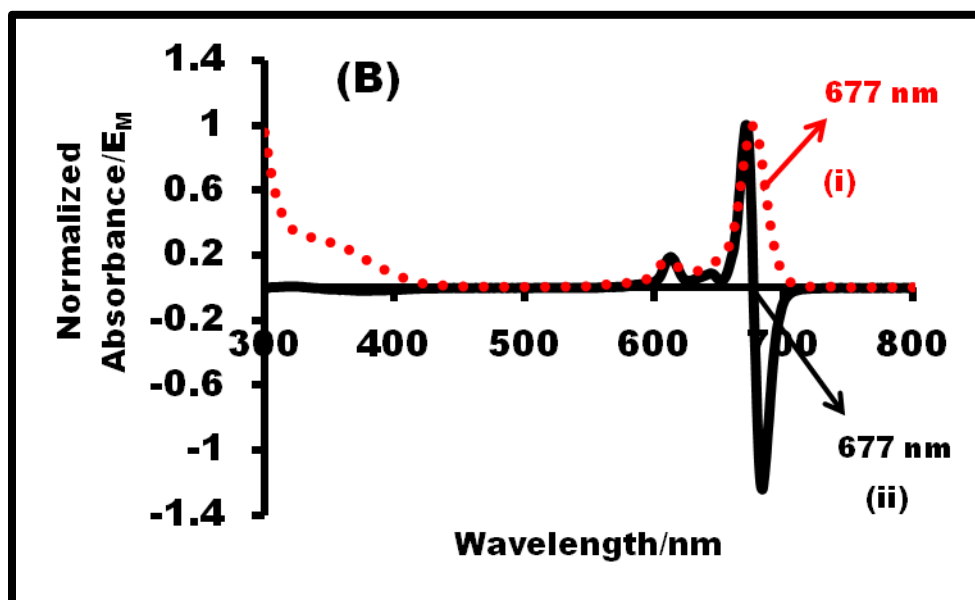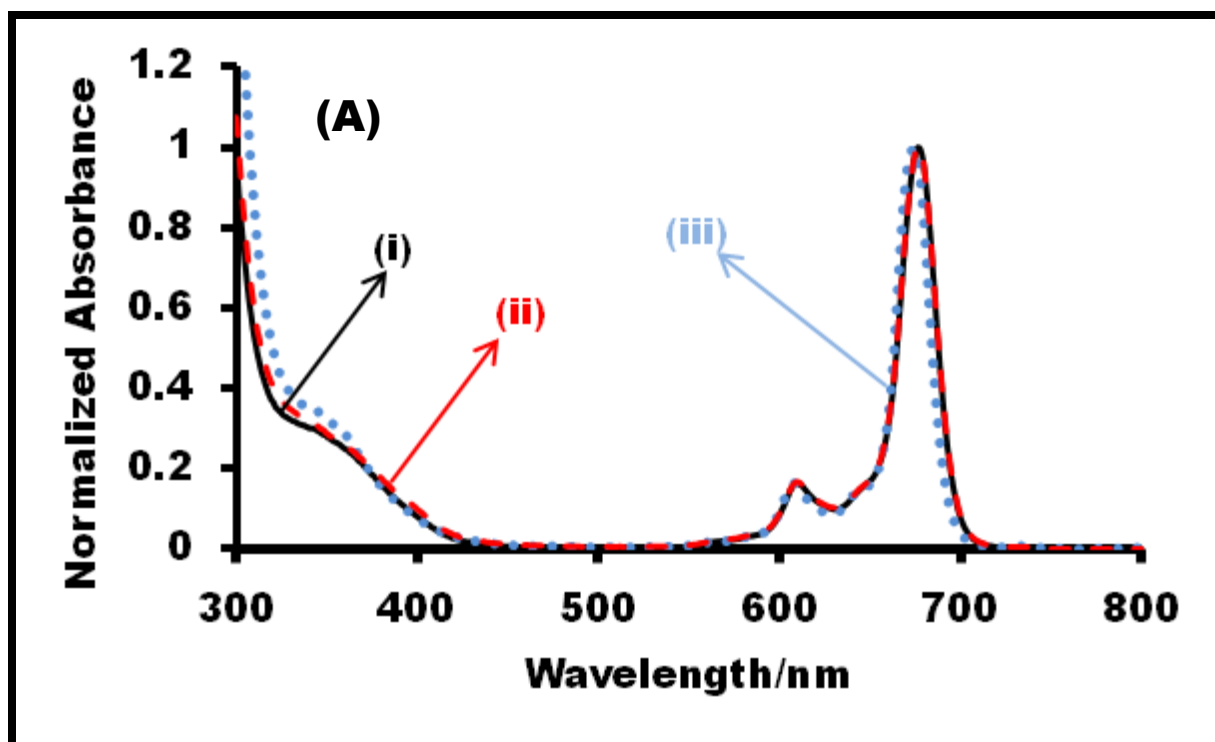
Fig 3.8(A) Electronic absorption spectra of compounds (i) 19 (α-ZnM-3-CAPc), (ii) 20 (β-ZnM-3-CAPc) and **(iii) 21 (α-ZnM-4-CAPc) in DMSO. Fig 3.8(B) Absorption spectrum of 19 (i) and magnetic circular dichroism spectrum of compound 19 (ii).**

3.3.   MPc-SiNPs conjugates - Schemes 3.6 - 3.10

Table 3.2 shows the Pc-SiNPs employed in this work.

- Complexes **8** and **9** were linked by both amide and ester bond. The complexes were also doped and as result, they were studied in more detail as representatives of the other conjugates.

- Complex **10** was doped within the silica matrix, linked via amide bond and then compared with corresponding complex **8.**

- Complex **11** (α-substituted) was linked via amide bond and compared with corresponding amide linked complex **12** (β-substituted)

- Complex **13** (α-substituted) was linked via amide bond and compared with corresponding amide linked complex **14** (β-substituted). Amide linked **14** was also compared to amide linked **15** (β-substituted) to see the effect of the spacer.

- Amide linked complex **11** (Tetra-substituted) was also compared to **13** (Mono substituted)

- Amide linked complex **12** (Tetra-substituted) was also compared to **14** (Mono substituted)

- Complexes **16**, **17** and **18** were not linked to SiNPs but were only used as precursors for complexes **19**, **20** and **21**

- Complexes **19**, **20** and **21** were linked to SiNPs via click chemistry and compared to each other

Amino functionalized SiNPs (SiNPs-NH$_2$) were conjugated to carboxylic acid-containing Pc (**8-10**) by the activation of the COOH groups of the Pcs using DCC and DMAP as coupling agents, Scheme 3.6. The COOH groups on the SiNPs-COOH were also activated and covalently bonded to the amino group (s) of compounds **11**, **12**, **13**, **14** and **15**, Scheme 3.7. As a result, an amide bond between the SiNPs and the Pc complexes was formed as represented in Schemes 3.6 (using **9** as a representative of **8** and **10**) and 3.7 (using **11** as a representative of **12-15**). The conjugates formed are represented as **8-SiNPs** (linked amide), **9-SiNPs** (linked amide), **10-SiNPs** (linked

amide), **11-SiNPs** (linked amide), **12-SiNPs** (linked amide), **13-SiNPs** (linked amide), **14-SiNPs** (linked amide) and **15-SiNPs** (linked amide), Table 3.2.
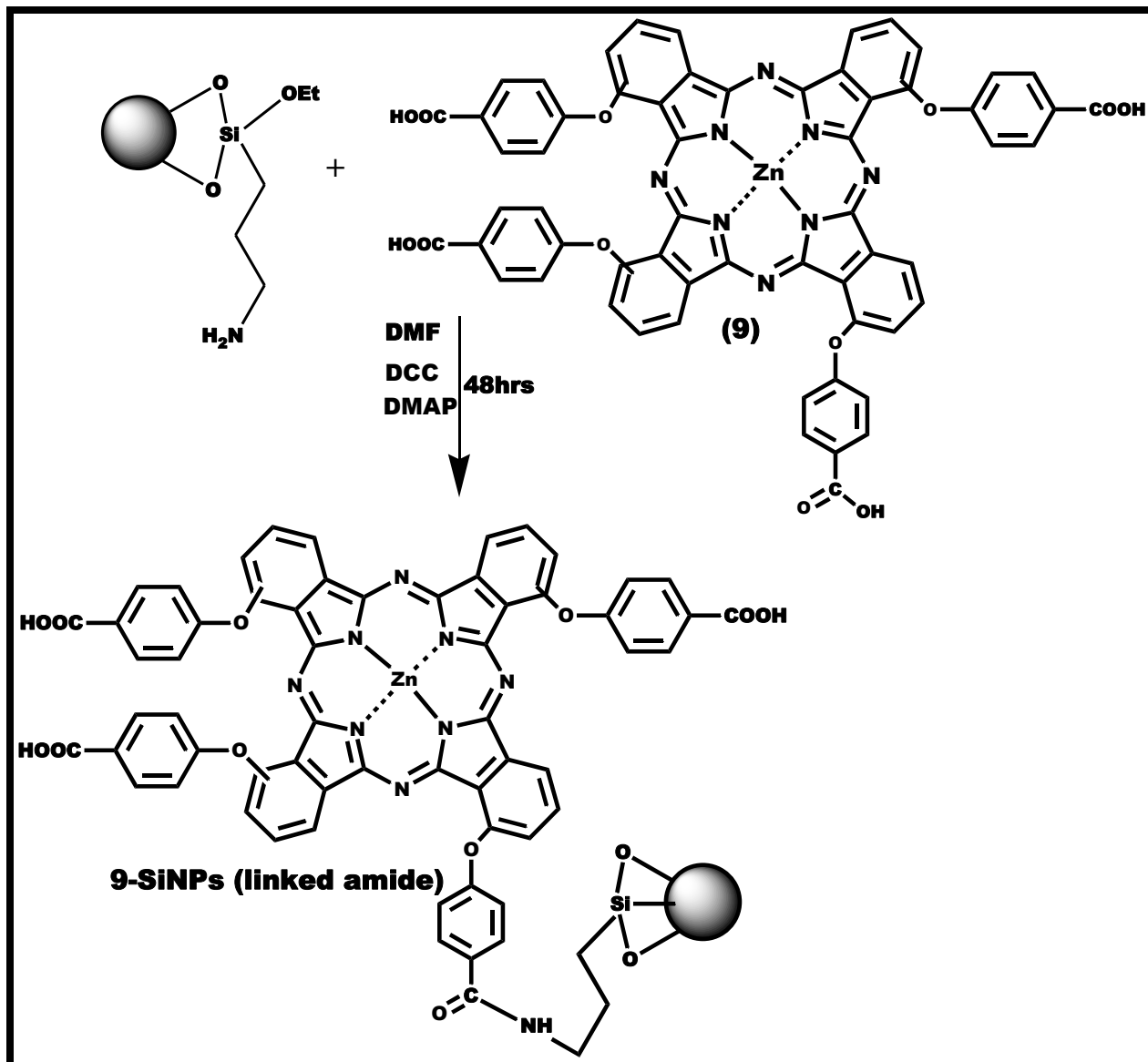
Scheme 3.6: Schematic representation showing the preparation of MPc-SiNPs (linked amide) nanoconjugates (between SiNPs-NH₂ and carboxylic containing Pc complex).
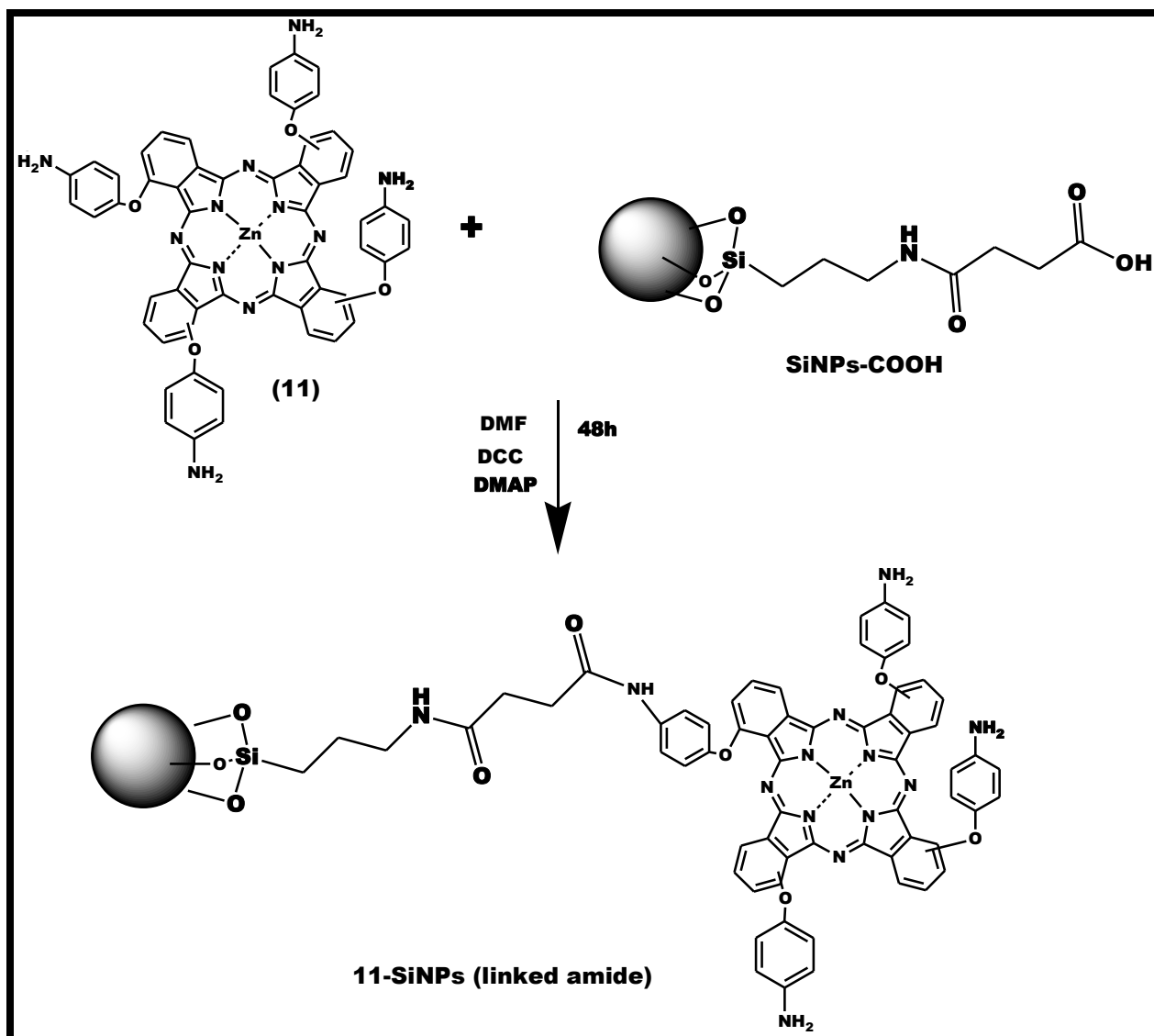
Scheme 3.7: Schematic representation showing the preparation of MPc-SiNPs (linked amide) nanoconjugates (between SiNPs-COOH and amino containing Pc complex).

Uncapped SiNPs (SiNPs) were also conjugated to carboxylic acid-containing Pc (**8** and **9**) by the activation of the COOH groups of the Pcs using DCC and DMAP as coupling agents. The ester bond between the SiNPs and the Pc complexes is represented in Scheme 3.8 (**9** used as an example). The conjugates formed are represented as **8-SiNPs** (linked ester) and **9-SiNPs** (linked ester).
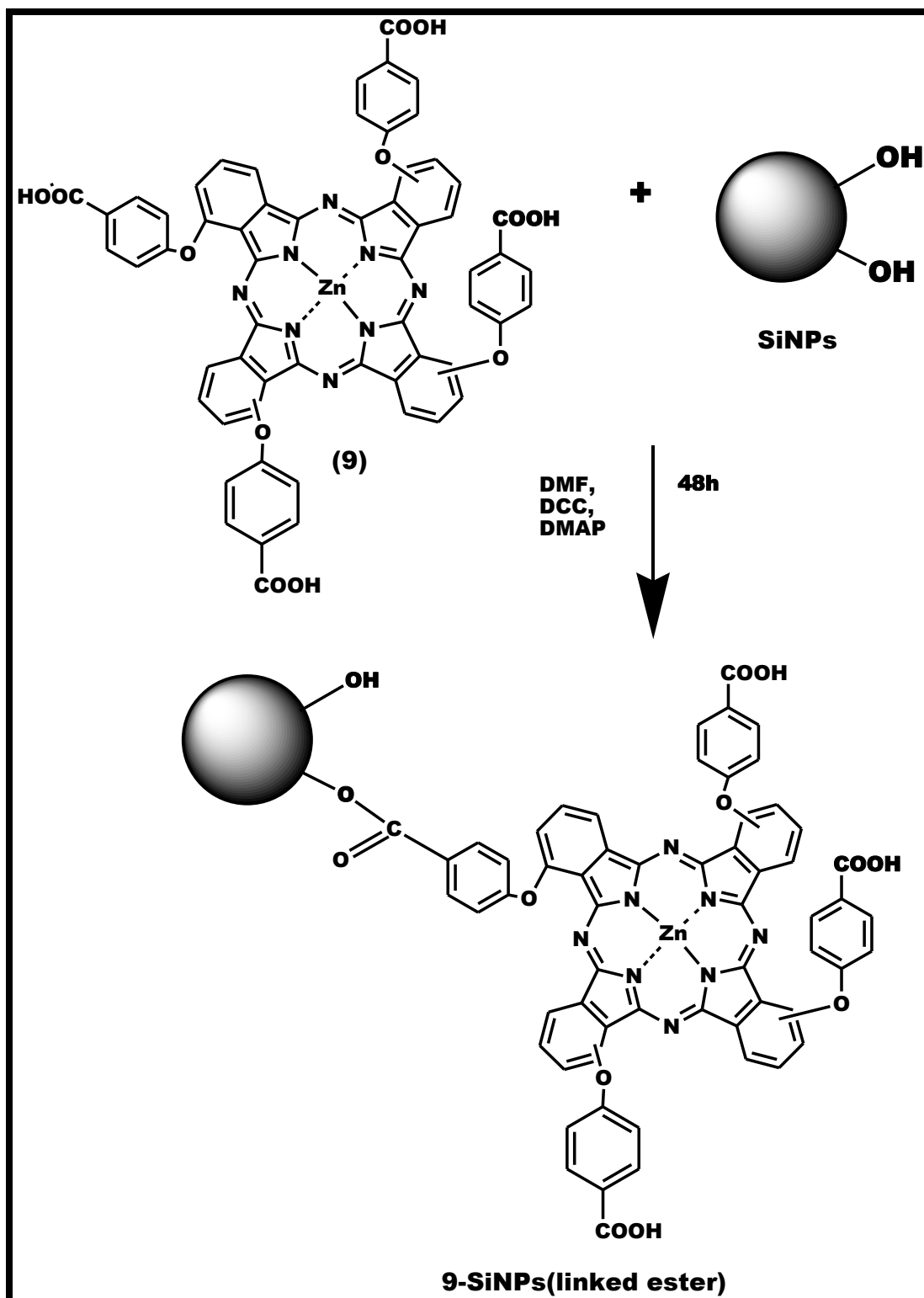
Scheme 3.8: Schematic representation showing the preparation of MPc-SiNPs (linked ester) nanoconjugates

Azide functionalized SiNPs (SiNPs-N$_3$) were also conjugated to Pcs containing alkyne terminal group (**19, 20** and **21**) via click chemistry. The cyclo-addition reaction between the SiNPs-N$_3$ and the Pc complexes is represented in Scheme 3.9 (**21** used as an example). The conjugates formed are represented as **19-SiNPs** (linked click), **20-SiNPs** (linked click) and **21-SiNPs** (linked click), Table 3.2.
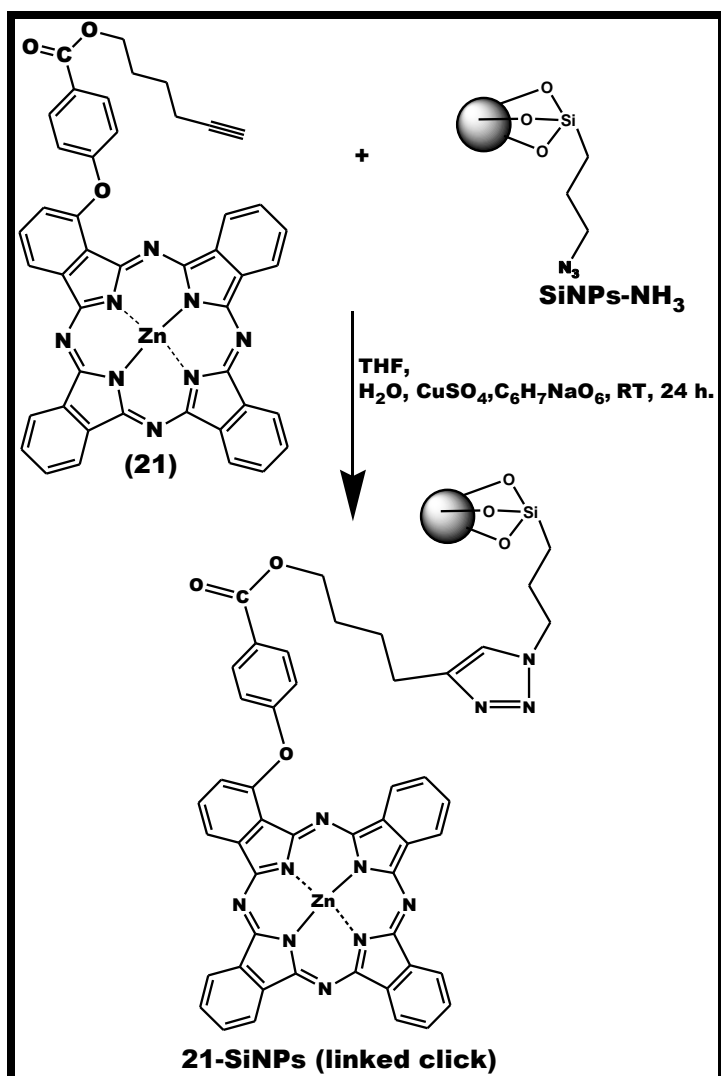
Scheme 3.9: Schematic representation showing the preparation of MPc-SiNPs (linked click) nanoconjugates.

Complexes **8, 9** and **10** were doped within the silica matrix via the microemulsion protocol [**167**]. The synthetic route for the doped Pcs is represented in Scheme 3.10 (**10** used as an example). The conjugates formed are represented as **8-SiNPs** (doped), **9-SiNPs** (doped) and **10-SiNPs** (doped).
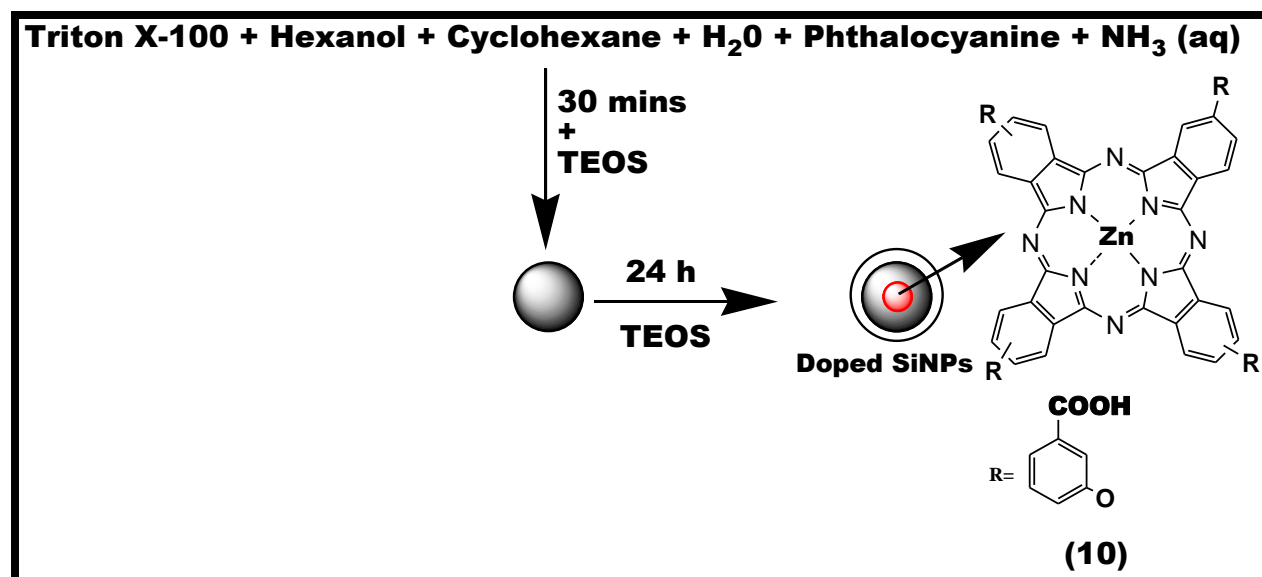
Scheme 3.10: Schematic representation showing the preparation of MPcs doped in SiNPs.

3.3.1. TEM Analysis

The representative TEM images of the conjugates are shown in Fig. 3.9A – 3.9B (using **11-SiNPs** (linked amide), **9-SiNPs** (linked ester), **20-SiNPs** (linked click) and **9-SiNPs** (doped) as examples). The images showed evidence of aggregation following evaporation from solution for the TEM studies though the ester conjugate (**9-SiNPs** (linked ester)), Fig 9A (ii) showed some level of dispersity when compared to the other TEM images.

Phthalocyanines tend to stack by π-π interactions especially in the solid state, hence the observed aggregation on the TEM images. Also, the clustering seen in the conjugates could arise from the manner in which the phthalocyanines assemble on the SiNPs leading to interaction between adjacent Pc molecules. Similar aggregation behavior has been observed in corroles grafted to silica nanoparticles **[176].** The TEM image also indicated that the dyes were encapsulated within the silica matrix, Fig. 3.9A (iv), as

judged by the white spots at the centre of the nanoparticles. The TEM images (Figs. 3.9A (i), 3.9A (ii) and 3.9A (iii)) of the SiNPs covalently attached to the Pc do not show the spots at the centre, though the surface grafted and the doped SiNPs visually had a green/blue color depending on the color of the phthalocyanine complex employed. The size distribution of the nanoparticles is shown in histograms in Fig 3.9B (v-viii)
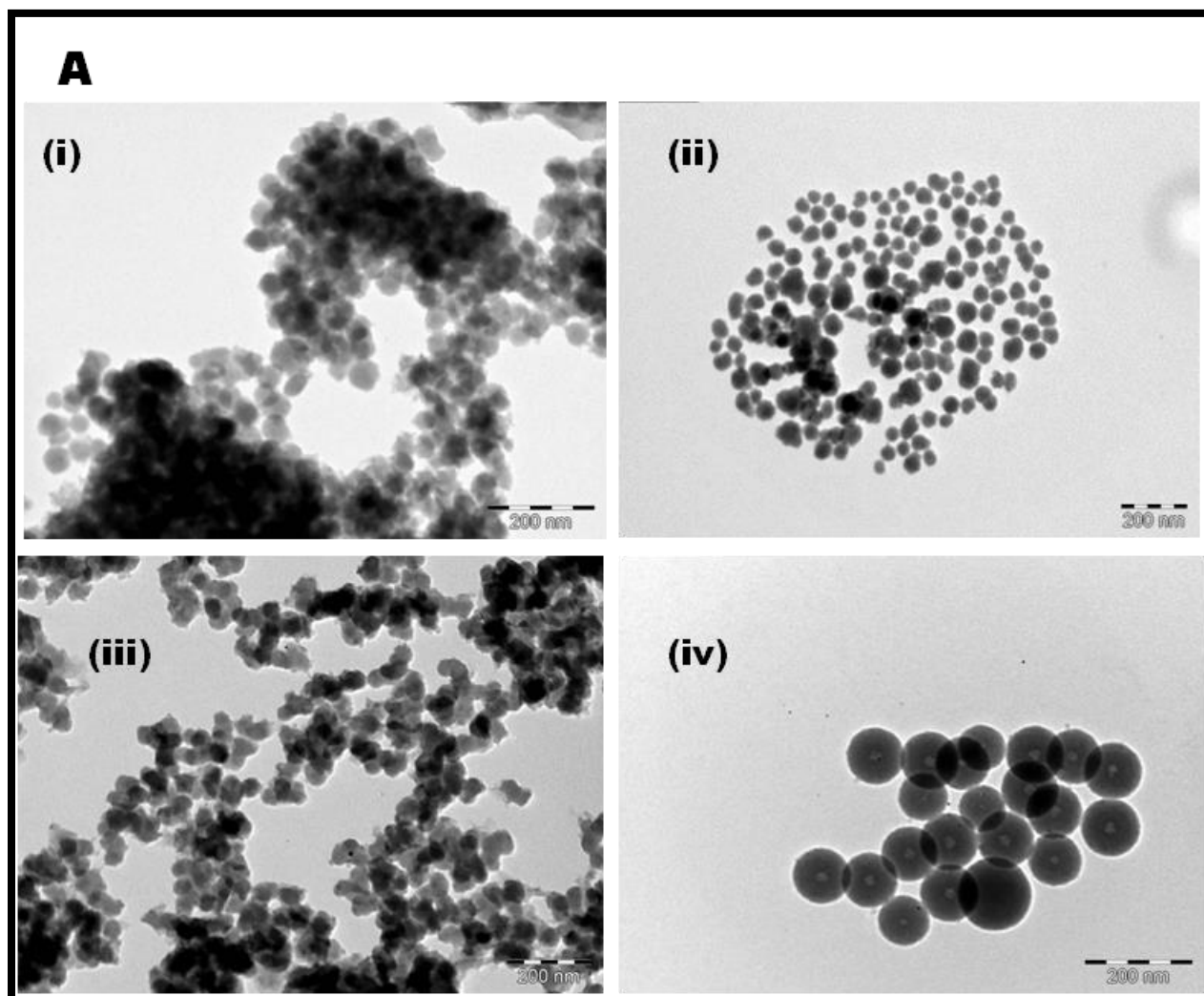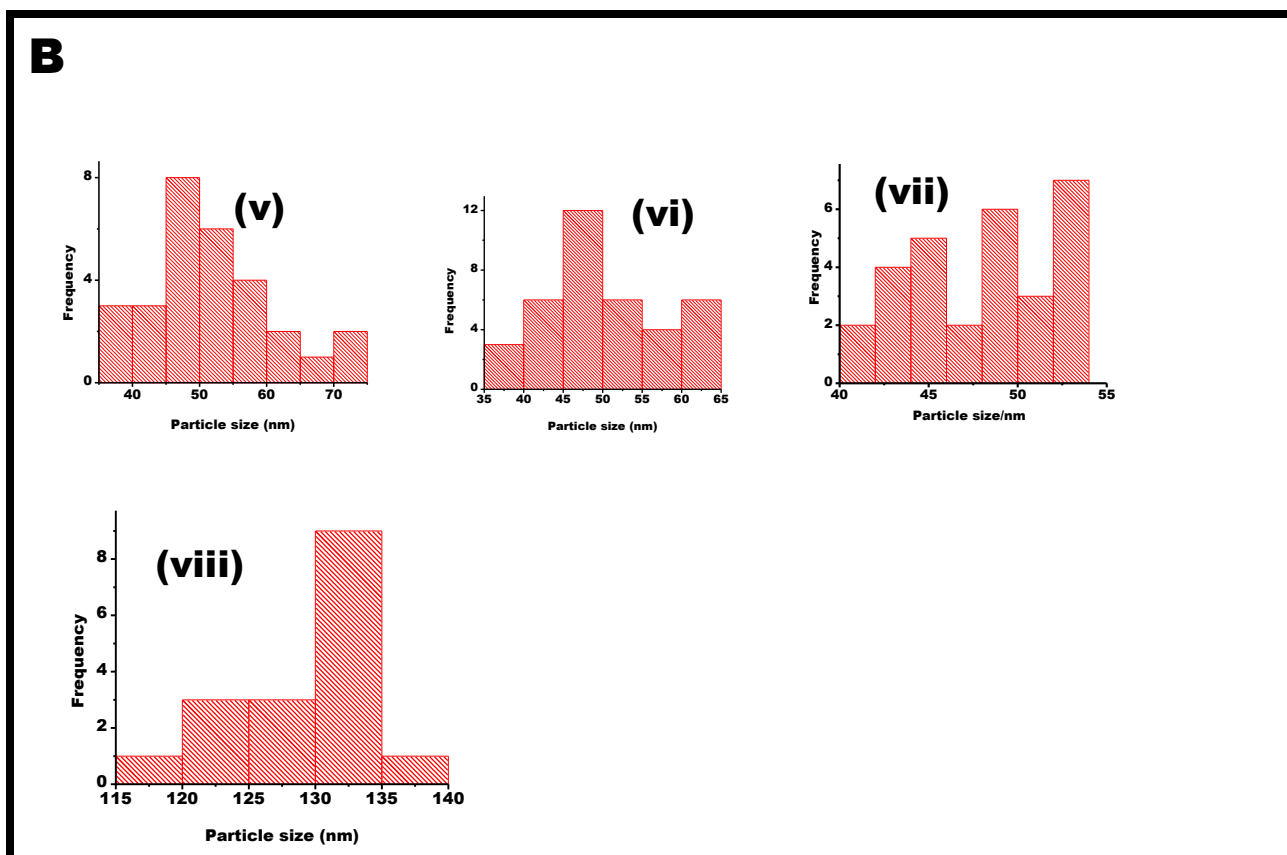
Fig. 3.9A: TEM images for (i) 11-SiNPs (linked amide), (ii) 9-SiNPs (linked ester), (iii) 20-SiNPs (linked click) and (iv) 9-SiNPs (doped). (B) v-viii shows the corresponding histograms.

The sizes of the nanoconjugates formed in this work were generally less than 90 nm and were larger than the starting silica nanoparticles. The increase in size could be attributed to aggregation upon conjugation. The large size of the doped nanoparticles, Fig 3.9B (viii) is as a result of the additional TEOS added during the synthesis to provide additional protection to the core and Pc [**16, 177**].

3.3.2. Loading Capacity of MPcs onto the SiNPs

The mass loading of the phthalocyanine complexes the SiNPs were determined using UV-Vis of the Pcs using reported methods [**178, 179**]. As examples, the mass loading of complexes **11** and **12** onto the SiNPs were found to be 88.0 µg per mg of SiNPs for **11-SiNPs** (linked amide) and 99.3 µg per mg of SiNPs for **12-SiNPs** (linked amide). This indicates a larger loading capacity for the peripherally substituted conjugate, **12-SiNPs** (linked amide). It is possible that at the peripheral position, there is less steric hindrance towards binding to the SiNPs; hence, more Pcs are linked to the SiNPs at the peripheral position. The grafting of more than one Pc to the surface of the SiNPs, Fig 3.10(A**)**, is possible due to the presence of extra COOH groups on the SiNPs. However, the binding of more than one SiNPs to Pc, Fig. 3.10(B) is less likely due to the small size of the Pc (~ 1 nm) in comparison to the SiNPs (> 20 nm), such binding would result in an unstable structure. It is also possible that the Pc molecules can act as a link between two SiNPs, Fig. 3.10 (C) forming a chain, though the resulting molecule could also result in the straining of the Pc molecule. The situation depicted in Fig. 3.10 (C) may also result in interactions which are observed as agglomeration in the TEM image.
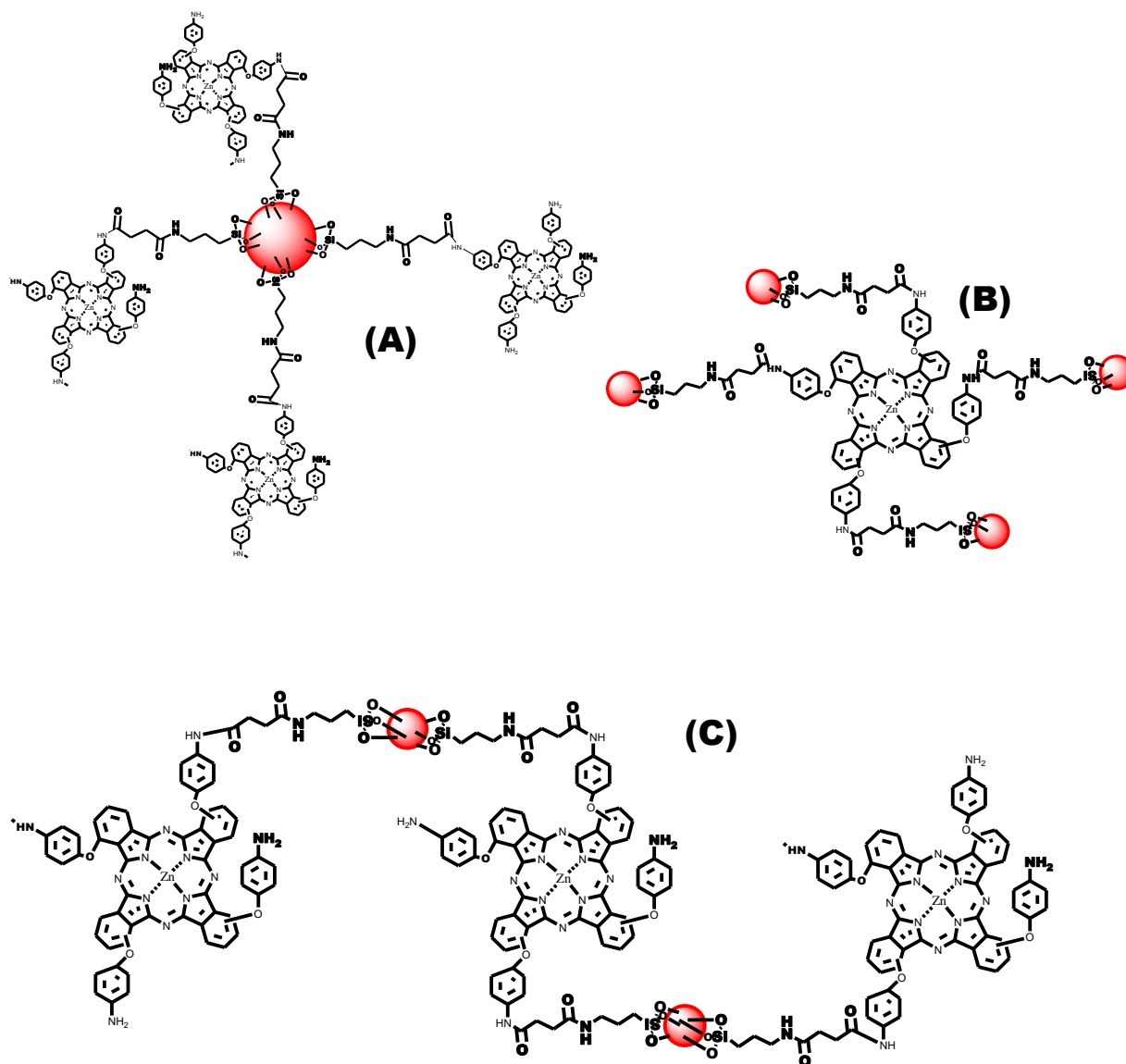
Fig. 3.10: Representation of (a) more than one Pc linked to SiNPs, (b) more than one SiNPs linked to one Pc and (c) a Pc linking two SiNPs (using 11-SiNPs linked amide as an example).

3.3.3. FT-IR Analysis

To confirm the conjugation between the SiNPs and MPc complexes via covalent bond formation (amide bond, ester bond and click chemistry), FT-IR analysis was carried out. As an example, Fig. 3.11 shows the FT-IR spectra of (A) **9,** (B) SiNPs, (C) SiNPs-NH$_2$, (D) **9-SiNPs** (linked ester) and **9-SiNPs** (linked amide) respectively. For **9,** the peak at ~ 3478 cm^{-1} is attributed to the OH peak (of the carboxylic acid) while the peak at 1653 cm^{-1} may be assigned to the carbonyl of the carboxylic acid. The bands at 3400 cm^{-1}, 1039 cm^{-1} and 794 cm^{-1} for SiNPs may be assigned to the Si-OH, Si- O-Si and Si-O peaks respectively. As discussed above, similar Si-O-Si peak and Si-O bands were observed in the SiNPs-NH$_2$ with the weak amino peak appearing at 1636 cm^{-1}. For **9-SiNPs** (linked ester), the carbonyl peak shifted from ~1653 cm^{-1} for the Pc alone to 1657 cm^{-1} for the conjugate, suggesting interaction between SiNPs and complex **9**. Also, the appearance of a new peak at 1389 cm^{-1}, representing the CH bending of the aromatic ring indicates that grafting of the Pc onto the SiNPs has occurred. For **9-SiNPs** (linked amide), the appearance of the broad peak around 3434 cm^{-1} suggests the cleavage of the hydroxyl group of the acid functionality of the phthalocyanine complex (**11**) on covalent amide bond formation with the N–H groups of the APTES coated silica nanoparticles. The appearance and shift of the carbonyl peak at 1660 cm^{-1} on the hybrid particle also indicates that the carbonyl of **9** was involved in an electronic interaction due to amide bond formation.
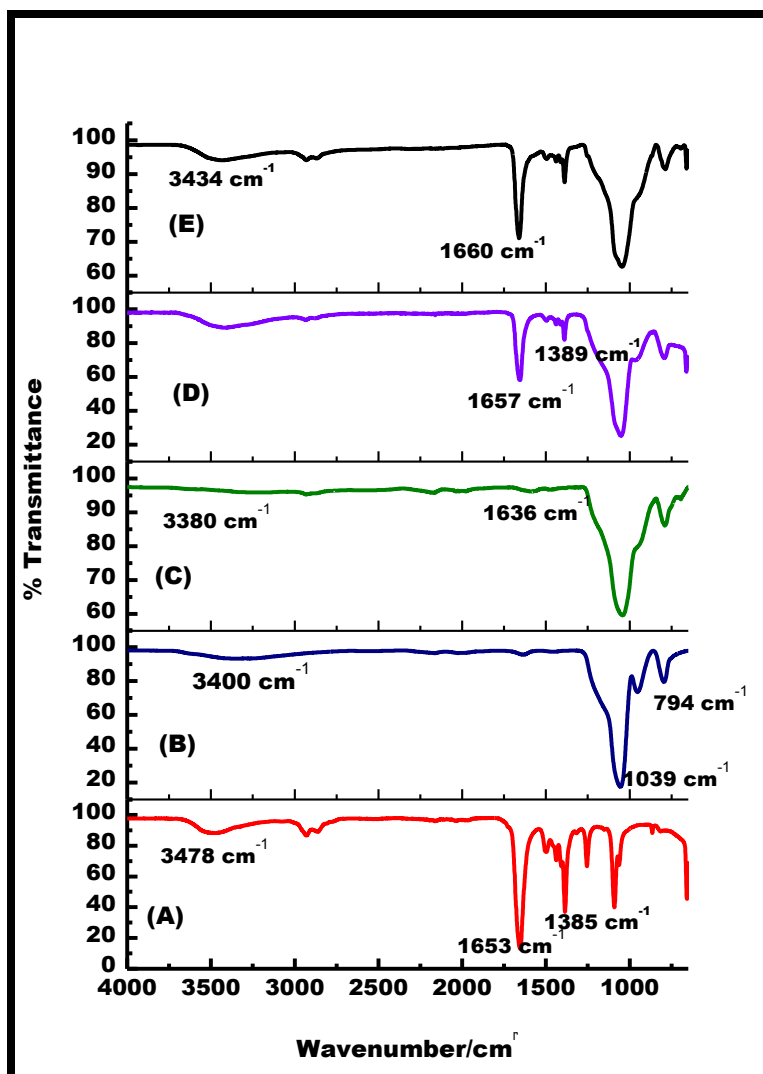
**Fig. 3.11: FT-IR spectra of (A) 9, (B) SiNPs, (C) SiNPs-NH₂, (D) 9-SiNPs (linked ester)
and 9-SiNPs (linked amide).**

3.3.4. Raman spectral characterization

Raman spectroscopy was also utilized in characterizing the hybrid nanoparticles. As an
example, Fig 3.12 shows the Raman spectra of (A) **SiNPs-NH₂** and (B) **9-SiNPs** (linked
amide). Fig. 3.12B shows the Raman spectrum of the conjugate (**9-SiNPs** (linked amide))
with amides bands I to III at 1666, 1513 and 1310 cm^{-1}, respectively (though of low
intensity), confirming the linkage between complex **9** and amino coated silica

nanoparticles (SiNPs-NH$_2$). Amide bands at similar positions have been observed in literature [**180–182**].
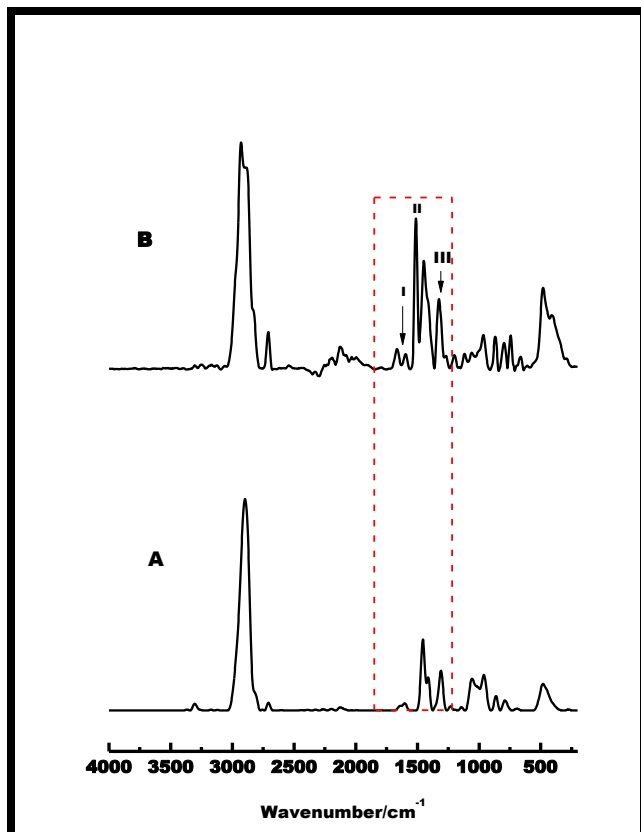
Fig. 3.12: Raman spectra of (A) SiNPs-NH$_2$ and (B) 9-SiNPs (linked amide).

3.3.5. XRD spectral characterization

The nature of the hybrid silica NP was assessed using X-ray diffraction. As an example, Fig 3.13 shows the XRD spectra of (A) SiNPs- COOH, (B) **13–SiNPs** (linked amide), (C) **14–SiNPs** (linked amide) and (D) **15–SiNPs** (linked amide).

Fig. 3.13 (A), representing the COOH functionalized SiNPs, shows a broad peak centred at 2θ = 22.4° (d-spacing at 3.88), while the conjugates show a slight shift in the broad reflection band to 2θ = 23.1° (d-spacing at 3.82), 2θ = 23.1° (d-spacing at 3.91) and 2θ = 23.0° (d-spacing at 3.80) for **13–SiNPs** (linked amide), **14–SiNPs** (linked amide) and **15–**

SiNPs (linked amide), respectively. The small changes observed in the XRD pattern of the conjugates could be due to the parking arrangement of the Pc on the silica matrix. The broad peak confirms the amorphous nature of the SiNPs, which is maintained after functionalization with the phthalocyanine complexes [**57, 167**]. The broad peak for Pc alone was observed near $2\theta = 25.0°$. The peak is typical of amorphous Pcs [**183**].
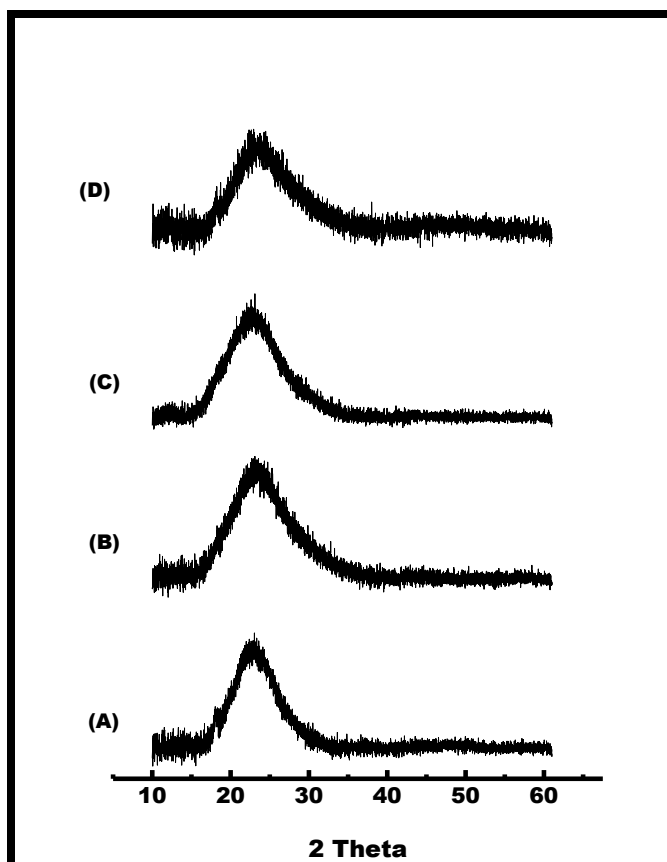
Fig. 3.13: X-Ray diffraction pattern of (A) SiNPs- COOH, (B) 13–SiNPs (linked amide), (C) 14–SiNPs (linked amide) and (D) 15–SiNPs (linked amide).

3.3.6. Thermal Analysis

The thermal stabilities of each of the nanoparticles were studied by TGA. The thermal properties of complex **21** (representative of the complexes), SiNPs-N3, **19-SiNPs** (linked click), **20-SiNPs** (linked click) and **21-SiNPs** (linked click) (representative of the conjugates) are shown in Fig. 3.13. The plot shows the weight variation with

temperature. Fig. 3.14 (B), representing the azide functionalized SiNPs show an initial approximate weight loss of 14.5 % from 30 -250 °C and a further loss of 27.3 % from 300 °C - 800 °C.

The curves obtained for **19-SiNPs** (linked click), **20-SiNPs** (linked click) and **21-SiNPs** (linked click) (Fig. 3.13 (C), (D) and (E)) show very similar patterns with an approximate total % weight loss of 34.1%, 33.6% and 39.0% at 800 °C for **19-SiNPs** (linked click), **20-SiNPs** (linked click) and **21-SiNPs** (linked click) respectively. Of the three conjugates, **21-SiNPs** (linked click) had the highest % weight loss; this could be due to the presence of a different substituent (4-carboxyphenoxy) on the Pc ring when compared to the substituent (3-carboxyphenoxy) on **19-SiNPs** (linked click) and **20-SiNPs** (linked click).

The TGA curve for **21** alone (without SiNPs), (Fig. 3.14A) shows an initial approximate weight loss of 14.7 % below 250 °C and about ~70.5 % weight loss between 350 and 800 °C, due to the decomposition of the Pc molecule. The phthalocyanine complexes show a sharp decrease from 350 °C, which is not observed for the conjugates. The final percentage weight loss is largest for the Pc complexes alone and this is found to decrease upon conjugation. Generally from the TGA analysis, it could be suggested that the SiNPs were found to stabilize the phthalocyanine ring against thermal degradation.
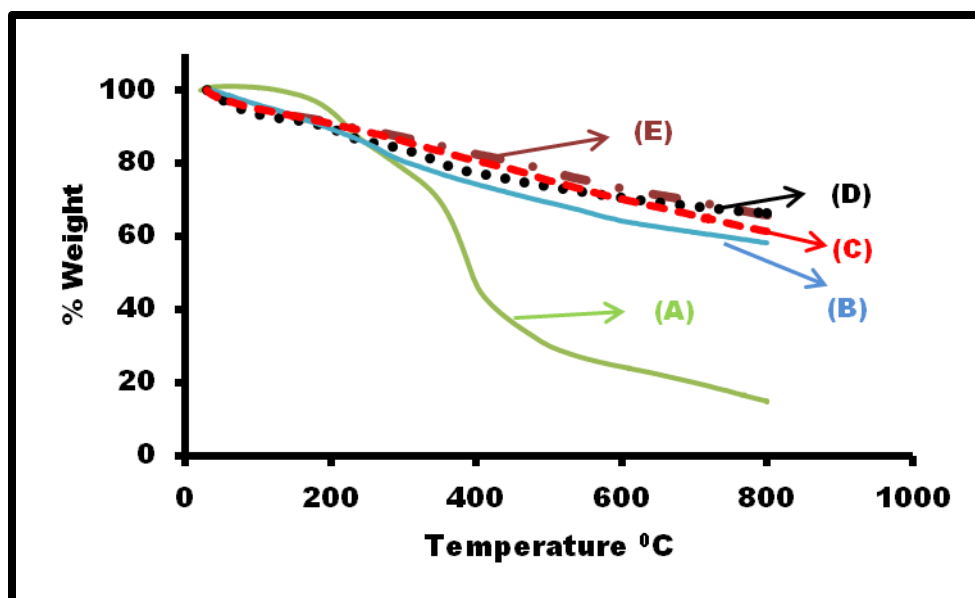
Fig. 3.14: shows TGA measurements of (A) 21 alone, (B) azide functionalized SINPs (SiNPs-N₃) alone, (C) 21-SiNPs (linked click), (D) 19-SiNPs (linked click) and (E) 20-SiNPs (linked click)

3.3.7. Surface Area and Porosity Analyses

The surface area and the porosity of the nanoconjugates were assessed using the BET method. As an example, Fig 3.15 shows the nitrogen adsorption-desorption isotherms for (A) SiNPs-COOH and **13–SiNPs** (linked amide). The BET characterization of the SiNPs-COOH and the conjugate (**13–SiNPs** (linked amide)) show typical type IV sorption isotherms [21, 184]. There was an increase in surface area from 33.93 m²/g for the SiNPs-COOH to 44.16 m²/g for **13–SiNPs** (linked amide). The increase in surface area in the presence of the Pcs could suggest increase in roughness, it has been reported that a rough surface results in larger surface area compared to a smooth surface [185]. A decrease in pore size from 240.49 Å for SiNP-COOH to 192.36 Å for **13-SiNPs** (linked amide) was observed. The results obtained suggest that some of the Pc complexes might have been entrapped in the pore of the functionalized SiNPs, causing a reduction in the pore size. In addition, the decrease in pore size could be due to inter-particle aggregations.
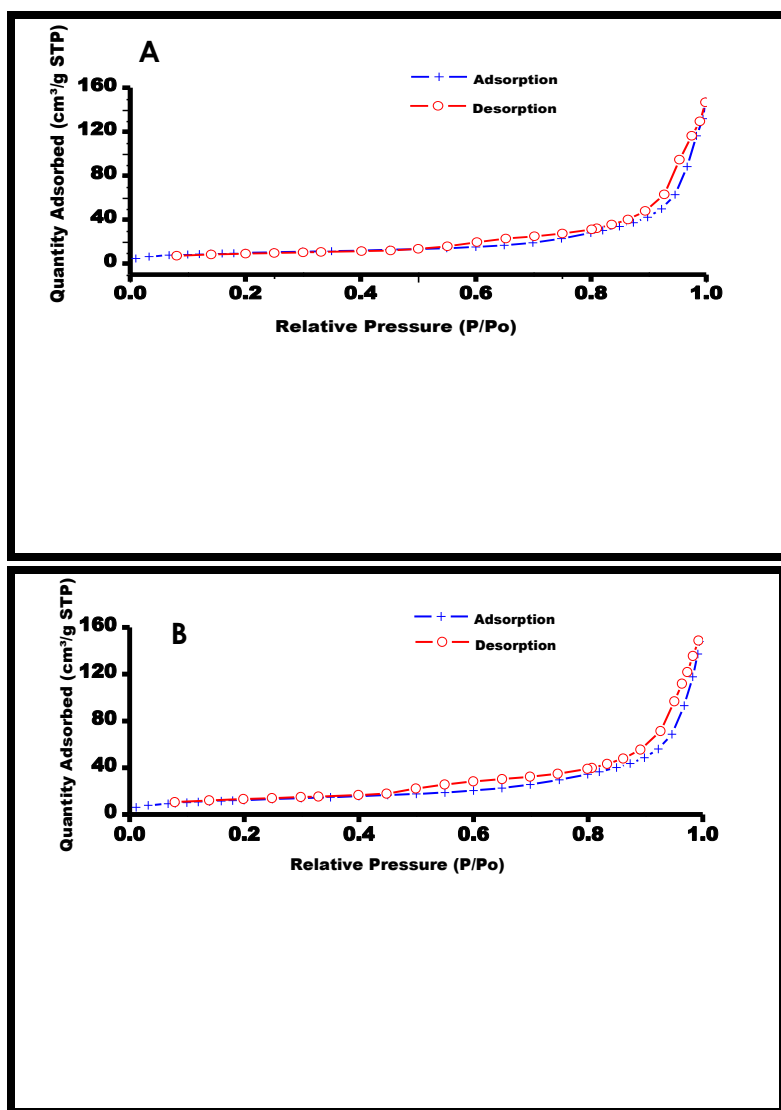
Fig. 3.15: Nitrogen adsorption-desorption isotherms of (A) SiNPs-COOH and (B) 13 –

SiNPs (linked amide).

3.3.8. XPS Analysis

To further confirm that the SiNPs were grafted with phthalocyanines, the chemical composition of the nanoparticles surface was assessed using XPS. As an example, Fig.

3.16 shows the XPS wide scans for (A) SiNPs-NH$_2$ and **8-SiNPs** (linked amide), while Table 3.4 shows the apparent surface composition of the nanoparticles.

The XPS wide scan spectra obtained for both nanoparticles (SiNPs-NH$_2$ and **8-SiNPs** (linked amide)), Fig 3.16, contain signals attributable to Si 2p, Si 2s, C 1s, N 1s and O 1s peaks with binding energies at about 102, 153, 284, 399 and 531 eV, respectively [**162**]. It was observed that the intensity of the N1s peak increased in Fig. 3.16B (at ~399 eV) for **8-SiNPs** (linked amide) (6.32%) compared to SiNPs-NH$_2$ alone (1.88%), Table 3.4, indicating that conjugation took place between the SiNPs-NH$_2$ and the phthalocyanine complex (which contain nitrogen groups in its ring). The increase in intensity of the O1s peak in Fig. 3.16 (B) compared to Fig. 3.16 (A) also suggests the presence of the Pc on SiNPs.

The corresponding high resolution spectrum of the N1s component is shown in Fig. 3.17 for both the conjugate (**8-SiNPs** (linked amide)) and the SiNPs-NH$_2$ alone. Upon the deconvolution, the N1s spectrum, Fig. 3.17 (A), for the SiNPs-NH$_2$ reveals two components: N - H and N-C as expected. One peak corresponds to the free amino group (N-H) at 400.99 eV while a second peak at 397.7 eV is due to the nitrogen attached to the carbon (N-C). The N1s spectrum for **8-SiNPs** (linked amide) could be deconvoluted into three peaks (most likely due to N-H, N-C, N-C=O), Fig. 3.17 (B). The appearance of a new peak at higher binding energies (401.7ev) is thought to be due to the amide bond formation (N-C=O). Zinc is not detected as the content of the zinc component is proportionally much lower than other elements (N, C, O etc.).

Table 3.4: Apparent surface composition of silica nanoparticles as determined by XPS.

Compound	Atomic Concentration (%)			
	C(1s)	N (1s)	O (1s)	Si (2p)
SiO_2 - NH_2	57.5	1.88	27.97	12.64
8-SiNPs (linked amide)	23.18	6.32	48.25	22.25
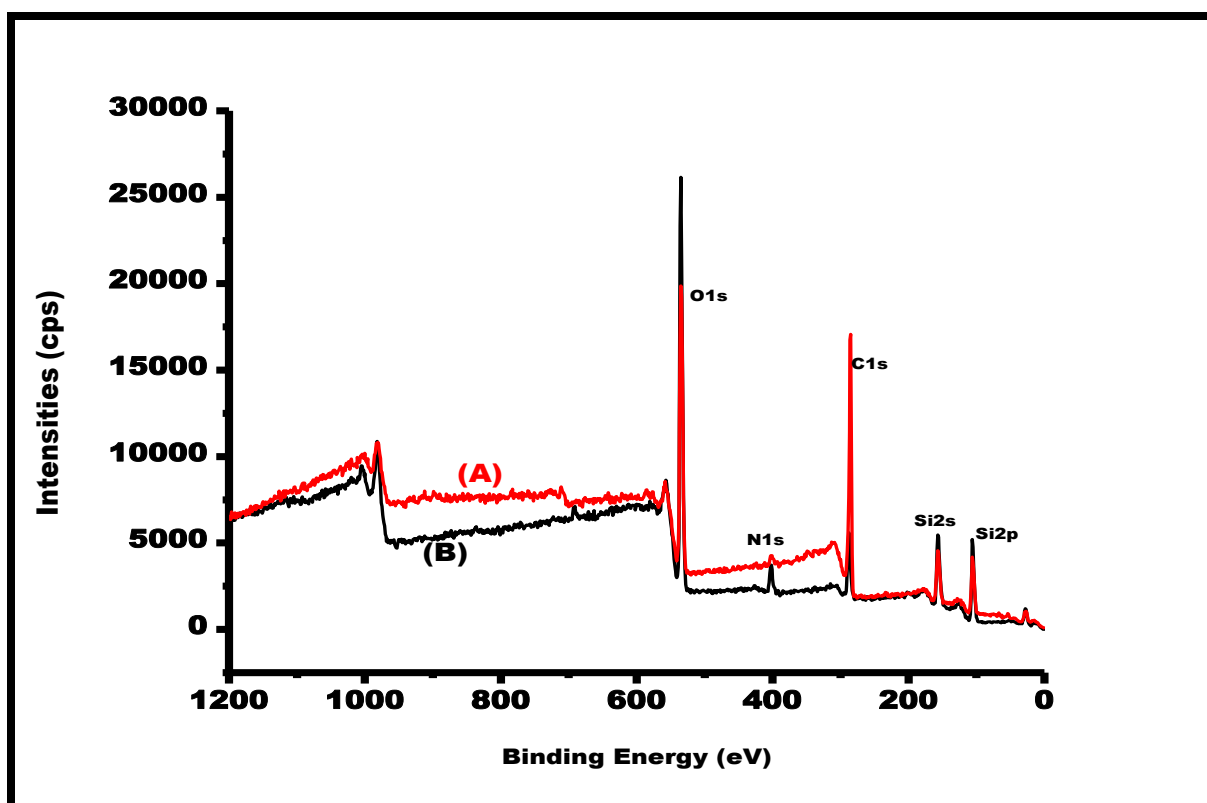
Fig. 3.16: Wide-scan X-ray photoelectron spectra of SiNPs-NH$_2$ (A) and 8–SiNPs (linked amide) (B).
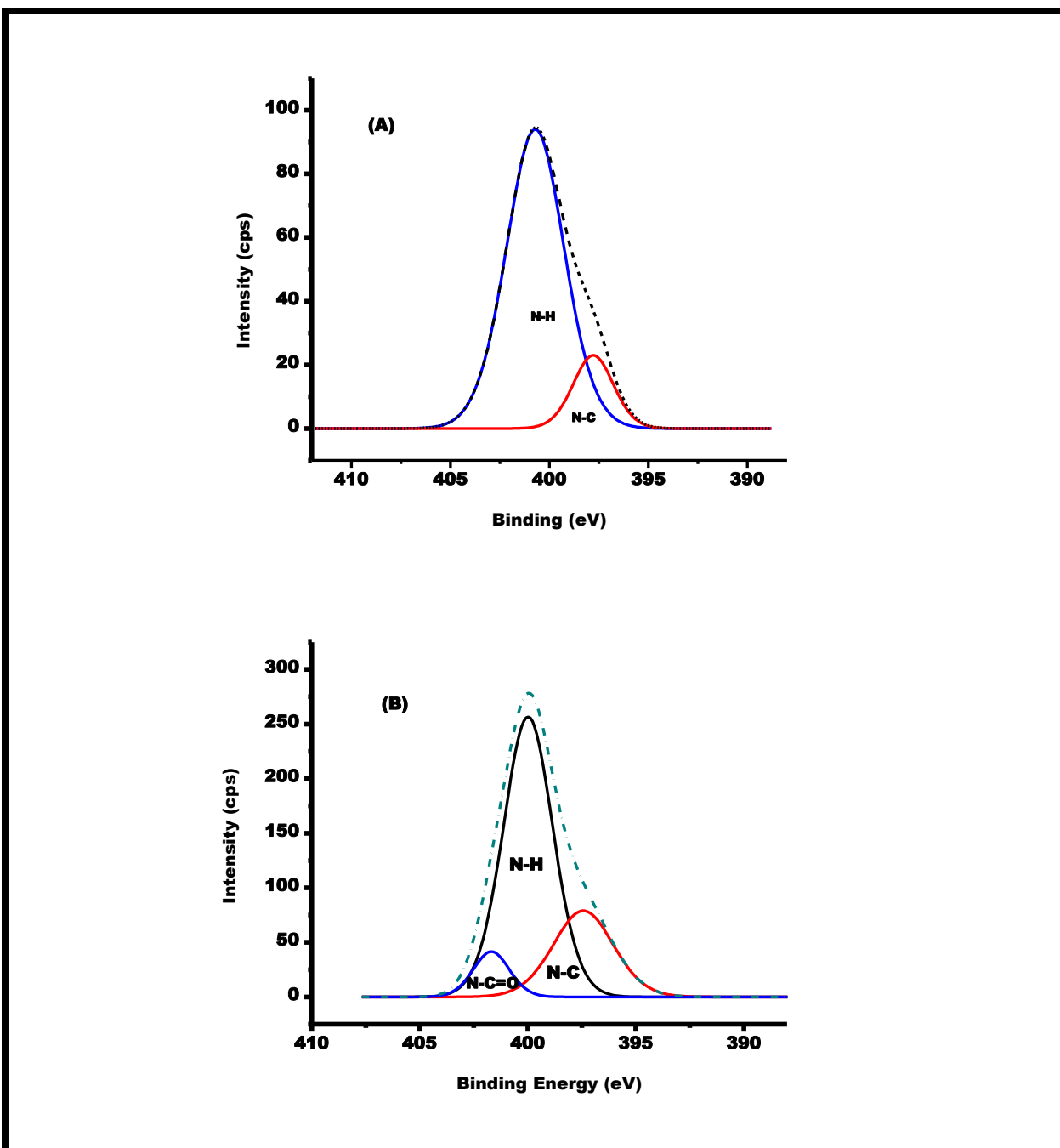
Fig. 3.17: N 1s high-resolution spectra of SiNPs-NH$_2$ (A) and 8–SiNPs (linked amide) (B).

3.3.9. UV/Vis Spectra of Conjugates

The UV-Vis spectra of all the conjugates studied in this work were recorded in DMSO. As an example, the absorption spectra of the linked conjugates compared to the MPcs and the mixed conjugates are shown in Fig. 3.18 using complexes **13** and **14** as examples. All the conjugates maintained the monomeric Q band of the Pc complexes and the shifts of the Q band on conjugation of the Pcs to the SiNPs are negligible for the both the covalently linked and the mixed conjugate, Table 3.5. This confirms the lack of aggregation for both grafted and doped Pcs in DMSO [**107, 109**]. The increase in absorbance 600 nm in Fig 3.18 (A and B) is due to the light scattering by the SiNPs. The spectrum of the SiNPs shows decreasing absorbance with increase in wavelength.
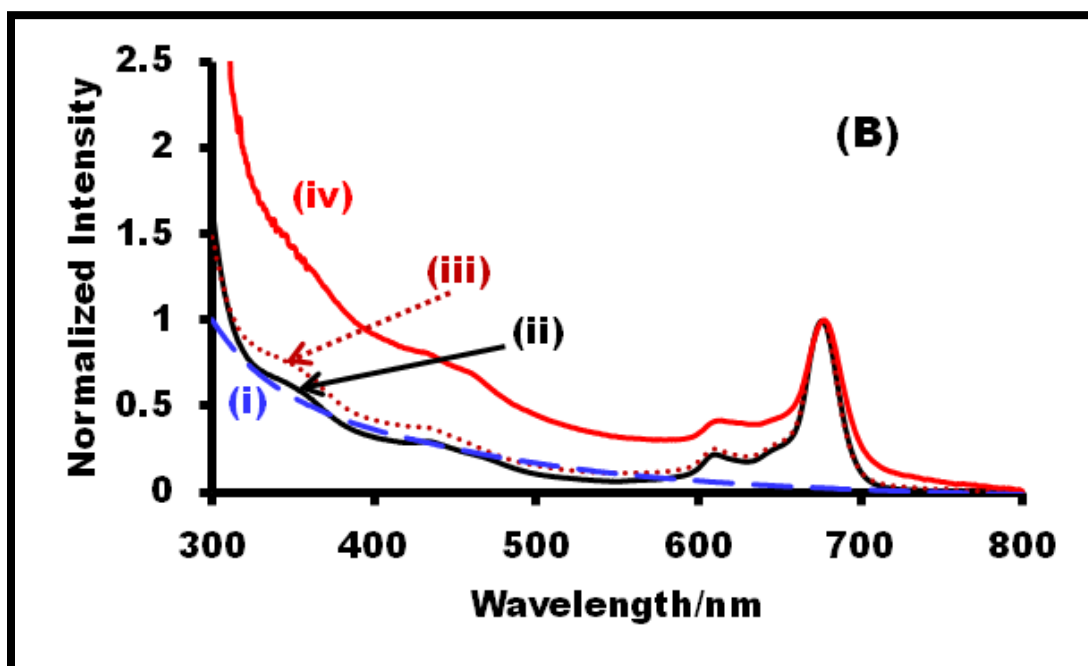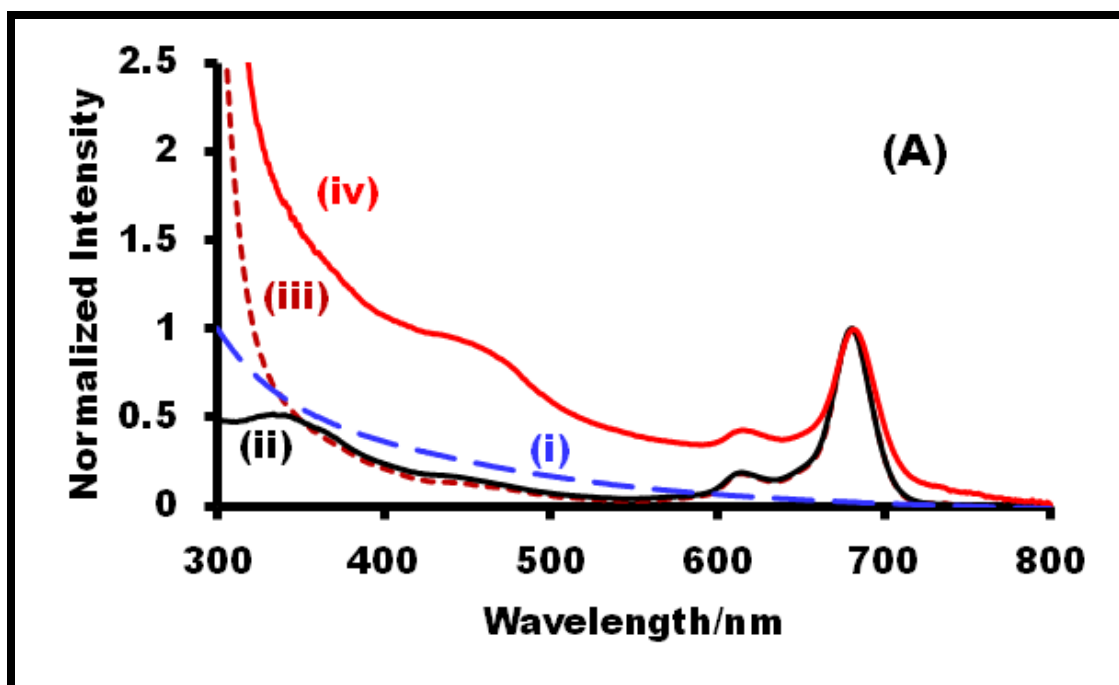
Fig. 3.18: Absorption spectra of (A) 13, (B) 14 and their conjugates (13-SiNPs (linked amide) and 14-SiNPs (linked amide) respectively). (i) SiNPs alone, (ii) 13 or 14 alone, (iii) mixed Pc- SiNPs and (iv) Pcs linked with SiNPs (amide). Solvent = DMSO.

Table 3.5: Q band maximum for the complexes and conjugates studied in this work.

Compound	Q-band maximum (nm)
8	692
8-SiNPs (linked amide)	691
8-SiNPs (linked ester)	692
8-SiNPs (doped)	692
8-SiNPs (mixed)	692
9	691
9-SiNPs (linked amide)	692
9-SiNPs (linked ester)	691
9-SiNPs (doped)	691
9-SiNPs (mixed)	691
10	679
10-SiNPs (linked amide)	680
10-SiNPs (doped)	679
10-SiNPs (mixed)	679
11	701
11-SiNPs (linked amide)	701
11-SiNPs (mixed)	701
12	685
12-SiNPs (linked amide)	683
12-SiNPs (mixed)	684
13	681
13-SiNPs (linked amide)	682
13-SiNPs (mixed)	681
14	676
14-SiNPs (linked amide)	677
14-SiNPs (mixed)	676
15	678
15-SiNPs (linked amide)	679
15-SiNPs (mixed)	678
16 (α-ZnM-3-CPPc)	677
17 (β–ZnM-3-CPPc)	674
18 (α-ZnM-4-CPPc)	677
19	677

Compound	Q-band maximum (nm)
19-SiNPs (linked click)	676
19-SiNPs (mixed)	677
20	674
20-SiNPs (linked click)	674
20-SiNPs (mixed)	674
21	677
21-SiNPs (linked click)	677
21-SiNPs (mixed)	677

Chapter Four

4.   Photophysical and Photochemical properties

This chapter reports on the photophysical and photochemical properties of the MPcs and SiNPs-MPc conjugates (linked and mixed).

4.1.   Fluorescence behavior of MPcs and Conjugates

The fluorescence properties of all the complexes and conjugates (linked and mixed) were studied in DMSO. The fluorescence spectra are mirror images of the excitation spectra for all the complexes Fig. 4.1, using complexes **10** and **10-SiNPs** (doped) as examples. The proximity of the Q band maxima of the absorption and excitation spectra for the complex **10**, Fig 4.1A suggests that the nuclear configurations of the ground and excited states are similar and not affected by excitation in DMSO. The same was observed for the conjugate **10-SiNPs** (doped), Fig 4.1B except that the absorption spectra were different from the excitation spectra, due to the light scattering by the SiNPs.
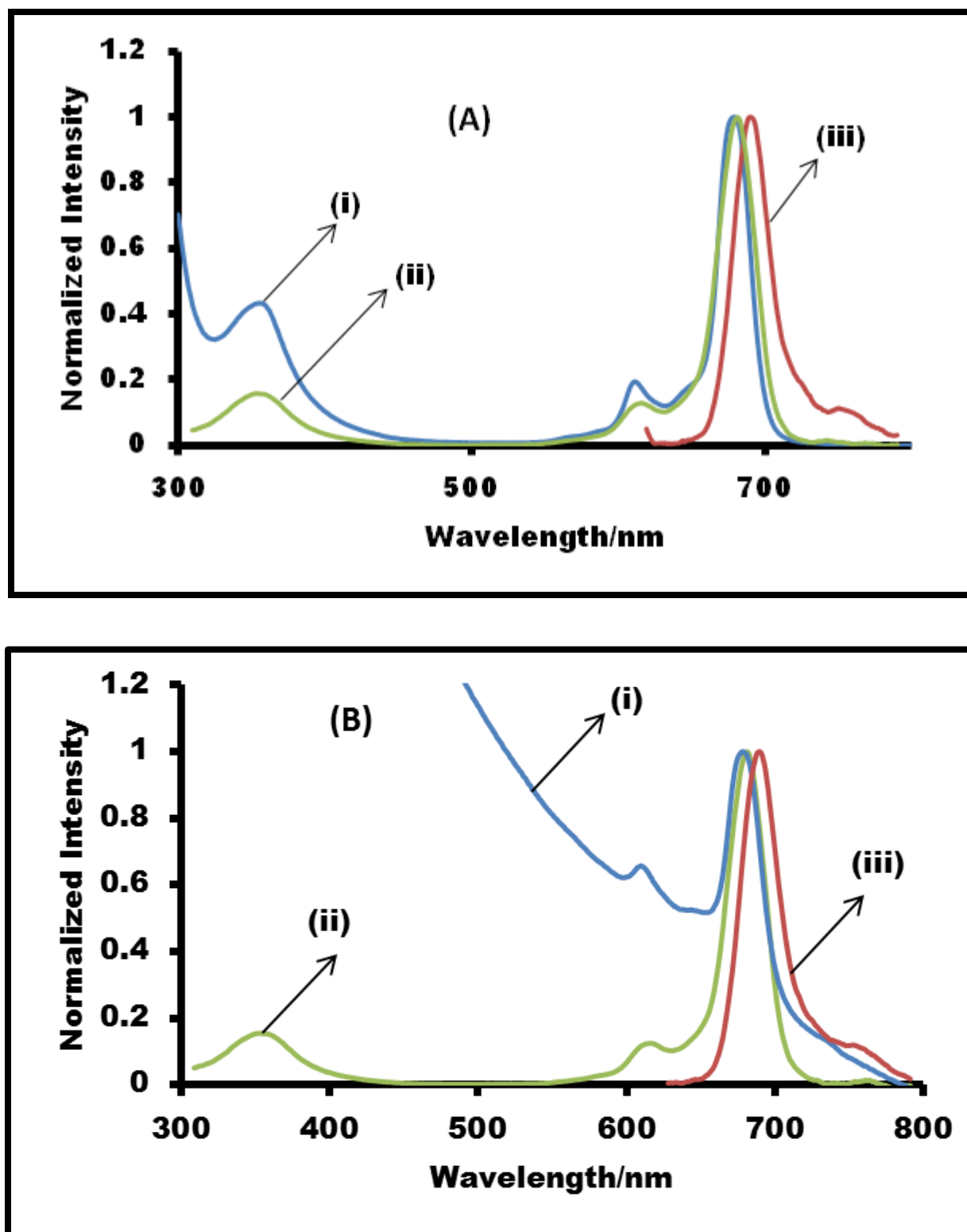
Fig. 4.1: Absorption (i), excitation (ii) and emission (iii) spectra of complexes (A) 10 and (B) 10-SiNPs (Doped) in DMSO.

4.1.1.   Fluorescence lifetimes (τ_F)

The fluorescence decay measurements were obtained by TCSPC for all the MPcs and the conjugates studies in this work. The fluorescence decay profiles for complexes **8, 9, 10, 19, 20, 21** and their respective conjugates as well as **16-18** are characterized by one exponential decay process, implying that one molecular specie is present in solution, Table 4.1. The values for the lifetimes are in the range observed for monomeric phthalocyanines [**149, 186**]. The fluorescence decay profiles for complexes **11, 12, 13, 14, 15** (all containing amino groups) and their respective conjugates are characterized by a bi-exponential decay process, implying that two molecular species are present in solution. Bi-exponential fluorescence decay profiles of phthalocyanines are attributed to the formation of ground-state dimers which can quench the monomer fluorescence, leading to a quenched (short lived) and unquenched lifetimes (long lived) [**186**]. For the conjugates, the number of lifetimes could also reflect the different orientations of the Pcs on the surface of the SiNPs after grafting. As an example, the fluorescence decay profile of complex **10** is shown in Fig 4.2. The calculation of the average fluorescence lifetime (τ_{avF}) was achieved using the values obtained from the fit and employing the following equation $\tau_{av} = \sum \alpha_i \tau_i$ (where α_i is the relative amplitude contribution to the lifetime τ_i). [**187**].
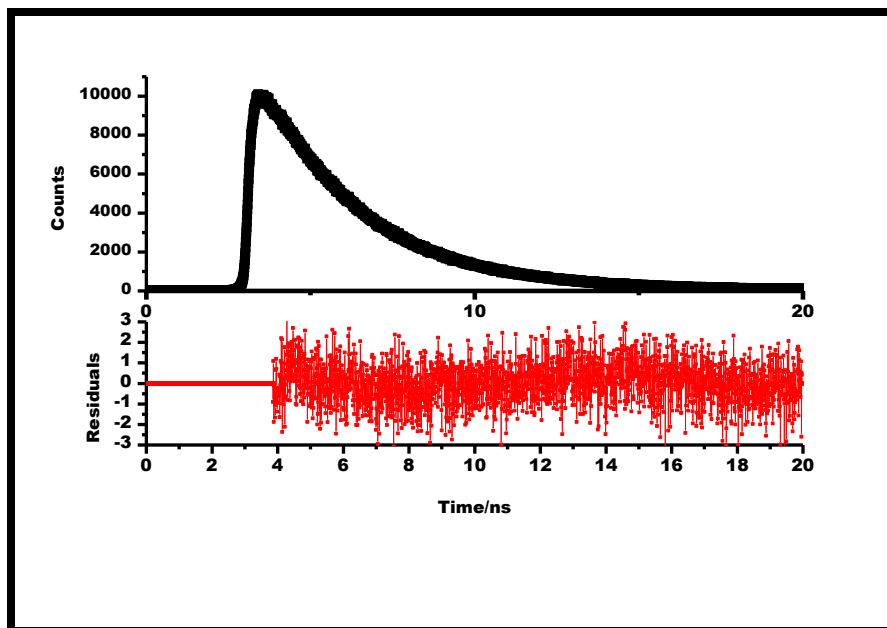
Figure 4.2: Fluorescence decay profile for complex 10 in DMSO.

Table 4.1: Fluorescence parameters of the complexes and conjugates. RA= relative amplitude.

Compound	Φ_F (±0.01)	τ_{F1}/ns (RA) ~ ±0.02	τ_{F2}/ns (RA) ~ ±0.04	τ_{avF}/ns ~ ±0.03
8	0.07	2.70 (1.00)	-	2.70
8-SiNPs (linked amide)	0.14	2.56 (1.00)	-	2.56
8-SiNPs (linked ester)	0.11	2.79 (1.00)	-	2.79
8-SiNPs (doped)	0.11	2.71 (1.00)	-	2.71
8-SiNPs (mixed)	0.07	2.63 (1.00)	-	2.63
9	0.07	2.70 (1.00)	-	2.70
9-SiNPs (linked amide)	0.13	2.68 (1.00)	-	2.68
9-SiNPs (linked ester)	0.11	2.69 (1.00)	-	2.69
9-SiNPs (doped)	0.09	2.57 (1.00)	-	2.57
9-SiNPs (mixed)	0.07	2.63 (1.00)	-	2.63
10	0.19	2.95 (1.00)	-	2.95
10-SiNPs (linked amide)	0.23	2.89 (1.00)	-	2.89
10-SiNPs (doped)	0.22	2.95 (1.00)	-	2.95
10-SiNPs (mixed)	0.19	2.94 (1.00)	-	2.94
11	0.01	2.23 (0.87)	0.61 (0.13)	2.02
11-SiNPs (linked amide)	0.02	2.17 (0.87)	0.40 (0.13)	1.94
11-SiNPs (mixed)	0.02	2.29 (0.90)	0.60 (0.10)	2.12
12	0.07	2.68 (0.89)	0.65 (0.11)	2.46
12-SiNPs (linked amide)	0.06	2.85 (0.94)	0.67 (0.06)	2.72
12-SiNPs (mixed)	0.07	2.85 (0.93)	0.43 (0.07)	2.68
13	0.12	2.86 (0.97)	0.45 (0.03)	2.79
13-SiNPs (linked amide)	0.09	2.66 (0.91)	0.52 (0.09)	2.47
13-SiNPs (mixed)	0.12	2.89 (0.96)	0.56 (0.04)	2.80
14	0.10	2.91 (0.95)	0.45 (0.05)	2.79
14-SiNPs (linked amide)	0.07	2.81 (0.90)	0.52 (0.10)	2.58

Compound	Φ_F (±0.01)	τ_{F1}/ns (RA) ~ ±0.02	τ_{F2}/ns (RA) ~ ±0.04	τ_{avF}/ns ~ ±0.03
14-SiNPs (mixed)	0.12	2.95 (0.95)	0.49 (0.05)	2.83
15	0.18	2.87 (0.95)	0.98 (0.05)	2.78
15-SiNPs (linked amide)	0.11	2.79 (0.94)	0.84 (0.06)	2.67
15-SiNPs (mixed)	0.17	2.86 (0.94)	0.81 (0.06)	2.74
16	0.12	3.11 (1.00)	-	3.11
17	0.16	3.27 (1.00)	-	3.27
18	0.14	3.01 (1.00)	-	3.01
19	0.20	2.91 (1.00)	-	2.91
19-SiNPs (linked click)	0.20	2.92 (1.00)	-	2.92
19-SiNPs (mixed)	0.20	2.89 (1.00)	-	2.89
20	0.18	3.02 (1.00)	-	3.02
20-SiNPs (linked click)	0.22	3.00 (1.00)	-	3.00
20-SiNPs (mixed)	0.19	3.05 (1.00)	-	3.05
21	0.18	2.87 (1.00)	-	2.87
21-SiNPs (linked click)	0.20	2.90 (1.00)	-	2.90
21-SiNPs (mixed)	0.18	2.89 (1.00)	-	2.89

In comparing the average fluorescence time (τ_{avF}) of complex **10** (2.95 ns) to those of complexes **8** and **9** (2.70 ns for **8** and **9** respectively)**,** it was observed that complex **10** has a longer lifetime when compared to complexes **8** and **9.** Pcs having substituent (s) at

the peripheral position usually have a higher fluorescence lifetime when compared to Pcs with same substituent at the non-peripheral position [**149, 188**]. A similar trend was observed for all the complexes studied in this work where all the peripherally substituted Pcs derivatives (**10, 12, 17** and **20**) had a higher fluorescence lifetime in comparison to their corresponding non-peripherally substituted Pc derivatives (**8**, **11**, **16**, **19** and **21**), except for **13** and **14** where the τ_{avF} are the same.

4.1.1.1   Point of Substitution

Carboxyphenoxy Substituted complexes (8-10)

The fluorescence lifetimes (2.56, 2.68 and 2.89 ns respectively) of the surface grafted SiNPs (**8-SiNPs** (linked amide), **9-SiNPs** (linked amide) and **10-SiNPs** (linked amide) showed similar behavior compared to the Pcs alone (2.70, 2.70 and 2.95 ns for **8**, **9** and **10** respectively), in that **10** had the longest τ_F. From the decrease in τ_F values, <u>it could be deduced that the fluorescence lifetime is quenched in the presence of amide bond</u>. For **8**, there is a decrease in τ_F for the amide bonded SiNPs, whereas the fluorescence lifetime (2.79 ns) of the surface grafted SiNPs ester derivative of complex **8** (**8-SiNPs** (linked ester)) shows a slight increase. The **τ_F** (2.69 ns) obtained for **9-SiNPs** (linked ester) remains unchanged compared to the Pc alone. For the mixed conjugates (**8-SiNPs** (mixed) and **9-SiNPs** (mixed) the τ_F is quenched and unchanged for **10-SiNPs** (mixed).

For complexes **8-SiNPs** (doped) and **10-SiNPs** (doped), the fluorescence lifetimes remained unchanged compared to the individual Pc complexes (**8** and **10**). However for **9-SiNPs** (doped), <u>a decrease in fluorescence lifetime</u> (2.57 ns) was observed when compared to the free complex (**9**) alone (2.70 ns). The fluorescence lifetime of the encapsulated Pc (doped) is not expected to decrease due to the protection offered by the outer silica matrix [**16, 109, 189**]. The quenching of the fluorescence lifetime in **9-SiNPs** (doped) could have resulted from <u>the loading of the Pcs within the silica matrix</u> hence resulting in aggregation and quenching of the fluorescence lifetime. Similar quenching

has also been observed when chloroaluminium phthalocyanine (ClAlPc) was doped within the silica matrix [113]. It should also be noted that the substituent (s) on complexes **8** and **10** (3-carboxyphenoxy) are the same while that of complex **9** (4-carboxyphenoxy) is different. This also indicates that the point of substitution on the phenoxy group could have affected the fluorescence lifetime of the Pcs within the silica matrix.

The doped conjugates of complexes **8-SiNPs** (doped) and **10-SiNPs** (doped)) had longer fluorescence lifetimes (2.71 and 2.95 ns for **8-SiNPs** (doped) and **10-SiNPs** (doped), respectively) compared to their amide conjugate counterparts (2.56 ns for **8-SiNPs** (linked amide) and 2.89 ns for **10-SiNPs** (linked amide)). However, the doped conjugate of complex **9** (**9-SiNP** (doped)) has a shorter lifetime (2.57 ns) when compared to the τ_F (2.68 ns) of the amide conjugate derivative **9-SiNPs** (linked amide). The behavior could also have resulted from point of substitution as described above. The ester conjugates **8-SiNPs** (linked ester) and **9-SiNPs** (linked ester) had longer lifetimes (2.79 ns and 2.69 ns) when compared to their doped derivatives (**8-SiNPs** (doped) and **9-SiNPs** (doped).

Aminophenoxy Substituted complexes (11-14)

In comparing the τ_{avF} of α (**11**) and β (**12**) symmetrically substituted complexes, it was observed that complex **12** exhibited a longer fluorescence lifetime (2.46 ns) than complex **11** (2.02 ns) in the absence of SiNPs due to peripheral substitution in the former as discussed above**.** In addition, the introduction of the phenyl substituent at the non-peripheral positions for **11** leads to the formation of a saddle-like distorted structure which affects the normal planar Pc structure [190]. This non planar deformation has been reported to enhance non radiative decay in porphyrins [191]. As a result, the lower average fluorescence lifetimes for complex **11** could be related to its possible deformation by the non-peripheral substitution. For conjugate **11-SiNPs** (linked amide), the average fluorescence lifetime (τ_{avF}) decreased in comparison to the τ_{avF} of complex

11 alone. However for conjugate **12-SiNPs** (linked amide), the τ_{avF} slightly increased in comparison to the τ_{avF} of the Pc alone (**12**). The decrease in τ_{avF} observed for conjugate **11-SiNPs** (linked amide), could be attributed to the deformed structure of the phthalocyanine molecule which might increase in proximity of the SiNPs.   The deformation could also have been enhanced if the Pc acts as a linker between SiNPs, Fig. 3.10C. The fluorescence behavior of fluorophores (such as Pcs) in the presence of nanoparticles is affected by factors such as the size of the nanoparticles and the distance separating them [**192**].

When Pcs are mixed with SiNPs without formation of a chemical bond (**11-SiNPs** (mixed) and **12-SiNPs** (mixed)), an increase in the average fluorescence lifetimes (τ_{avF}) was observed when compared to **11** or **12** alone**.** The fluorescence lifetimes may be affected by amounts of SiNPs in the mixed and linked conjugates, thus making it difficult to compare the mixed and linked complexes directly.

It was observed that complexes **13** and **14** have the same τ_{avF} (2.79 ns for each) though they are substituted at α and β position respectively. The lack of decrease in the τ_{avF} for complex **13** compared to **14** (which was observed for **11** compared to **12**) could be due to the reduced number of aminophenoxy groups on the Pc ring. The average lifetimes of **13** and **14** are quenched on conjugation to SiNPs (2.47 and 2.58 ns for **13-SiNPs** (linked amide) and **14-SiNPs** (linked amide), respectively). When Pcs are mixed with SiNPs without formation of a chemical bond (**13-SiNPs** (mixed) and **14-SiNPs** (mixed)), changes observed in the average fluorescence lifetime of the complexes were very small.

4.1.1.2   Amino groups versus Carboxylic groups (9, 11)

In comparing the τ_{avF} of complex **11** and the τ_{avF} of **9** (both complexes are symmetrical and α substituted)**,** it was observed that complex **9** (with 4-carboxyphenoxy groups) has a longer lifetime (2.70 ns) compared to the lifetime (2.02 ns) of complex **11** (with 4-aminophenoxy groups)**.** The same trend was observed for their respective conjugates (**9-**

SiNPs (linked amide) and **11-SiNPs** (linked amide)), <u>amino groups on Pcs are known to quench fluorescence</u> [**193**], hence the shorter τ_{avF} for **11**.

4.1.1.3   Amino group versus Aminophenoxy group (14, 15)

It was observed that τ_{avF} (2.79 and 2.78 ns for **14** and **15,** both β and mono-substituted with aminophenoxy and amino respectively) decreased on linking to SiNPs for **14-SiNPs** (linked amide) and **15-SiNPs** (linked amide). The τ_{avF} of the two Pcs are similar showing that the spacer present in complex **14** has no effect on the lifetime of the complexes.

When Pcs (**14** and **15**) are mixed with SiNPs without formation of a chemical bond, changes observed in the average fluorescence lifetime of the complexes were very small.

4.1.1.4   Tetra-substitution versus Mono-substitution (11-14)

For complexes **13** and **14** (both mono-substituted with a 4-amino phenoxy group in the α and β position, respectively), the τ_{avF} (2.79 ns each) are longer when compared to the τ_{avF} (2.02 and 2.46 ns respectively) of complexes **11** and **12** (both tetra-substituted with 4-amino phenoxy groups in the α and β position respectively). This implies that <u>the τ_{avF} decreases with increase in the number of amino groups on the Pc ring</u>, amino groups quench fluorescence as stated above. A similar trend was observed for the conjugates.

4.1.1.5   Clicked complexes (19-21)

For complexes **16**, **17** and **18**, the lifetimes (3.11, 3.27 and 3.01 ns respectively) decreased when compared to the lifetimes of the derived complexes **19**, **20** and **21** (2.91, 3.02 and 2.87 ns respectively). The length of the linker used to modify complexes **19**, **20** and **21** could have impacted on the lifetimes of the derived complexes thereby enhancing non radiative decay. On grafting the phthalocyanine complexes to surface of the azide functionalized SiNPs, the lifetimes of the conjugates (2.92, 3.00 and 2.90 ns for **19-SiNPs** (linked click), **20-SiNPs** (linked click) and **21-SiNPs** (linked click) respectively) did not change significantly when compared to those of the derived complexes alone (**19**, **20** and **21**) indicating that the lifetimes are not quenched in the presence of the nanoparticles.

The average lifetimes of complexes **19** and **21** (2.91 and 2.87 ns respectively) are longer when compared to the τ_{avF} of complex **13** (2.79 ns). The three complexes are mono-substituted and α substituted with **19** having a 4-((hex-5-ynyl)-benzoate) phenoxy, **21** with a 3-((hex-5-ynyl)-benzoate) phenoxy group while complex **13** has a 4-aminophenoxy group as substituent. The different substituent could have accounted for the longer times observed for complexes **19** and **21** since amino groups quench fluorescence**.** A similar trend is observed when complex **20** (3-((hex-5-ynyl)-benzoate) phenoxy group) is compared to complex **14** (with 4-aminophenoxy as substituent)**,** both complexes are mono-substituted and β substituted.

4.1.2.   Fluorescence Quantum yield (Φ_F)

The fluorescence quantum yields (Φ_F) values were determined by the comparative method in DMSO [**94**]. The Φ_F values obtained for all the Pc complexes and the conjugates are highlighted in Table 4.1.

4.1.2.1   Point of Substitution

Carboxyphenoxy Substituted complexes (8-10)

The efficiency of the fluorescence process (Φ_F) was observed to be better in complex **10** (0.19) compared to complexes **8** and **9** (0.07 for each). The <u>substitution position</u> (complex **10** is β substituted while **8** and **9** are α substituted) on the Pc ring could have contributed to the improvement in fluorescence corresponding to longer τ_F at the β position [**188**]. The fluorescence quantum yields of the surface grafted SiNPs (**8-SiNPs** (linked amide), **9-SiNPs** (linked amide) and **10-SiNPs** (linked amide)) showed improvement in comparison to the Pc complexes alone (**8, 9** and **10** respectively). The observed <u>increase in the quantum yield</u> of the conjugates might be due to the <u>close grafting of the Pcs on the surface of the SiNPs</u>, thereby increasing the <u>efficiency of the fluorescence process</u> [**32**].

Similar improvements in Φ_F were observed for conjugates **8-SiNPs** (linked ester), **8-SiNPs** (doped), **9-SiNPs** (linked ester), **9-SiNPs** (doped) and **10-SiNPs** (doped) when compared to the Φ_F of complexes **8, 9** and **10** respectively**.** The slight improvement observed for the doped nanoparticles (**8-SiNPs** (doped), **9-SiNPs** (doped) and **10-SiNPs** (doped)) compared to the Pc alone could be as a result of the <u>protection of the Pc rich core by the outer silica shell and also silica has been found to provide a rigid environment that enhances dye performance</u> [**3, 33**].

When Pcs are mixed with SiNPs (**8-SiNPs** (mixed), (**9-SiNPs** (mixed) and (**10-SiNPs** (mixed)) without a chemical bond, no increase in quantum yield was observed.

Aminophenoxy Substituted complexes (11-14)

The Φ_F of complexes **11** and **12** were calculated to be 0.01 and 0.07 respectively, Table 4.1. The low values could be attributed to the quenching of the fluorescence by the

amino substituent (s) on the Pc ring. However, **13** (Φ_F= 0.12) and **14** (Φ_F= 0.10) have higher Φ_F <u>due to fewer amino groups.</u>

The fluorescence quantum yields of both conjugates **11-SiNPs** (linked amide) and 1**2-SiNPs** (linked amide) were unquenched in DMSO when compared to complexes **11** and **12** alone. The same applies when the Pcs are mixed with SiNPs (**11-SiNPs** (mixed) and 1**2-SiNPs** (mixed)) without a chemical bond. The Φ_F of the amide bonded conjugates of **13** and **14** (1**3-SiNPs** (linked amide) and 1**4-SiNPs** (linked amide)) were quenched on conjugation to SiNPs. The slight decrease in fluorescence quantum <u>yields could reflect aggregation in the conjugates.</u>

When Pcs are mixed with SiNPs (**13-SiNPs** (mixed) and (**14-SiNPs** (mixed)) without a chemical bond, no quenching of the complexes was observed.

4.1.2.2   Amino groups versus Carboxylic groups (9, 11)

In general, the α substituted symmetrical complex containing carboxyphenoxy substituents (**9**) showed better fluorescent properties as compared to the α symmetrical complex with 4-aminophenoxy groups (**11**) due to quenching of the excited state by the amino groups. The same trend was observed for their β substituted symmetrical derivatives.

4.1.2.3   Amino group versus Aminophenoxy group (14, 15)

The Φ_F of complex **15** was found to be better compared to complex **14,** though the two complexes have amino groups, the amino group in complex **15** is directly linked to the Pc ring while that of complex **14** is separated by a spacer, a phenoxy group. Thus <u>the lack of spacer in complex **15** could have resulted in less quenching.</u> The effect of the amino group on the Φ_F of complex **15** can be evaluated by comparing its Φ_F (0.18) with

that of un-substituted ZnPc (0.2) [**95**]. It can be observed that the Φ_F of complex **15** decreased slightly as a result of the single amino group on the Pc ring.

The fluorescence quantum yields of all the conjugates **14-SiNPs** (0.07) and **15-SiNPs** (0.11) were slightly quenched in DMSO when compared to **14** (0.10) and **15** (0.18) alone. The slight decrease in fluorescence quantum yields could reflect aggregation in the conjugates.

4.1.2.4   Tetra-substitution versus Mono-substitution (11-14)

In comparing the fluorescent properties of complexes **11** and **12** (both tetra-substituted with 4-aminophenoxy groups) with complexes **13** and **14** (both mono-substituted with 4-aminophenoxy groups), it was observed that the mono-substituted complexes (**13** and **14**) showed better fluorescent properties compared to symmetrical complexes (**11** and **12**) at both the α and β positions. This implies that the less amino groups for **13** and **14** could have resulted in less quenching compared to **11** and **12**. A similar trend was observed for the conjugates.

4.1.2.5   Clicked Complexes (19-21)

The fluorescence quantum yield of the derived complexes (**19**, **20** and **21**) increased when compared to those of complexes **16**, **17** and **18**. This indicates that a slight modification of the phthalocyanine complexes could impact on the photophysical properties of the newly formed complexes. Introduction of the groups containing a triple bond has been reported to increase fluorescence rate [**194**]. This could explain the observed increase in fluorescence quantum yields for complexes **19**, **20** and **21** compared to the corresponding complexes **16**, **17** and **18.**

The fluorescence quantum yield of **19-SiNPs** (0.20) did not change when compared to **19** (0.20) alone. The quantum yields of **20-SiNPs** and **21-SiNPs** (0.22 and 0.20

respectively) slightly increased in comparison to **20** and **21** alone (both at 0.18). When mixed (without the formation of a chemical bond, the fluorescence quantum yield of all the mixed conjugates (**19-SiNPs** (mixed)**, 20-SiNPs** (mixed) and **21-SiNPs** (mixed)) remained unchanged when compared to the quantum yield of the derived phthalocyanine complexes alone (**19**, **20** and **21**).

The Φ_F of complexes **19** and **21** (0.20 and 0.18 respectively) are better when compared to the Φ_F of complex **13** (0.12). The three complexes are mono-substituted and α substituted with **19** having a 4-((hex-5-ynyl)-benzoate) phenoxy, **21** with a 3-((hex-5-ynyl)-benzoate) phenoxy group while complex **13** has a 4-aminophenoxy group as substituent. A similar trend is observed when complex **20** (3-((hex-5-ynyl)-benzoate) phenoxy group) is compared to complex **14** (with 4-aminophenoxy as substituent)**,** both complexes are mono-substituted and β substituted.

4.2.   Triplet quantum yields (Φ_T) and lifetimes (τ_T) of MPcs and Conjugates

The triplet quantum yields and lifetimes were determined using laser flash photolysis. The triplet decay curve of the complexes and conjugates are consistent with the first order kinetics, Fig. 4.3, using conjugate **10-SiNPs** (doped) as an example. The lifetime and the quantum yield of the triplet state were determined at a wavelength of 490 nm. The triplet quantum yields and the corresponding lifetimes of the phthalocyanines complexes and their conjugates are listed in Table 4.2.
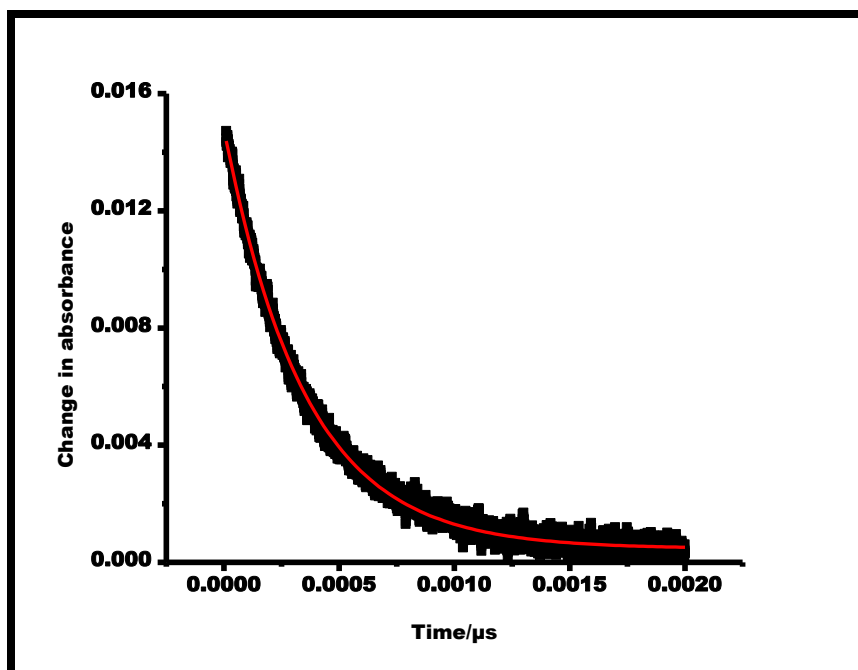
Figure 4.3: Triplet decay curve of complex 10-SiNPs (doped) in DMSO at 490 nm

4.2.1.   Triplet Quantum yield (Φ_T)

4.2.1.1   Point of Substitution

Carboxyphenoxy Substituted complexes (8-10)

Triplet quantum yield (Φ_T) is a measure of the efficiency of intersystem crossing (ISC) from the excited singlet to the excited triplet state. The efficiency of the ISC process in complex **8** with 3-carboxyphenoxy groups is better when compared to complex **9** (has 4-carboxyphenoxy groups), both are α substituted, this suggests that the point of substitution on the phenoxy group affects the ISC process. In comparing the Φ_T of complex **8** (0.41) to that of complex **10** (0.54), complex **10** has a better Φ_T, Table 4.2. This also implies that point of substitution on the Pc ring also impacts on the ISC process, both complexes have same substituent (s) but are substituted at the α (**8**) and β (**10**)

positions, hence the β position is better than the α position. This could have resulted from less steric hindrance at the β position.

Tables 4.2, shows that higher Φ_T were obtained for conjugates **8-SiNPs** (linked amide), **9-SiNPs** (linked amide) and **10-SiNPs** (linked amide) compared to the free phthalocyanine complexes (**8**, **9** and **10**). The observed increase in Φ_T could be attributed to the presence of the polymeric SiNPs which supports the ISC process. Similar increase in Φ_T was observed for the ester conjugates (**8-SiNPs** (linked ester) and **9-SiNPs** (linked ester)) compared to complexes **8** and **9.**

In comparing the amide (**8-SiNPs** (linked amide) and **9-SiNPs** (linked amide) and the ester (**8-SiNPs** (linked ester) and **9-SiNPs** (linked ester) conjugates, it was observed that the ISC process was more efficient in the ester conjugates. The observed efficiency could have resulted from the length of the bond between the SiNPs and the Pc complexes, the amide conjugates have longer length hence the possibility of more energy loss by non radiative pathways.

The Φ_T of the doped conjugates (**8-SiNPs** (doped), **9-SiNPs** (doped) and **10-SiNPs** (doped)) showed improvement when compared to those of the surface grafted nanoparticles (**8-SiNPs** (linked amide), **9-SiNPs** (linked amide) and **10-SiNPs** (linked amide)). The observed improvement in the efficiency of the ISC process could be attributed to the protective cover of the silica matrix and the packing of the phthalocyanine complexes within the silica matrix. It should be highlighted that for the conjugates of complexes **8**, **9** and **10**, an increase in triplet quantum yields was also accompanied by an increase in fluorescence quantum yields showing the benefits of linking Pcs to SiNPs. The two processes are competing processes but the silica protection enhanced both processes.

When Pcs and SiNPs are mixed without a chemical bond, there is also an increase in triplet quantum yields for **8-SiNPs** (mixed) and **9-SiNPs** (mixed) while a slight decrease is observed in **10-SiNPs** (mixed). However, it is difficult to compare the mixed and linked conjugates since the amounts of SiNPs will not be the same in both. Even though

equal amount of SiNPs and Pcs were used in both mixed and linked, the amount will not be the same due to the purification process involved of the latter.

Aminophenoxy Substituted complexes (11-14)

In comparing the Φ_T of complex **11** (Φ_T = 0.26) to that of complex **12** (Φ_T = 0.65), complex **12** has a better Φ_T. This also implies that point of substitution on the Pc ring also impacts on the ISC process, both complexes have same substituents but are substituted at the α (**11**) and β (**12**) positions hence substitution at the β position is better than the α position. It was observed that the triplet quantum yield for conjugate **12-SiNPs** (linked amide) decreased in comparison to **12** alone while an increase was observed for **11-SiNPs** (linked amide) in relation to **11** alone. It should be noted that it is possible that some Pcs may interlink with the SiNPs, Fig 3.9C, especially the peripherally substituted Pc (**12**). This type of arrangement could quench the excited states. Peripheral substituent(s) are oriented in a manner which makes linking more favored than the non-peripheral position.

When Pcs (**11** and **12**) and SiNPs are mixed without a chemical bond, there is also an increase in triplet quantum yields for **11-SiNPs** (mixed) and **12-SiNPs** (mixed).

The efficiency of the ISC process in complex **13** (Φ_T = 0.83) is better when compared to complex **14** (Φ_T = 0.76) this suggests that the point of substitution (α (**13**) vs β (**14**)) on the Pc ring affects the ISC process contradicting the observation above where the β position was better than the α position. Both complexes have a 4-aminophenoxy substituent and the Φ_T may have been affected by the presence of only one amino group. A slight increase in triplet quantum yield was observed for the linked conjugates (**13-SiNPs** (linked amide) and **14-SiNPs** (linked amide)) when compared to the Pc complexes alone (**13** and **14**), Table 4.2.

When Pcs (**13** and **14**) and SiNPs are mixed without a chemical bond, no significant change in triplet quantum yield is observed for **13-SiNPs** (mixed) while a decrease is observed in **14-SiNPs** (mixed).

4.2.1.2   Amino groups versus Carboxylic groups (9, 11)

In comparing the effect of substituent type on the Φ_T, complexes **9** (with 4-carboxyphenoxy) and **11** (with 4-aminophenoxy), it was observed that ISC process is more efficient in complex **9** and a comparable increase in Φ_T was observed for their respective conjugates (**9-SiNPs** (linked amide) and **11-SiNPs** (linked amide) respectively). The less efficiency observed in complex **11** could be due to quenching by the amino groups.

4.2.1.3   Amino group versus Aminophenoxy group (14, 15)

In comparing complexes **14** and **15**, both complexes β mono-substituted and have a terminal amino group, though **14** has a spacer between Pc ring and the amino group, complex **14** has a higher Φ_T compared to complex **15,** showing that in the absence of the spacer, the ISC process is quenched. The larger Φ_T of **14** corresponds to a lower Φ_F compared to complex **15.** It was also observed that conjugate **14-SiNPs** (linked amide) has a higher Φ_T compared to **15-SiNPs** (linked amide). For **15-SiNPs** (linked amide), there was no significant change in triplet quantum yield when compared to Pc (**15)** alone.

When the Pcs (**14** and **15**) and SiNPs are mixed without a chemical bond, a decrease in triplet quantum yield is observed for **14-SiNPs** (mixed) and **15-SiNPs** (mixed).

4.2.1.4   Tetra-substitution versus Mono-substitution (11-14)

In comparing the Φ_T of complexes **11** and **12** (both tetra-substituted with 4-aminophenoxy groups) with complexes **13** and **14** (both mono-substituted with 4-aminophenoxy groups), it was observed that the mono-substituted complexes (**13** and **14**) have a more efficient ISC process compared to the symmetrical complexes (**11** and **12**) at both the α and β positions. This implies that with reduced number of amino

groups at both α and β position, the ISC process is affected and less quenching is observed. A similar trend was observed for the conjugates.

4.2.1.5   Clicked Complexes (19-21)

For the derived phthalocyanine complexes (**19**, **20** and **21**), the triplet quantum yield (0.71, 0.60 and 0.65 respectively) increased significantly when compared to the Pc complexes **16**, **17** and **18** (0.49, 0.41 and 0.38 respectively). It would have been expected that if the substituent increase the fluorescence quantum yields, they would decrease the triplet yields since these are competing processes. However both triplet and fluorescence yields increased. It has been reported that the presence of triple bonds enhance both the fluorescence and intersystem crossing [**194**].

The increase in triplet quantum yield for **19**, **20** and **21** could also be explained in terms of symmetry, it has been reported that low symmetry results in large intersystem crossing to the triplet state [**195, 196**]. The phenoxy groups, which are bulky substituents, have been reported to result in low symmetry. This loss in symmetry is more pronounced at the α position due to steric hindrance. Prior to conjugation, complexes **16, 17** and **18** have carboxylic groups attached to the phenoxy groups making it bulkier, however, on conjugation to 5-hexyn-1-ol, the bulkiness of the substituent is further increased, hence a further loss of symmetry leading to the observed increase in the triplet quantum yield of complexes **19, 20** and **21.** It was also observed that complexes **19** and **21** which are α substituted showed improved Φ_T compared to **20**, contradicting the earlier observation that β position is better than the α position**.**

A significant decrease in triplet quantum yield was observed for all the linked conjugates (**19-SiNPs** (linked click), **20-SiNPs** (linked click) and **21-SiNPs** (linked click)) when compared to the Pc complexes alone (**19, 20** and **21** alone). The decrease in Φ_T observed in the conjugates could be due to the type of bond formed between the silica nanoparticles and the complexes. Also, the ability of the conjugates to retain (**19-SiNPs**

(linked click)) and improve (**20-SiNPs** (linked click) and **21-SiNPs** (linked click)) on the fluorescent properties of the Pc could also have contributed because the ISC process and the fluorescence process are competing processes.

Complex **13** has a more efficient ISC process (Φ_T = 0.83) compared to complexes **19** and **21** (Φ_T =0.71 and 0.65 respectively). The three complexes are asymmetrical and α substituted with **19** having a 4-((hex-5-ynyl)-benzoate) phenoxy, **21** with a 3-((hex-5-ynyl)-benzoate) phenoxy group while complex **13** has a 4-aminophenoxy group as substituent. Complex **20** (3-((hex-5-ynyl)-benzoate) phenoxy group) showed a less efficient ISC process compared to complex **14** (with 4-aminophenoxy as substituent), both complexes are asymmetrical and β substituted.

4.2.2.   Triplet lifetimes (τ_T)

All the complexes and conjugates studied in this work were degassed to ensure that the triplet state parameters are accurately determined and also to prevent oxygen from quenching the triplet state [**197**]. The τ_T ranged from 234 - 484 µs for the conjugates and from 161 to 366 µs for the free phthalocyanine complexes, this indicates that all complexes and conjugates have long-lived excited triplet state. Zinc phthalocyanine complexes are known to produce high triplet yields with long lifetimes [**89**, **100**]. τ_T are expected to be longer where Φ_T is smaller [**98**].

4.2.2.1   Point of Substitution

Carboxyphenoxy Substituted complexes (8-10)

Both the amide and the doped conjugates of complexes **8**, **9** and **10** showed significant increase in triplet lifetime when compared to the free phthalocyanines. The increase in triplet lifetimes could be <u>due to the protection provided for the Pc complexes</u> by the

polymeric SiNPs. A similar trend was observed for the ester conjugate of complex **8** (**8-SiNPs** linked ester) and **9** (**9-SiNPs** linked ester). It was also observed that for all the conjugates of complexes **8**, **9** and **10** the increase in τ_T also corresponded with an increase in Φ_T, contrary to the expected decrease of τ_T with increase in Φ_T, due to the protection discussed above.

In comparing the τ_T of complexes **8** (174 µs) and **10** (337 µs), it was observed that complex **10** had a longer τ_T, this shows that the point of substitution on the Pc ring also impacts on the τ_T. Both complexes are substituted with 3-carboxyphenoxy groups at the α (**8**) and β (**10**) positions. The same trend was observed for their respective amide conjugates (249 µs for **8-SiNPs** (linked amide) and 391 µs for **10-SiNPs** (linked amide)).

In comparing the effect of the point of substitution on the phenoxy group on the τ_T, we look at complexes **8** and **9**. The triplet state of complex **8** (174 µs) is short lived in comparison to complex **9** (215 µs), a similar trend was also observed for their respective amide conjugates (249 µs for **8-SiNPs** (linked amide) and 412 µs for **9-SiNPs** (linked amide)). However, the reverse was observed for their respective ester conjugates (444 µs for **8-SiNPs** (linked ester) and 343 µs for **9-SiNPs** (linked ester)). This also shows the importance of the type of linkage between the SiNPs and the Pcs.

When the Pcs (**8**, **9** and **10**) and SiNPs are mixed without a chemical bond, an increase in triplet lifetimes is observed for **8-SiNPs** (mixed) and **9-SiNPs** (mixed) while no significant change was observed for **10-SiNPs** (mixed).

Aminophenoxy Substituted complexes (11-14)

The τ_T of complexes **11** (323 µs) and **12** (339 µs) are comparable, though complex **12** has a slightly longer τ_T. This implies that the point of substitution on the Pc ring also impacts on the τ_T, both complexes are substituted with 4-aminophenoxy groups at the α (**11**) and β (**12**) positions. For their respective conjugates, an improvement in τ_T (333 µs) is observed for **11-SiNPs** (linked amide) while a decrease in τ_T (234 µs) is observed for **12-SiNPs** (linked amide). It should also be noted that the increase in τ_T observed for **11-**

SiNPs (linked amide) corresponded with an increase in Φ_T, while the decrease observed in τ_T for **12-SiNPs** (linked amide) corresponds to a decrease in Φ_T in the latter.

When the Pcs (**11** and **12**) and SiNPs are mixed without a chemical bond, a increase in triplet lifetimes is observed for **12-SiNPs** (mixed) while a decrease in triplet lifetimes is observed for **11-SiNPs** (mixed).

The triplet state lifetime in complex **13**, α substituted (357 μs) is longer when compared to complex **14**, β substituted (326 μs). An increase in Φ_T was also observed for **13** compared to **14**. Both complexes are mono-substituted and have a 4-aminophenoxy substituent.

A significant increase in τ_T was observed for the linked conjugate (**13-SiNPs** (linked amide) compared to the Pc alone. The increase in τ_T observed for **13-SiNPs** (linked amide) corresponded with an increase in Φ_T. A decrease in τ_T was obtained for **14-SiNPs** (linked amide) corresponding to an increase in Φ_T, as expected.

When the Pcs (**13** and **14**) and SiNPs are mixed without a chemical bond, a decrease in τ_T is observed for **13-SiNPs** (mixed) while a slight increase was observed for **14-SiNPs** (mixed).

4.2.2.2   Amino groups versus Carboxylic groups (9, 11)

In comparing the effect of substituent type on the τ_T, complexes **9** (with 4-carboxyphenoxy) and **11** (with 4-aminophenoxy) are compared. The triplet state lifetime of the complex **11** is longer in comparison to complex **9**, an increase in Φ_T was also observed for **11** compared to **9**, though the reverse was observed for their respective conjugates (**9-SiNPs** (linked amide) and **11-SiNPs** (linked amide) respectively).

4.2.2.3   Amino group versus Aminophenoxy group (14, 15)

In comparing complexes **14** and **15**, both complexes β substituted and have a terminal amino group though **14** has a spacer between Pc ring and the amino group. Complex **14** has a longer τ_T compared to complex **15,** showing that in the absence of the spacer the τ_T is quenched as was the case with Φ_T.

For **15-SiNPs** (linked amide) a significant increase in τ_T when compared to **15** alone though no change in Φ_T is observed.

When the Pcs (**14** and **15**) and SiNPs are mixed without a chemical bond, a slight increase was observed for **14-SiNPs** (mixed) and **15-SiNPs** (mixed).

4.2.2.4   Tetra-substitution versus Mono-substitution (11-14)

In comparing the τ_T of complexes **11** and **12** (both tetra-substituted with 4-aminophenoxy groups) with complexes **13** and **14** (both mono-substituted with 4-aminophenoxy groups), it was observed that the α mono-substituted complex (**13**) has a longer lifetime compared to the α tetra-substituted complex (**11**). However, the reverse was observed for the β substituted complexes where complex **12** (339 μs) had the longer lifetime compared to complex **14** (326 μs). For the conjugates, it was observed that the mono-substituted conjugates (**13** (linked amide) and **14**) (linked amide) have a longer τ_T compared to the tetra-substituted conjugates (**11** (linked amide) and **12** (linked amide)) at both the α and β positions, due to fewer amino groups in the former.

4.2.2.5   Clicked Complexes (19-21)

For the derived phthalocyanine complexes (**19**, **20** and **21**), the τ_T (343, 341 and 366 μs respectively) increased when compared to the Pc complexes **16**, **17** and **18** (168, 161 and 200 μs respectively). The longer triplet lifetimes observed in complexes **19**, **20** and **21** implies that the alkyne terminated complexes are less efficient at dissipating the energy

of the excited triplet state compared to the carboxylic terminated complexes **16**, **17** and **18** [95].

An increase in triplet state lifetimes was observed for all the linked conjugates (**19-SiNPs** (linked click), **20-SiNPs** (linked click) and **21-SiNPs** (linked click)) when compared to the Pc complexes alone (**19, 20** and **21** alone). The observed increase in τ_T corresponds to a decrease in Φ_T for all the conjugates**.**

When the Pcs (**19, 20** and **21**) and SiNPs are mixed without a chemical bond, an increase in τ_T was observed for conjugates (**19-SiNPs** (mixed) and **21-SiNPs** (mixed)) while no significant change is observed for **20**.

Table 4.2: Triplet quantum yield (Φ_T), triplet lifetime (τ_T), singlet oxygen quantum yield (Φ_Δ), fraction of the triplet state quenched by triplet state oxygen (S_Δ), quantum of internal conversion (Φ_{IC}) and intersystem crossing times (τ_{isc}) of the complexes and their respective conjugates in DMSO.

Compound	Φ_T	$\tau_T/\mu s$	Φ_Δ	S_Δ	Φ_{IC}	τ_{isc}/ns
8	0.41	174	0.30	0.73	~0.52	6.59
8-SiNPs (linked amide)	0.44	249	0.19	0.43	~0.42	5.82
8-SiNPs (linked ester)	0.59	444	0.23	0.39	~0.3	4.73
8-SiNPs (doped)	0.56	314	0.48	0.86	~0.33	4.84
8-SiNPs (mixed)	0.59	242	0.29	0.49	~0.34	4.46
9	0.38	215	0.31	0.82	~0.55	7.11
9-SiNPs (linked amide)	0.48	412	0.38	0.79	~0.39	5.58
9-SiNPs (linked ester)	0.77	343	0.22	0.29	~0.12	3.49
9-SiNPs (doped)	0.59	343	0.47	0.80	~0.32	4.36
9-SiNPs (mixed)	0.45	296	0.24	0.53	~0.48	5.84
10	0.54	337	0.27	0.50	~0.27	5.46
10-SiNPs (linked amide)	0.58	391	0.22	0.38	~0.19	4.98
10-SiNPs (doped)	0.61	352	0.30	0.49	~0.17	4.84
10-SiNPs (mixed)	0.52	430	0.11	0.21	~0.29	5.65
11	0.26	323	0.22	0.85	~0.73	7.77
11-SiNPs (linked amide)	0.49	333	0.40	0.82	~0.49	3.96
11-SiNPs (mixed)	0.62	288	0.55	0.89	~0.36	3.42
12	0.65	339	0.42	0.65	~0.28	3.78
12-SiNPs (linked amide)	0.50	234	0.20	0.40	~0.44	5.44
12-SiNPs (mixed)	0.70	357	0.53	0.76	~0.23	3.83
13	0.83	357	0.50	0.60	~0.05	3.36
13-SiNPs (linked amide)	0.87	416	0.51	0.59	~0.04	2.84
13-SiNPs (mixed)	0.85	331	0.58	0.68	~0.03	3.29

Compound	Φ_T	$\tau_T/\mu s$	Φ_Δ	S_Δ	Φ_{IC}	τ_{isc}/ns
14	0.76	326	0.31	0.41	~0.14	3.67
14-SiNPs (linked amide)	0.80	307	0.29	0.36	~0.13	3.23
14-SiNPs (mixed)	0.66	350	0.36	0.55	~0.22	4.29
15	0.58	252	0.50	0.86	~0.24	4.79
15-SiNPs (linked amide)	0.59	459	0.54	0.92	~0.3	4.53
15-SiNPs (mixed)	0.51	255	0.47	0.92	~0.32	5.37
16	0.49	168	0.17	0.35	~0.39	6.35
17	0.41	161	0.15	0.37	~0.43	7.98
18	0.38	200	0.18	0.47	~0.48	7.92
19	0.71	343	0.35	0.49	~0.09	4.10
19-SiNPs (linked click)	0.40	352	0.26	0.65	~0.4	7.30
19-SiNPs (mixed)	0.61	388	0.28	0.50	~0.19	4.74
20	0.60	341	0.40	0.67	~0.22	5.03
20-SiNPs (linked click)	0.49	373	0.30	0.61	~0.29	6.12
20-SiNPs (mixed)	0.64	342	0.48	0.75	~0.17	4.77
21	0.65	366	0.35	0.54	~0.17	4.42
21-SiNPs (linked click)	0.37	484	0.18	0.49	~0.43	7.84
21-SiNPs (mixed)	0.67	448	0.40	0.60	~0.15	4.31

4.3.   Singlet Oxygen quantum yields (Φ_Δ)

The singlet oxygen values are expected to depend on the corresponding triplet quantum yield (Φ_T) values of the complexes. This implies that if the triplet state of the MPc is populated, it can then interact with molecular oxygen and excite it to its singlet excited state. In this work, the singlet oxygen quantum yields of the complexes were determined using an optical method bases on time-resolved near-IR phosphorescence decay of singlet oxygen. As an example, Fig 4.4 shows the singlet oxygen phosphorescence decay profile of complex **21**. The singlet oxygen quantum yield of all the complexes and conjugates are shown in Table 4.2. The fraction of the triplet state quenched by triplet state oxygen (S_Δ), was also calculated, where $S_\Delta = \Phi_\Delta/\Phi_T$ [**95**].
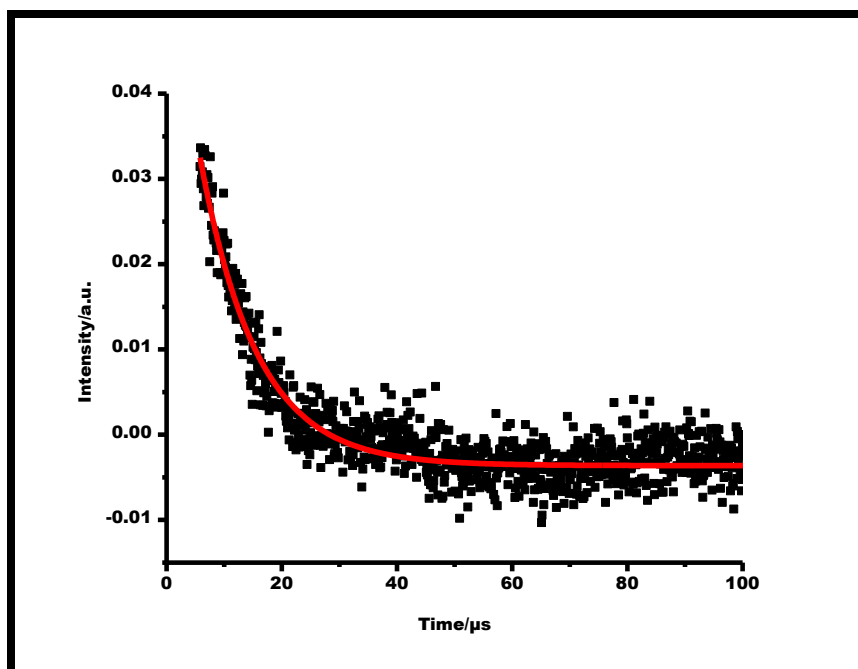
Figure 4.4: Singlet oxygen phosphorescence decay profile of complex 21 in DMSO.

All the complexes studied gave reasonable singlet oxygen quantum yields in DMSO before their conjugation with SiNPs, Table 4.2. Before conjugation, complexes **13** and **15** show the highest singlet oxygen quantum yield of 0.50 each, Table 4.2, followed by

complex **12** with a Φ_Δ value of 0.42. However, the efficiency of energy transfer from the triplet state to triplet state oxygen (S_Δ) is highest in complexes **9**, **11** and **15** with S_Δ values of 0.82, 0.85 and 0.86 respectively.

4.3.1.   Point of Substitution

Carboxyphenoxy Substituted complexes (8-10)

Complexes **8**, **9** and **10** have comparable Φ_Δ (0.30, 0.31 and 0.27 respectively). This suggests that the point of substitution on the Pc ring (α (**8**) vs β (**10**)) and the point of attachment on the phenoxy group (4-position (**9**) vs 3-position (**8** and **10**)) do not have significant impact on the generation of singlet oxygen considering these Pcs.
The efficiency of energy transfer from the triplet state to the triplet state oxygen is lowest for complex **10** (S_Δ = 0.50), showing inefficient energy transfer compared to **8** and **9** (S_Δ = 0.73 and 0.82 for **8** and **9** respectively).
The amide conjugates of complexes **8** and **10** (**8-SiNPs** (linked amide) and **10-SiNPs** (linked amide)) show a decrease in Φ_Δ (0.19 and 0.22 respectively) when compared to **8** and **10** alone (0.30 and 0.27 respectively). However, an increase in Φ_Δ (0.38) was observed for **9-SiNPs** (linked amide) in comparison to **9** alone (0.31). The S_Δ (0.79) value of **9-SiNPs** (linked amide) shows a more efficient energy transfer from the triplet state to $^3O_2$ compared to the S_Δ values of complexes **8-SiNPs** (linked amide) and **10-SiNPs** (linked amide) (0.43 and 0.38 for **8-SiNPs** (linked amide) and **10-SiNPs** (linked amide), respectively).
A decrease in singlet oxygen quantum yield was also observed for the ester conjugates (**8-SiNPs** (linked ester) and **9-SiNPs** (linked ester)) when compared to complexes **8** and **9.** The decrease in Φ_Δ values could be related to <u>screening effect</u>, where the SiNPs prevent the oxygen molecule from interacting with the excited triplet state of the phthalocyanine molecule, depending on the orientation [**198**]. The observed decrease in Φ_Δ also corresponds with low S_Δ values for (**8-SiNPs** (linked ester) and **9-SiNPs** (linked ester)) showing an inefficient energy transfer from the triplet state to the $^3O_2$.

A significant increase in singlet oxygen quantum yield value was observed for **8-SiNPs** (doped) ($\Phi_\Delta = 0.48$) and **9-SiNPs** (doped) ($\Phi_\Delta = 0.47$) compared to complexes **8** ($\Phi_\Delta = 0.30$) and **9** ($\Phi_\Delta = 0.31$) alone. While a slight increase was obtained for **10-SiNPs** (doped) ($\Phi_\Delta = 0.30$) when compared to **10** alone ($\Phi_\Delta = 0.27$), Table 4.2. The increase in Φ_Δ indicates an efficient transfer of energy from the excited triplet state of the Pc to the triplet state oxygen [**199**] and could be attributed to the protection offered by the silica matrix [**107**, **114**].

The Φ_Δ values of the doped nanoparticles (**8-SiNPs** (doped), **9-SiNPs** (doped) and **10-SiNPs** (doped)) are higher when compared to the surface grafted nanoparticles (**8-SiNPs** (linked amide), **9-SiNPs** (linked amide) and **10-SiNPs** (linked amide)). This also indicates that the Pc complexes within the core-shell nanoparticles showed more efficient energy transfer from the triplet state and this was confirmed by the higher S_Δ values obtained for the doped complexes ($S_\Delta = 0.86$ and 0.49 for **8-SiNPs** (doped), and **10-SiNPs** (doped), respectively) compared to the S_Δ values for the amide grafted complexes ($S_\Delta = 0.43$ and 0.38 for (**8-SiNPs** (linked amide) and **10-SiNPs** (linked amide), respectively). No change in S_Δ value was observed for **9-SiNPs** (doped) when compared to S_Δ value of **9-SiNPs** (linked amide).

When the Pcs (**8**, **9** and **10**) and SiNPs are mixed without a chemical bond, a decrease in Φ_Δ is observed for conjugates (0.24 and 0.11 for conjugates **9-SiNPs** (mixed) and **10-SiNPs** (mixed) when compared to the Pc alone (0.31 and 0.27 for complexes **9** and **10** respectively). No change was observed for **8-SiNPs** (mixed).

Aminophenoxy Substituted complexes (11-14)

An increase in Φ_Δ value of **11-SiNPs** (0.40) was observed compared to **11** alone (0.22)**,** Table 4.2, while a decrease was observed in the 1**2-SiNPs** (0.20) hybrid compared to $\Phi_\Delta = 0.42$ for 1**2** alone, corresponding to the trends in Φ_T values. The S_Δ value for complex **11** (0.85) is larger compared to the S_Δ value of complex **12** (0.65), indicating a more

efficient transfer of energy from the triplet state to the $^3O_2$ in complex **11**. A similar trend was observed for their respective conjugates.

For the mixed complexes there was an increase in Φ_Δ values for both **11**-SiNPs (mixed) and 1**2**-SiNPs (mixed).

The Φ_Δ of complex **13** (0.50) is larger when compared to complex **14** (0.31) this corresponds to the trend observed in the triplet quantum yield values, Table 4.2. Both complexes have a 4-aminophenoxy substituent. Complex **13** which has the larger singlet oxygen quantum yield also has a larger triplet quantum yield than complex **14**. No significant changes in Φ_Δ was observed for their respective conjugates (**13-SiNPs** (linked amide) and **14-SiNPs** (linked amide)). Complex **13** (S_Δ = 0.60) also shows a more efficient energy transfer compared to complex **14** (S_Δ = 0.41). A similar trend was also observed for their respective conjugates.

For the mixed complexes there was an increase in Φ_Δ values for both **13-SiNPs** (mixed) and **14-SiNPs** (mixed).

4.3.2.   Amino groups versus Carboxylic groups (9, 11)

In comparing the effect of substituent type on the singlet oxygen quantum yield, complexes **9** (with 4-carboxyphenoxy) and **11** (with 4-aminophenoxy), the Φ_Δ of complex **11** (0.22) is smaller in comparison to complex **9** (0.31), though the reverse was observed for their respective conjugates (0.38 for **9-SiNPs** (linked amide) and 0.40 for **11-SiNPs** (linked amide)), corresponding to trends in Φ_T values. Complex **11** (S_Δ = 0.85) shows a more efficient energy transfer from the triplet state to the $^3O_2$ compared to complex **9** (S_Δ = 0.82), a similar trend was observed for their respective conjugates.

4.3.3.   Amino group versus Aminophenoxy group (14, 15)

In comparing complexes **14** and **15**, both complexes are β substituted with a terminal amino group though **14** has a spacer between Pc ring and the amino group. Complex **14** (0.31) has a lower Φ_{Δ} compared to complex **15** (0.50), the trend does not correspond to the Φ_T values where **14** (0.76) and **15** (0.58). This suggests that <u>the aminophenoxy group prevents interaction with oxygen</u>. A slight increase in singlet oxygen quantum yield was obtained for **15-SiNPs** (linked amide) while a slight decrease was observed for **14-SiNPs** (linked amide) compared to the Pcs alone. The increase in Φ_{Δ} corresponds to a slight increase in Φ_T for **15-SiNPs** (linked amide)). Complex **15** (S_{Δ} = 0.86) shows a more efficient energy transfer from the triplet state to the $^3O_2$ compared to complex **14** (S_{Δ} = 0.41), a similar trend was observed for their respective conjugates.

For the mixed conjugates, **14-SiNPs** (mixed) showed an increase in singlet oxygen quantum yield, while a decrease in Φ_{Δ} was observed for **15-SiNPs** (mixed). Though the Φ_{Δ} of **15-SiNPs** (mixed) decreased it has a more efficient energy transfer compared to **14-SiNPs** (mixed) (S_{Δ} = 0.55).

4.3.4.   Tetra-substitution versus Mono-substitution (11-14)

In comparing the Φ_{Δ} of complexes **11** and **12** (both tetra-substituted with 4-aminophenoxy groups) with complexes **13** and **14** (both mono-substituted with 4-aminophenoxy groups), it was observed that the α mono-substituted complex (**13**) has a larger Φ_{Δ} value compared to the α tetra-substituted complex (**11**), corresponding to Φ_T values. However, the reverse was observed for the β substituted complexes where complex **12** (Φ_{Δ} = 0.42) had the larger Φ_{Δ} value compared to complex **14** (Φ_{Δ} = 0.31), which does not correspond with Φ_T values due to a more efficient energy transfer in **12**. Though complex **13** has a larger Φ_{Δ} value, it is less efficient in transferring energy from the triplet state to the $^3O_2$ compared to complex **11**.

For the conjugates, it was observed that the mono-substituted conjugates (**13-SiNPs** (linked amide) and **14-SiNPs** (linked amide) have a larger Φ_Δ value compared to the tetra-substituted conjugates (**11-SiNPs** (linked amide) and **12-SiNPs** (linked amide)) at both the α and β positions. However, the tetra-substituted conjugates (S_Δ = 0.82 and 0.40 for **11-SiNPs** (linked amide) and **12-SiNPs** (linked amide), respectively) showed a more efficient energy transfer compared to the mono-substituted conjugates (S_Δ = 0.59 and 0.36 for **13-SiNPs** (linked amide) and **14-SiNPs** (linked amide), respectively)

4.3.5.   Clicked complexes (19-21)

The singlet oxygen quantum yields of the clicked complexes were determined to be Φ_Δ = 0.35, Φ_Δ = 0.40 and 0.35 for **19**, **20** and **21** respectively. These values are significantly higher than those obtained for complexes **16**, **17** and **18** alone (Φ_Δ = 0.17, 0.15 and 0.18, respectively), corresponding to an increase in triplet quantum yields. The observed increase in singlet oxygen quantum yields corresponds to higher S_Δ values for complexes **19**, **20** and **21** (S_Δ = 0.49, 0.67 and 0.54 respectively) compared to complexes **16**, **17** and **18** alone (S_Δ = 0.35, 0.37 and 0.47 respectively), showing a more efficient energy transfer from the triplet state to the $^3O_2$ for complexes **19**, **20** and **21**.

A decrease in singlet quantum yield values were observed for the linked conjugates (**19-SiNPs** (linked click), **20-SiNPs** (linked click) and **21-SiNPs** (linked click)) when compared to the Pc complexes alone (**19**, **20** and **21**), corresponding to decrease in triplet quantum yields. Conjugate **19-SiNPs** (linked click) (S_Δ = 0.65) showed a more efficient energy transfer from the triplet state to the $^3O_2$ compared to complex **19** (S_Δ = 0.49) alone.

While conjugates **20-SiNPs** (linked click) and **21-SiNPs** (linked click) (S_Δ = 0.61 and 0.49 respectively) showed a less efficient energy transfer compared to complexes **20** and **21** (S_Δ = 0.67 and 0.54, respectively).

When the Pcs (**19-21**) and SiNPs are mixed without a chemical bond, a slight decrease in singlet quantum yield value was also observed for **19-SiNPs** (mixed) while a slight

increase was observed for **20-SiNPs** (mixed) and **21-SiNPs** (mixed) when compared to the derived Pc complexes alone (**19, 20** and **21**).

The singlet oxygen quantum yield of complex **13** (Φ_Δ = 0.50) is higher compared to complex **19** (Φ_Δ = 0.35) and **21** (Φ_Δ = 0.35) corresponding to their Φ_T values and a more efficient energy transfer in complex **13**. The three complexes are asymmetrical and α substituted with **19** having a 4-((hex-5-ynyl)-benzoate) phenoxy, **21** with a 3-((hex-5-ynyl)-benzoate) phenoxy group while complex **13** has a 4-aminophenoxy group as substituent. Complex **20** (3-((hex-5-ynyl)-benzoate) phenoxy group) displayed a higher singlet oxygen quantum yield compared to complex **14** (with 4-aminophenoxy as substituent)**,** both complexes are asymmetrical and β substituted. The larger Φ_Δ value observed for complex **20** contradicts the Φ_T value due to a more efficient energy transfer to the $^3O_2$ in complex **20** (S_Δ = 0.67).

4.4.   Quantum yield of Internal Conversion (Φ_{ic}) and Intersystem crossing times (τ_{isc})

The values obtained for both the singlet excited state lifetimes (τ_F) and the triplet quantum yields (Φ_T) were used to estimate the intersystem crossing times (τ_{isc}). As expected, the τ_{isc} decreased with increase in Φ_T for all the complexes and conjugates studied.

The quantum yield of internal conversion (Φ_{IC}) was estimated using the equation Φ_{IC} = 1-(Φ_T + Φ_F), the equation assumes that only three processes (fluorescence, intersystem crossing and internal conversion) jointly deactivate the singlet excited states of the Pc complexes and their conjugates.

For the Pc complexes alone, the least energy (<0.1) lost via internal conversion was observed in complexes **13** (Φ_{IC} =0.05) and **19** (Φ_{IC} =0.09) while the most energy lost via internal conversion was observed in complex **11** (Φ_{IC} =0.73)**.** For the conjugates, the least energy lost via internal conversion was observed in **13-SiNPs** (linked amide) (Φ_{IC}

=0.04). Most of the conjugates lost less energy via internal conversion when compared to the Pc complexes alone, though there were a few exceptions which include **12-SiNPs** (linked amide), **19-SiNPs** (linked click), **20-SiNPs** (linked click) and **21-SiNPs** (linked click).

4.5.   Remark on Chapter

The amide conjugates of complexes **8**, **9** and **10** showed improved fluorescence due to the close grafting of the Pcs on the surface of the SiNPs, thereby increasing the efficiency of the fluorescence process. Similar improvement was observed for conjugates of complexes **11, 20** and **21**. The doped conjugates of **8**, **9** and **10** also showed similar improvements due to the protection of the Pc rich core by the outer silica shell. The peripherally substituted complexes generally had higher fluorescence lifetimes compared to their non-peripheral substituted derivatives**.**

The amide conjugates of complexes **8**, **9**, **10**, **11**, **13** and **14** showed a more efficient intersystem crossing process compared to their respective Pcs, while a decrease in Φ_T was observed for **12-SiNPs** (linked amide). A decrease in Φ_T was also observed for all the clicked complexes (**19-SiNPs** (linked click), **20-SiNPs** (linked click) and **21-SiNPs** (linked click)) in comparison to their respective Pcs (**19**, **20** and **21**).

Chapter Five

5.   Nonlinear Optical Studies

This chapter reports on the nonlinear absorption behavior of the phthalocyanine complexes.

5.1.   Nonlinear absorption (NLA) behavior of MPcs: Z scan measurements

This section reports on the findings on the NLA behavior of nine of the complexes studied in this work. The complexes studied for their NLA behavior include **10, 11, 12, 13, 14, 15, 19, 20** and **21**. The NLA behavior of complexes **8**, **9**, **16**, **17** and **18** has been previously studied [**149**]. The studies were carried out only in DMSO. Attempts were also made to study the NLA behavior of the conjugates however, the NLO behavior of the Pcs were not improved in the presence of the SiNPs. This may be due to the strong linear absorption of the conjugates at around 532 nm and also to the photophysical inertness of the SiNPs.

Fig. **5.1A** shows a representative open aperture (OA) Z-scans for complexes (**10, 11, 13, 19 and 20** as examples) at a concentration of 2.09 mM. The curves obtained for all the materials show a strong decrease in transmission which is indicative of reverse saturable absorption (RSA). This is typical of an induced positive nonlinear absorption of the incident light, in this case attributed to excited state absorption. [**128**, **141, 149, 153, 154, 200**]. Fig. **5.1B** is representative of the fitted open-aperture curves. The obtained results for the measurements are summarized in Table 5.1.
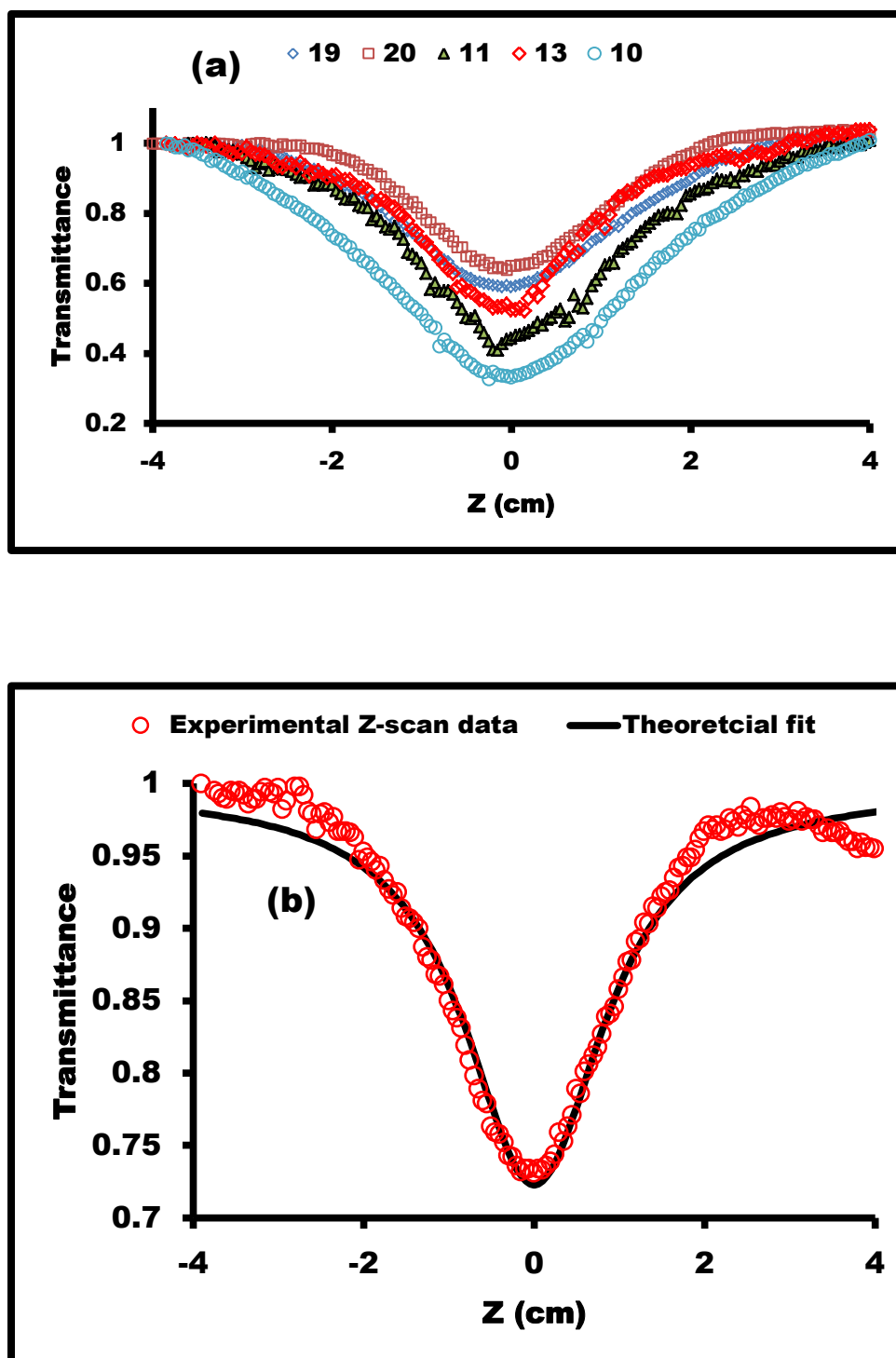
Fig. 5.1(a) Representative open-aperture Z-scans of the phthalocyanine complexes (10, 11, 13, 19 and 20 studied. (b) Open aperture Z-scan for 20 in DMSO showing the fitting. The black solid curve represents the theoretical fit. Concentration = 2.09 mM for (a) and 1.6mM for (b).

Table 5.1: Nonlinear Optical parameters of the studied materials at concentration= ~2.09 mM.

Compounds	Φ_T	β_{eff}(cm/MW)	I_m [$\chi^{(3)}$] /a (esu) $\times 10^{-9}$	γ (esu) $\times 10^{-32}$	I_{lim} (J cm^{-2})
10	0.54	40	14.1	6.68	0.05
11	0.26	22	7.74	3.68	0.19
12	0.65	11	3.87	1.84	0.32
13	0.83	12	4.22	2.01	0.28
14	0.76	21	7.39	3.51	0.21
15	0.58	9.4	3.31	1.57	0.40
19	0.71	11.5	4.05	1.92	0.29
20	0.60	8.0	2.82	1.34	0.44
21	0.65	10.0	3.52	1.67	0.40

Fig. 5.2 shows the open aperture Z-scan curves (using complex **21** as an example) as the energy of the laser beam is varied between 17µJ and 67µJ. It was observed that as the energy of the laser is increased the minimum transmission values were found to drop. This enhancement of the nonlinear absorption reflects the increase in the population of the excited state(s) relative to that of the ground state. This type of behavior is expected of materials showing RSA [**149, 201, 202**]. It has been reported that the nonlinear optical behavior of Pcs is based on RSA mechanisms [**106, 146, 203-205**].
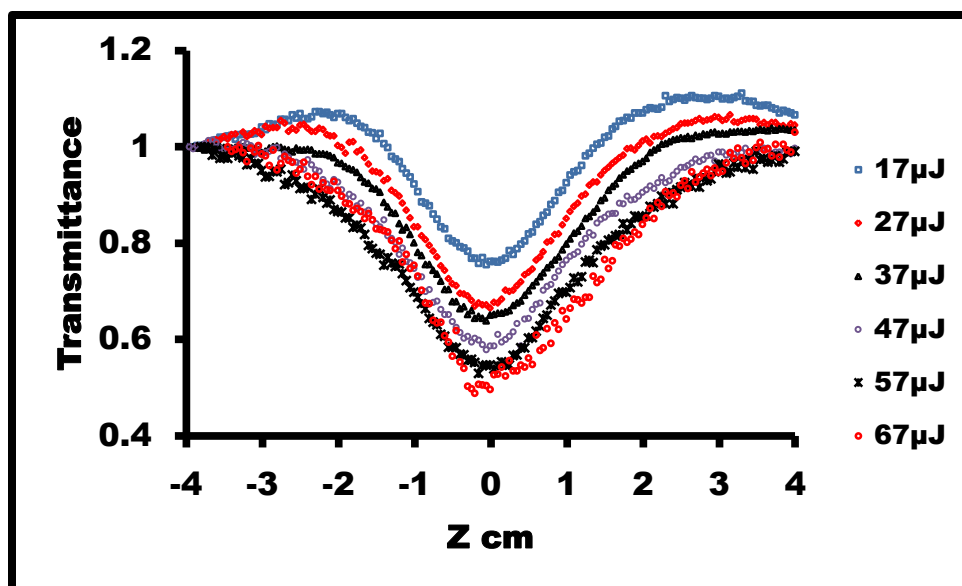
Fig. 5.2: Representative open-aperture Z-scans for complex 21 at energies ranging from 17µJ to 67µJ.

5.2.   Trends in effective nonlinear absorption coefficients (β_{eff})

5.2.1   Point of Substitution

The Z-scan data were analyzed to obtain the effective nonlinear absorption coefficients (β_{eff}) by theoretically fitting the data to the full transmission equations described in the introduction 1.15. The β_{eff} values for the non-peripherally substituted complexes **19** and **21** were slightly higher than the β_{eff} value obtained for peripheral complex **20**. In comparing the data for complexes **11** and **12** (with amino phenoxy groups), the β_{eff} value of complex **11** (non-peripherally substituted) was higher compared to complex **12** (peripherally substituted)**.** However, comparing complex **14** (peripherally substituted and **13** (non-peripherally substituted), the former shows a higher β_{eff} value, contradicting the observations above. The different behavior could be related to the fewer number of amino groups in **13** and **14** compared to **11** and **12.**

5.2.2   Nature of Substituent

In comparing complexes **10** and **12**, the β_{eff} value for complex **10** is higher when compared to **12.** This does not correspond to the triplet quantum yield values which were larger for **12**.

In comparing the β_{eff} values for complexes **14** and **15,** it was observed that complex **15,** which has an amino group closest to the Pc ring, had the lowest β_{eff} value, corresponding to the trend observed in Φ_T values. This could suggest that the spacer between the Pc ring and the amino group has an effect on the β_{eff} value obtained.

5.3.   Trends in third-order nonlinear susceptibility and hyperpolarizability

The imaginary third-order nonlinear susceptibility ($I_m[\chi^{(3)}]$) and second order hyperpolarizability (γ) values are expected to showed similar trend to the β_{eff} values and this was observed in this work, Table 5.1. The values obtained for $I_m[\chi^{(3)}]$ and γ are required to be large due to the fact these parameters determine how quick an optical limiter responds to the agitations initiated by an intense laser beam. The values in Table 5.1 are comparable to those previously reported values for monomeric Pc complexes [**155, 206, 207**].

$I_m[\chi^{(3)}]$ and γ values were larger for α substituted **19** and **21** compared to **20** (β substituted)**,** the same applies to the α substituted complex **11** which gave a larger value than β substituted complex **12** corresponding to β_{eff} values**.** However for complexes **13** and **14,** the α substitution of **13** does not improve the $I_m[\chi^{(3)}]$ and γ values as was the case with the β_{eff} values. Complex **14** shows improved $I_m[\chi^{(3)}]$ and γ. Complex **10** gave the largest $I_m[\chi^{(3)}]$ and γ values. The $I_m[\chi^{(3)}]$ and γ values do not always vary in the same as the Φ_T values.

These observations show that there are other factors contributing to the values of $I_m[\chi^{(3)}]$ and γ in addition to the population of the triplet state.

5.4.   Trends in Optical Limiting

Optical limiting materials have the ability to decrease transmittance with increasing incident fluence. One of the parameters that highlight a good optical limiter is the threshold limiting intensity (I_{lim}), which is defined as the intensity at which one observes a deviation from linear light transmission [124, 208].

Fig. 5.3(A and B) show a plot of incident laser intensity (I_{in}) versus transmitted laser intensity (I_{out}) for all the complexes (10, 11, 12, 13, 14, 15, 19, 20 and 21) studied. It could be clearly observed that all the materials exhibited a deviation from linearity and this is a typical behavior of optical limiters [124, 148, 209]. The limiting threshold fluence values obtained for complexes 10, 11, 13, 14 and 19 (0.05, 0.19, 0.28, 0.21 and 0.29 J cm^{-2} respectively) are comparable to previously reported in literature [210, 211] . The lower the I_{lim} value, the better the material as an optical limiter.

The observed result ties into the values obtained above for γ and [$\chi^{(3)}$], which indicates that complex 10 has the best optical limiting properties when compared to the other complexes studied and this could be due to its bulky substituent (s) compared to the substituent (s) of the other complexes studied. This complex also had the largest $I_m[\chi^{(3)}]$ and γ values.
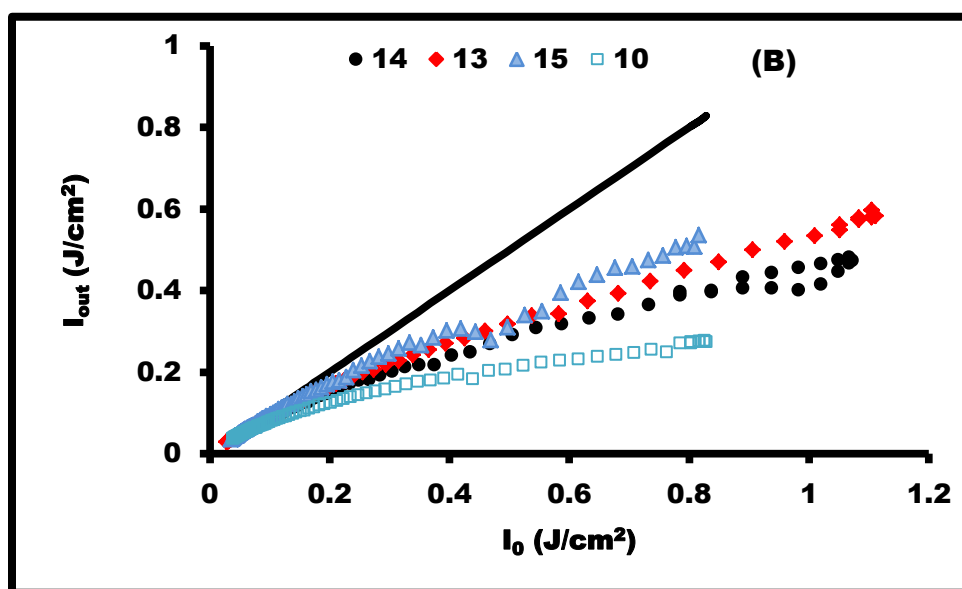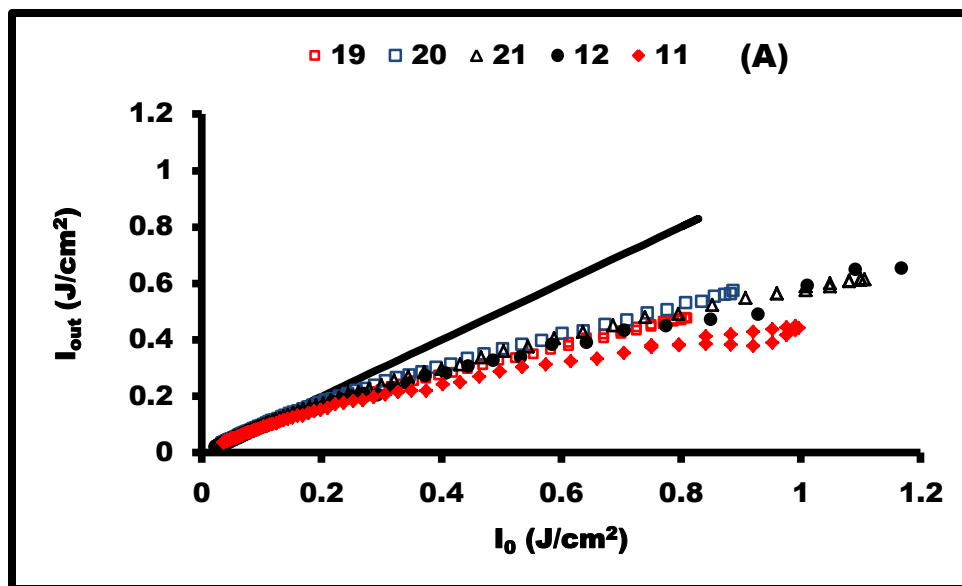
Fig. 5.3: Output fluence (I_{out}) versus input fluence (I_o) plots for compounds 11, 12, 19, 20, 21(A), 10, 13, 14 and 15 (B) respectively at a concentration of ~2.09 mM. The black solid represents a case of linear transmission.

5.5.   Mechanism for NLO

A plot of effective nonlinear absorption coefficients (β_{eff}) versus concentration showed an increase in β_{eff} as the concentration is increased and this was observed for all the samples, Fig. 5.4 (which shows a representative plot for the complexes studied). The increase in β_{eff} values as concentration increases implies that the β_{eff} is strongly dependent on the active species in the excited state species [**209, 210**].
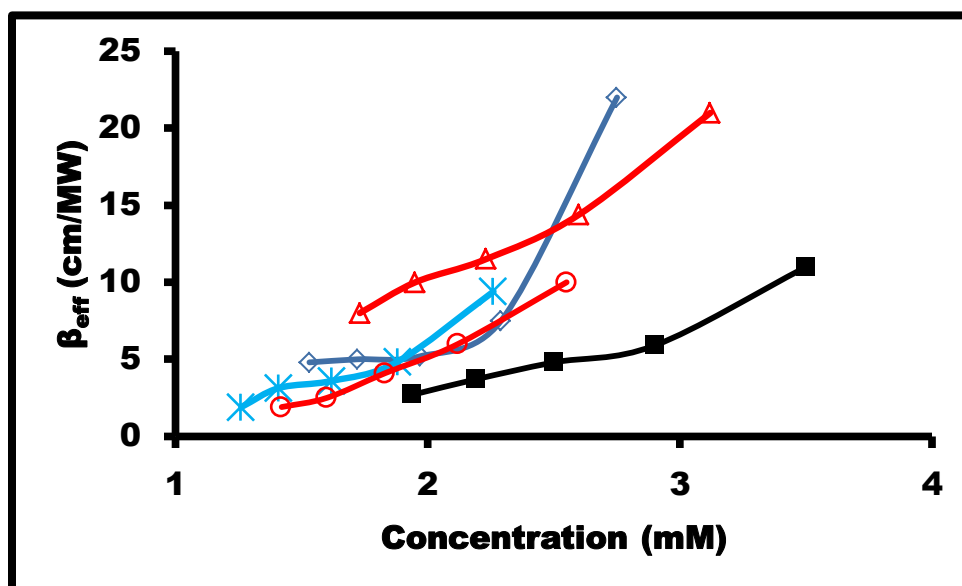
Fig. 5.4: Representative plots showing the concentration dependence on β$_{eff}$ for the phthalocyanine complexes. Each data point represents an independent open aperture Z-scan. 11 (□), 12 (■), 14 (∆), 15 (ж) and 21 (○).

To confirm the NLO behavior of the complexes in response to variation in laser intensities, the transmittance was plotted against input fluence (I_o), Fig. 5.5. Similar curves are observed for the rest of the complexes. There is an exponential decrease in transmittance as the I_o is increased and this type of response is typical of two photon absorbers [**149, 209, 210, 212**].
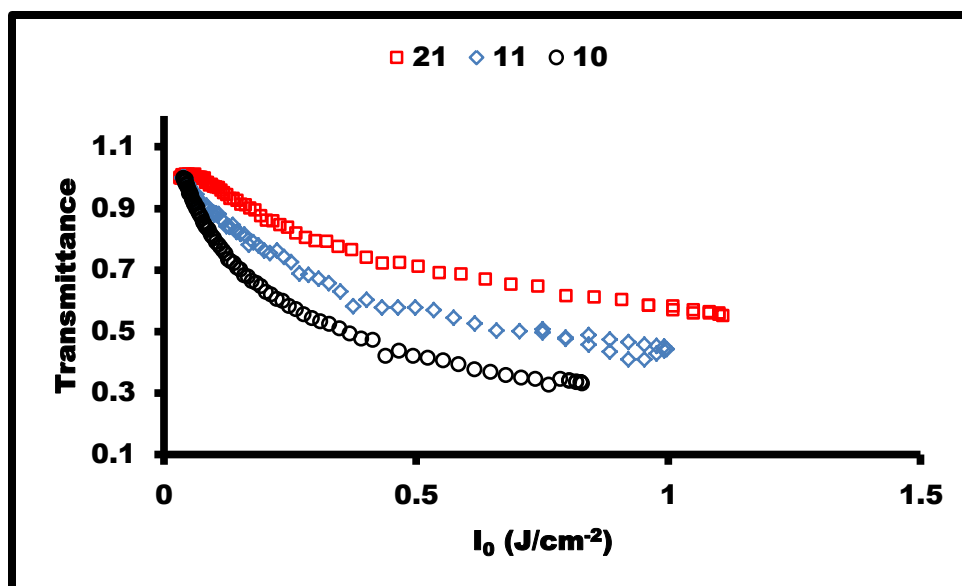
Fig. 5.5: Representative transmission versus input fluence (I_o) curves for the phthalocyanine complexes 10, 11 and 21 studied at a concentration of ~2.09mM for each measurement.

Reverse saturable absorption (RSA) was proven to be the main mechanism by fitting a plot of ln (I_{in}/I_{out}) versus ($I_{in}-I_{out}$), Fig. 5.6. As previously reported, the linear nature of the graph is a clear indication that RSA is the main mechanism causing optical limiting in the studied samples [**213, 214**]. The $\tau_{isc,}$ Table 4.2, obtained for all the phthalocyanine complexes and conjugates are of the same order as the pulse width (10 nm) of the nanosecond laser used for the nonlinear optical measurements and non linear transimissions. It has been stated that, when the laser pulse width is comparable to the τ_{isc} values, Z-scans contributions are from both the triplet and the singlet excited states [**122, 149**]. Thus, the non-linear absorption measurements obtained on the Z-scan in this work are contributions from both the triplet and singlet excited states, since τ_{isc} values are comparable to the pulse width.
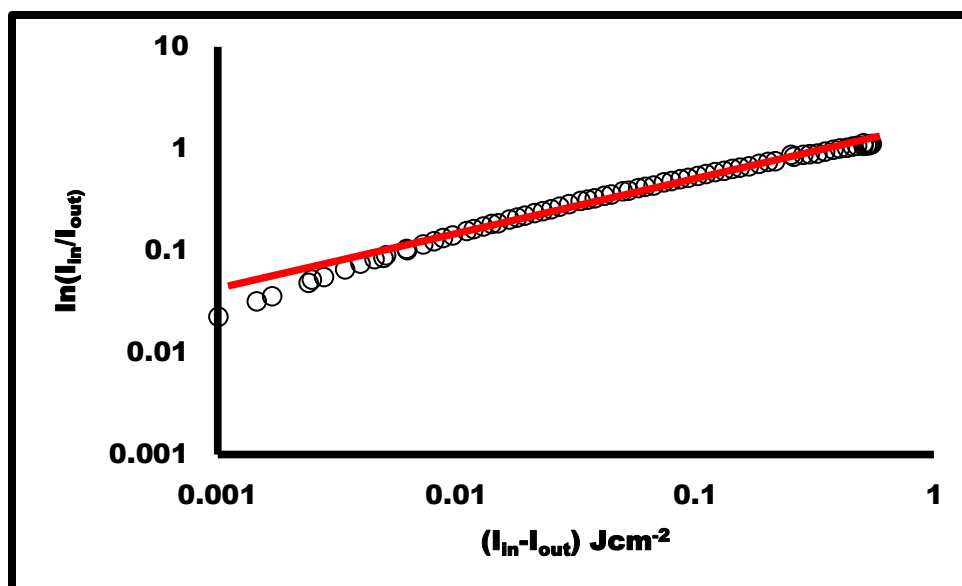
Fig. 5.6: Plot of ln (I_{in}/I_{out}) versus (I_{in}/I_{out}) for complex 10 at a concentration of 2.09mM indicating RSA as the main mechanism.

5.6.   Remark on Chapter.

All the complexes studied showed a reverse saturable absorption behavior. Two of the symmetrical complexes (**10** and **11**) showed better NLO behavior compared to complex **12**. For the asymmetrical complexes studied, complex **14** showed a better NLO behavior compared to other asymmetrical complexes (**13**, **15**, **19-21**). It was observed that the non-linear absorption measurements obtained are contributions from both the triplet and singlet excited states

Complex **10** had the lowest threshold limiting intensity (I_{lim}) implying that it has the best optical limiting property compared to the other complexes studied.

Chapter Six

6.   Dissolution Studies

This chapter reports on the behavior of the phthalocyanine silica nanoparticle conjugates in a simulated biological media.

6.1.   Dissolution studies in artificial lysosomal fluid (ALF)

An investigation of the fate of Pc-SiNP conjugates, including aggregation and dissolution, was carried out in artificial lysosomal fluid (ALF). Card and co-worker showed that the respiratory system especially the lung is vulnerable to the potential toxic effects of nanoparticles as a result of their inhalation [215]. ALF is similar to the fluid that inhaled particles would come into contact after phagocytosis by alveolar and interstitial macrophages in the lung [170, 215, 216]. As highlighted in Table 3.1, the nanoparticles employed in this work were generally less than 60 nm, though slight increase in size was observed on conjugation to Pcs, Fig 3.9. The tendency remains that the respiratory system is susceptible to these nanoparticles.

The dissolution studies were conducted using inductively coupled plasma optical emission spectrometry (ICP-OES). SiNPs were incubated in ALF solution for up to 96 h at 38 °C and concentrations of 0.2 or 2 mg/mL, Table 6.1.

Conjugates **8-SiNPs** (linked ester) and **8-SiNPs** (linked ester) are presented as representatives of the conjugates studied. At certain periods (6, 24, 48, 72 and 96 h) about 4 mL of the nanoparticle-biological fluid solution was taken and filtered by a syringe through a 0.2 µm filter and centrifuged to remove nanoparticles and aggregates that were not dissolved. The filtered and centrifuged solutions were digested in aqua-regia analyzed by ICP-OES.

From Table 6.1, it was observed that the concentration of silicon in solution increased with the incubation period of the SiNPs in ALF. This indicates that the solubility of SiNPs increases in the artificial lysosomal fluid with time, which is in agreement with studies reported in literature [217-219]. The conjugates showed similar trend regardless of the concentration or linkage utilized.

Table 6.1: Concentration of Silicon in incubated biological fluid as determined by ICP-OES in duplicates.

Conjugate	Incubation time (h)				
	6 h	24 h	48 h	72 h	96 h
	Si Concentration (ppm)				
8-SiNPs (linked ester)[a]	18.29	27.22	42.00	57.09	61.88
8-SiNPs (linked amide)[b]	1.72	2.76	4.03	6.00	19.08

[a]**Conjugate concentration= 2 mg/mL.** [b]**Conjugate concentration = 0.2 mg/mL.**

6.2.   Aggregation studies of Pc-SiNPs conjugate in ALF

The level of aggregation and change in size of the incubated Pc-SiNPs were monitored during the period of incubation. Fig. 6.1 shows the TEM images of **8-SiNPs** (linked amide) deposited from the ALF buffer after incubation for a period of 6 h to 96 h. It was observed that the level of aggregation did not change significantly throughout the period of incubation. Similar patterns were observed for **8-SiNPs** (linked ester) conjugate.
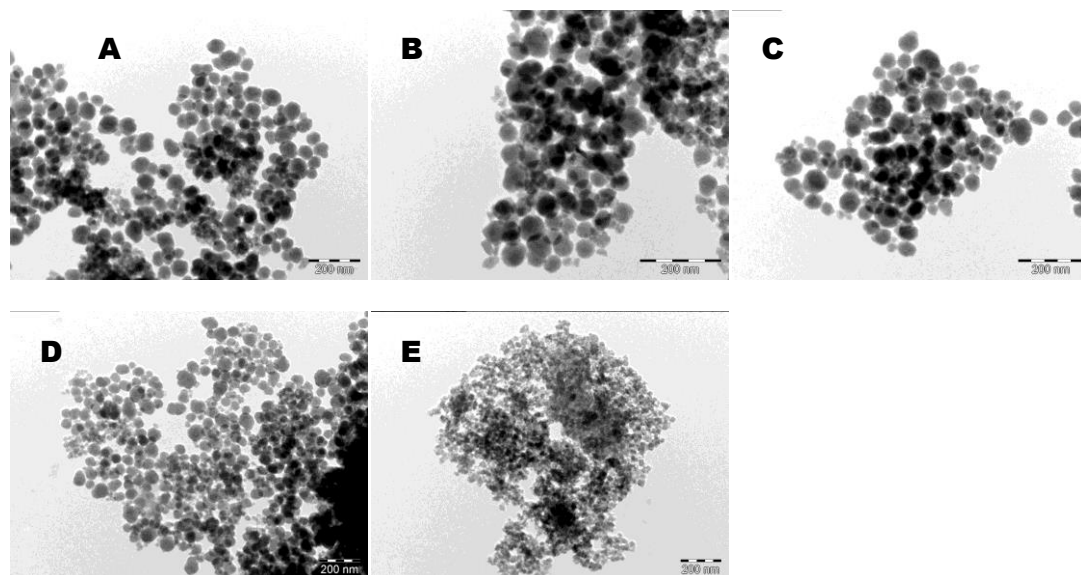
Fig. 6.1: TEM images of 8-SiNPs (linked amide) deposited from the ALF buffer at (A) 6, (B) 48, (C) 72 and (D) 96 h incubation time periods. (E) represents the image of 8-SiNPs (linked ester) after a 96 h incubation time period.

7.   Conclusions and future prospects

This chapter gives a summary of the work presented in this thesis and its future prospect.

7.1.   General Conclusions

In this work, the syntheses and spectroscopic characterization of zinc phthalocyanine complexes were carried out. Five of the Zn phthalocyanine complexes utilized are new and were successfully characterized by various techniques that confirmed their relative purity. The comparison of the photophysical and photochemical parameters of the complexes were also achieved with respect to the substituent type, point of substitution on the Pc ring (α versus β) and the number of substituent (tetra versus mono).

The synthesis, functionalization and characterization of silica nanoparticles (SiNPs) were also achieved. The MPcs were successfully conjugated to SiNPs or doped within the matrix of the SiNPs. In addition, the formed conjugates were characterized with various instrumental techniques. The UV-vis spectral properties of all the conjugates reported in this thesis maintained the Q band of the complexes and the shifts in Q bands were generally negligible.

The conjugates that were linked via ester bond or click chemistry showed improvements in fluorescent properties when compared to the MPcs alone. The conjugation of SiNPs containing carboxylic groups to amino containing MPcs via amide bond resulted in a decrease in fluorescent properties of the Pcs. The reverse occurred when carboxylic acid containing MPcs were linked to amino functionalized SiNPs.

The doped conjugates also showed improvements in fluorescent properties, triplet quantum yields and lifetimes. Improvements in singlet oxygen quantum yield were also observed in some of the doped and linked conjugates. For most of the conjugates studied in this work, an improvement in triplet lifetimes occurred.

The nonlinear absorption behavior of the complexes was successful studied and all the complexes studied showed an increase in absorption with input fluence. This behavior is characteristic of reverse saturable absorbers. All the MPcs also exhibited a deviation from linearity which is a typical behavior of optical limiters. Attempts were made to study the nonlinear optical behavior of the conjugates however, the presence of the SiNPs appear to decrease the nonlinearities observed on the MPcs alone.

Optical parameters such as $I_{lim,}$ γ and $[\chi^{(3)}]$ were determined for all the complexes. Complex **10** showed a superior optical limiting ability when compared to the other complexes studied.

The dissolution and aggregation properties of conjugates were also studied successfully in artificial lysosomal fluid and it was found that amount of silicon in solution increased with the time of incubation, though the size of the nanoparticles did not change in a significant way. Also the level of aggregation did not reduce with incubation time.

7.2.   Future Prospects

The ability of the surface grafted conjugates to retain and in some instances improve on the photophysical properties of the phthalocyanine complexes shows that an alternative channel to doping materials could be developed. The optimization of the surface grafted complexes could be exploited in biological studies and as delivery systems.

In future, it would be interesting to see these conjugates doped within electrospun fibers and to study their photocatalytic behavior and see the retention level of their photophysical properties. It would also be of interest to study the complexes that showed good optical properties in thin films.

References

1. C. Feldmann, H. Goesmann, *Angew. Chem. Int. Ed.* 49 (2010) 1362

2. S. Kango, S. Kalia, A. Celli, J. Njuguna, Y. Habibi, R. Kumar, *Prog. Polym. Sci.* 38 (2013) 1232

3. A. Burns, H. Ow, U. Wiesner, *Chem. Soc. Rev.* 35 (2006) 1028

4. M. De, P. S. Ghosh, V. M. Rotello, *Adv. Mater.* 20 (2008) 4225

5. W. Stöber, A. Fink, E. Bohn, *J. Colloid Interface Sci.* 26 (1968) 62.

6. S. Zhu, J. Xiang, X. Li, S. Shen, H. Lu, J. Zhou, W. Xiong, B. Zhang, X. Nie, M. Zhou, K. Tang, G. Li. *Biotechnol. Appl. Biochem.* 39 (2004) 179

7. C. Kneuer, M. Sameti, U. Bakowsky, T. Schiestel, H. Schirra, H. Schmidt, C. Lehr, *Bioconjugate Chem.* 11 (2000) 926

8. D. Luo, E. Han, N. Belcheva, W. M. Saltzman. *J. Controlled Release* 95 (2004) 333

9. M. N. R. Kumar, M. Sameti, S.S. Mohapatra, X. Kong, R. F. Lockey, U. Bakowsky, G. Lindenblatt, H. Schmidt,C. Lehr. *J. Nanosci. Nanotechnol.* 4 (2004) 876

10. W. Tan, K. Wang, X. He, X. J. Zhao, T. Drake, L. Wang, R. P. Bagwe, *Med. Res. Rev.* 24 (2004) 621

11. G. Yao, L. Wang, Y. Wu, J. Smith, J. Xu, W. Zhao, E. Lee, W. Tan, *Anal. Bioanal. Chem.* 385 (2006) 518

12. A. Liberman, N. Mendez, W. C. Trogler, A. C. Kummel, *Surf. Sci. Rep.* 69 (2014) 132

13. A.K. van Helden, J.W. Jansen and A. Vrij, *J. Colloid Interface Sci.* 81 (1981) 354

14. A. van Blaaderen, A. Kentgens, *J. Non-Cryst. Solids* 149 (1992) 161

15. A. van Blaaderen, A. Vrij, *J. Colloid Interface Sci.* 156 (1993) 1

16. L. Wang, K. Wang, S. Santra, X. Zhao, L. Hillard, J. Smith, Y. Wu, W. Tan, *Anal. Chem.* 78 (2006) 646

17. K. Nozawa, H. Gailhanou, L. Raison, P. Panizza, H. Ushiki ,E. Sellier, J. P. Delville, M. H. Delville, *Langmuir* 21 (2004) 1516

18. N. Shimura, M. Ogawa, *J. Mater. Sci.* 42 (2007) 5299

19. I. A. Rahman, P. Vejayakumaran, C. S. Sipaut, J. Ismail, M. Abu Bakar, R. Adnan, C. K. Chee, *Coll. Surf. A* 294 (2007) 102

20. M. Jafarzadeh, I. A. Rahman, C. S. Sipaut, *J. Sol-Gel Sci. Technol.* 50 (2009) 328

21. I.A. Rahman, P. Vejayakumaran, C. S. Sipaut, J. Ismail, C. K. Chee, *Ceram. Int.* 34 (2008) 2059

22. *F.* J. Arriagada, K. Osseo-Asare, *J. Colloids Surf.* 50 (1990) 321

23. *F.* J. Arriagada, K. Osseo-Asare, *J. Colloid and Interface Sci.* 211 (1999) 210

24. C. L. Chang, H. S. Fogler, *Langmuir* 13 (1997) 3295

25. J. Smith, L. Wang, W. Tan, *Trends Anal. Chem. TrAc* 25 (2006) 848

26. L. Wang, W. Zhao, W. Tan, *Nano. Res.* 1 (2008) 99

27. H. Mader, X. Li, S. Saleh, M. Link, P. Kele, O.S. Wolfbeis, *Ann. N. Y. Acad. Sci.* 1130 (2008) 218

28. A. Bitar, N. M. Ahmad, H. Fessi, Abdelhamid Elaissari, *Drug Discovery Today* 17 (2012) 1147

References

29. Y. Jin, A. Li, S. G. Hazelton, S. Liang, C. L. John, P. D. Selid, D. T. Pierce, J. X. Zhao, *Coord. Chem. Rev.* 253 (2009) 2998

30. K. S. Finnie, J. R. Bartlett, C. J. A. Barbe, L. Kong, *Langmuir* 23 (2007) 3017

31. P. Couleaud, V. Morosini, C. Frochot, S. Richeter, L. Raehm, J. O. Durand, *Nanoscale* 2 (2010) 1083

32. S. Bonacchi, D. Genovese, R. Juris, M. Montalti, L. Prodi, E. Rampazzo, M. Sgarzi, N. Zaccheroni, *Top. Curr. Chem.* 300 (2011) 93

33. H. Ow, D. Larson, M. Srivastava, B. Baird, W. Webb, U. Wiesner, *Nano. Lett.* 5 (2005) 113

34. T. Doussineau, S. Trupp and G. J. Mohr, *J. Colloid Interface Sci.* 339 (2009) 266

35. J. Peng, X. He, K. Wang, W. Tan, Y. Wang, Y. Liu, *Anal. Bioanal. Chem.* 388 (2007) 645

36. S. J. Lee, D. R. Bae, W. S. Han, S. S. Lee, J. H. Jung, *Eur. J. Inorg. Chem.* 10 (2008) 1559

37. S. Bonacchi, E. Rampazzo, M. Montalti, L. Prodi, N. Zaccheroni, F. Mancin, P. Teolato, *Langmuir* 24 (2008) 8387

38. M. Arduini, F. Mancin, P. Tecilla, U. Tonellato, *Langmuir* 23 (2007) 8632

39. . P. Liu, D. Yu, C. Du, B. He, X. Qiu, G. Chen, *Talanta* 81 (2010) 433

40. M. Montalti, E. Rampazzo, N. Zaccheroni, Luca Prodi, *New J. Chem.* 37 (2013) 28

41. S. Santra, K. Wang, R. Tapec, W. Tan, *J. Biomed. Opt.* 6 (2001) 160

42. S. Santra, P. Zhang, K. M. Wang, R. Tapec, W. H. Tan, *Anal. Chem.* 73 (2001) 4988

43. R. Johnston, B. J. Battersby, G. A. Lawrie, M. Trau, *Chem. Commun.* 7 (2005) 848

44. W. Zhong, *Anal. Bioanal. Chem.* 394 (2009) 47

45. L. Wang, W. Zhao, M. B. O'Donoghue, W. Tan, *Bioconjugate Chem.* 18 (2007) 297

46. F. Figueira, J. A. S. Cavaleiro, J. P.C. Tomé, *J. Porphyrins Phthalocyanines* 15 (2011) 517

47. J. L. Vivero-Escoto, Y. T. Huang, *Int. J. Mol. Sci.* 12 (2011) 3888

48. S. Kim, T. Y. Ohulchanskyy, H. E. Pudavar, R. K. Pandey, P. N. Prasad, *J. Am. Chem. Soc.* 129 (2007) 2669

49. K. G. Lee, J. C. Kim, R. Wi, J. S. Min, J. K. Ahn, D. H. Kim, *J. Nanosci. Nanotech.* 11 (2011) 686

50. C. Loo, A. Lowery, N. J. Halas, J. West, R. Drezek, *Nano Lett.* 5 (2005) 709

51. A. M. Gobin, M. H. Lee, N. J. Halas, W. D. James, R. A. Drezek, J. L. West, *Nano Lett.* 7 (2007) 1929

52. X. Ji, R. Shao, A. M. Elliott, R. J. Stafford, E. Esparza-Coss, J .A. Bankson, G. Liang, Z.-P. Luo, K. Park, J. T. Markert, C. Li, *J. Phys. Chem. C* 111 (2007) 6245

53. D. Li , W. Y. Teoh , C. Selomulya , R. C. Woodward , R. Amal , B. Rosche, *Chem. Mater.* 18 (2006) 640

54. C. Shifu, C. Gengyu, *Surf. Coat. Technol.* 200 (2006) 3637

55. K. Guan, *Surf. Coat. Technol.* 191 (2005) 155

56. H. Guo, S. Tao, *Sens. Actuator, A* 123 (2007) 578

57. L.P. Singh, S.K. Bhattacharyya, G. Mishra, S. Ahalawat, *Appl. Nanosci.* 1 (2011) 117

58. I.A. Rahman, M. Jafarzadeh, C.S. Sipaut, *Ceram. Inter.* 35 (2009) 1883

59. L. M. Rossi, L. Shi, F. H. Quina, Z. Rosenzweig, *Langmuir* 21 (2005) 4277

60. S. Brunauer, L. S. Deming, W. E. Deming, E. Teller, *J. Am. Chem. Soc.* 62 (1940) 1723

61. S. Brunauer, P. H. Emmett, E. Teller, *J. Am. Chem. Soc.* 60 (1938) 309

62. J. F. Watts, J. Wolstenholme. *"An introduction to surface analysis by XPS and AES." An Introduction to Surface Analysis by XPS and AES,* pp. 224. ISBN 0-470-84713-1. Wiley-VCH, May 2003.

63. K. Hofmann, I. Kahle, F. Simon, S. Spange, *Beilstein J. Org. Chem.* 6 (2010) 79

64. C. G. Claesens, U. Hahn, T. Torres, *Chem. Rec.* 8 (2008) 75

65. D. Wöhrle, G. Schnurpfeil, S. G. Makarov, A. Kazarin, O. N. Suvorova, *Macroheterocycl.* 5 (2012) 191

66. N. B. Mckeown, Phthalocyanine Materials: Synthesis, Structure, Functions Cambridge Univ. Press, Cambridge, UK, 1998, 30

67. J.D. Spikes, *Photochem. Photobiol.* 43 (1986) 691

68. P. Gregory. *J. Porphyrins Phthalocyanines* 3 (1999) 468

69. P. Gregory. *J. Porphyrins Phthalocyanines* 4 (2000) 432

70. D. Wöhrle, O. Suvorova, R. Gerdes, O. Bartels, L. Lapok, N. Baziakina, S. Makarov, A. Slodek, *J. Porphyrins Phthalocyanines* 8 (2004) 1020

71. E. A. Lukyanets, *J. Porphyrins Phthalocyanines* 3 (1999) 424

72. S. M. O'Flaherty, S. V. Hold, M. J. Cook, T. Torres, Y. Chen, M. Hanack, W. J. Bla *Adv. Mater.* 15 (2003) 19

73. G. Bottari, G. de la Torre, D. M. Guldi, T. Torres, *Chem. Rev.* 110 (2010) 6768

74. J. Mack, M. Stillman, *Coord. Chem. Rev.* 219 (2001) 993

75. A. Henrikson, M. Soundbom, *Theor. Chim. Acta* 27 (1972) 213

76. L. Edwards, M. Gouterman, *J. Mol. Spectrosc.* 33 (1970) 292

77. M. Gouterman, in *The Porphyrins, Part A. Physical Chemistry*, D. Dolphin (Ed) Academic Press, New York, Vol. 3 (1978) P1-165

78. A. J. McHugh, M. Gouterman, C. Weiss, *Theoret. Chim. Acta.* 24 (1987) 246

79. A. M. Schaffer, M. Gouterman, E. R. Davidson, *Theoret. Chim. Acta.* 30 (1973) 9

80. F. Dumoulin, M. Durmuş, V. Ahsen, T. Nyokong, *Coord. Chem. Rev.* 254 (2010) 2792.

81. V. N. Nemykin, E. A. Lukyanets, *ARKIVOC* I (2010) 136

82. N. B. Mckeown, J. Painter, *J. Mater. Chem.* 4 (1994) 1153

83. L. F. Levey, H. Stephen, *J. Chem. Soc.* (1931) 79

84. C.C. Leznoff, C.R. McArthur, Y. Qin, *Can. J. Chem.* 71 (1993) 1319.

85. S.V. Kudrevich, H. Ali, J.E. van Lier, *J. Chem. Soc. Perkin Trans.* 1 (1994) 2767

86. T. Torres, *J. Porphyrins Phthalocyanines* 4 (2000) 325

87. N. Kobayashi, R Kondo, S Nakajima, T. J. Osa, *Am. Chem. Soc.* 112 (1990) 9640

88. A. Weitemeyer, H. Kliesch, D. Wohrle, *J. Org. Chem.* 60 (1995) 4900

89. C. Allen, W. M. Sharman, J. E. Van Lier, *J. Porphyrins Phthalocyanines* 5 (2001) 161

90. J. R. Lakowicz, Principles of Fluorescence Spectroscopy, 3rd ed., Springer Science Business Media, LCC, New York, 2006

91. K. Ishii, N. Kobayashi, In The Porphyrin Handbook, eds., K.M. Kadish, K.M. Smith, R. Guilard, Elsevier Sc., USA, Vol. 16 (2003) 1, Chp.102

92. B. Valeur, Molecular Fluorescence, Wiley-VCH Publishers, 2002

93. S. Dhami, A. J. Demello, G. Rumbles, S. M. Bishop, D. Phillips, A Beeby, *Photochem. Photobiol.* 61 (1995) 341

94. S. Fery-Forgues, D. Lavabre, *J Chem Educ* 76 (1999) 1260

References

95. A. Ogunsipe, J. Y. Chen, T. Nyokong, *New J Chem* 28 (2004) 822

96. T. H. Tran-Thi, C. Desforge , C. Thiec, S. J. Gaspard, *Phys Chem* 93 (1989) 1226

97. R. A Keller, S. G Hadley, *J. Chem. Phys*. 42 (1965) 2382

98. T. Nyokong, *Pure Appl. Chem.* 83 (2011) 1763

99. V. V. Bryukhanov, B. F. Minaev, A. S. Kusenova, S. G. Karstina, *J. Appl. Spec.* 56 (1992) 146

100. T. Nyokong, *Coord. Chem. Rev.* 251 (2007) 1707

101. L. I. Grossweiner (Ed.), The Science of Phototherapy, CRC Press, Boca Rota, 1994

102. Peter Meisel, Thomas Kocher, *J. Photochem. Photobiol. B*: 79 (2005) 159

103. M. Niedre, M. S. Patteerson, B. C. Wilson, *Photochem. Photobiol.* 75 (2003) 382

104. M. S. Patterson, S. J. Madsen, R. Wilson, *J. Photochem. Photobiol. B*: 5 (1990) 69

105. N. Kuznetsova, N. Gretsova, E. Kalmykova, E. Makarova, S. Dashkevich, V. Negrimovskii, O. Kaliya, E. Lukyanets, *Russ. J. Gen. Chem.* 70 (2000) 133

106. L. De boni, E. Piovesan, L. Gaffo. C. R. Mendonca. *J. Phys. Chem. A*. 112 (2008) 6803

107. R. Lin, L. Zhou, Y. Lin, A. Wang, J.H. Zhou, S.H. Wei *Spectroscopy* 26 (2011) 179.

108. F. Wang, X. L. Chen, Z. X. Zhao, S.-H. Tang, X.Q. Huang, C.H. Lin, C.B. Cai, N.F. Zheng, *J. Mater. Chem.* 21 (2011) 11244

109. B. Zhao, J. J. Yin, P. J. Bilski, C. F. Chignell, J. E. Roberts, Y. Y. He, *Toxicol. Appl. Pharmacol.* 241 (2009) 163

110. H. J. Kim, K. J. Shin, M. K. Han, K. An, J. K. Lee, I. Honma, H. Kim, *Scr. Mater.* 61 (2009) 1137

111. Q. F. Zhuang, J. E. Wang, Z. J. Zhu, F. Feng, Z. X. Wang, *Chin. J. Anal. Chem.* 39 (2011) 1567

112. N. B. Sul'timova, P. P. Levin, A. V. Lobanov, A. M. Muzafarov, *High Energy Chemistry* 47 (2013) 98

113. K. Sathiyamoorthy, C. Vijayan, S. Varma, *Langmuir* 24 (2008) 7485

114. T. H. Kim, J. K. Lee, W. H. Park, T. S. Lee, *Mol. Cryst. Liq. Cryst.* 444 (2006) 23

115. M. A. García-Sánchez, F. Rojas-González, E. C. Menchaca-Campos, S. R. Tello-Solís, R. I. Y. Quiroz-Segoviano, L. A. Diaz-Alejo, E. Salas-Bañales, A. Campero *Molecules* 18 (2013) 588

116. H. S. Qian, H. C. Guo, P. C. Ho, R. Mahendran, Y. Zhang, *Small* 5 (2009) 2285

117. D. K. Chatterjee, Y. Zhang, *Nanomedicine* 3 (2008) 73

118. X. L. Chen, J. L. Zou, T. T. Zhao, Z. B. Li, *J. Fluoresc.* 17 (2007) 235

119. J. l. Zou, X.l. Chen, *Microchem. J.* 86 (2007) 42

120. Y. R. Shen, *The Principles of Nonlinear Optics* (Wiley, New York 1984)

121. R. W. Boyd, *Nonlinear Optics*, 2nd edn. (Academic, San Diego 2003)

122. T. Pritchett, *Models for Saturable and Reverse Saturable Absorption in Materials for Optical Limiting (*No. ARL-TR-2567) Army Research Lab White Sands Missile Range NM, (2002).

123. L. De Boni, D. S. Corrêa, C. R. Mendonça. "*Nonlinear Optical Absorption of Organic Molecules for Applications in Optical Devices.*" InTech (2010).

124. L. W. Tutt, T. F. Boggess, *Prog. Quantum Electron* 17 (1993) 299

125. G. Banfi, V. Degiorgio, D. Richard, *Adv. Phys.* 47 (1998) 447

126. G. S. He, L. S. Tan, Q. Zheng, P. N. Prasad, *Chem. Rev.* 108 (2008) 1245

127. D. Dini, M. Barthel, M. Hannack, *Eur. J. Org.* 20 (2001) 3759

128. J. W. Perry, K. Mansour, S. R. Marder, K. J. Perry, D. Alvarez, I. Choong, *Opt. letters.* 19 (1994) 625

129. P. C. Ray, *Chem. Rev.* 110 (2010) 5332

130. T. H. Wei, D. J. Hagan, M. J. Sence, E. W. Van Stryland, J.W. Perry, D. R. Coutler, *Appl. Phys.* B51 (1992) 46

131. G. L. Wood, M. J. Miller, A. G. Mott, *Opt. lett.* 20 (1995) 973

132. L. W. Tutt, A. Kost, *Nature* 356 (1992) 225.

133. R. T. Tom, A. S. Nair, N. Singh, M. Aslam, C. L. Nagendra, R. Philip, K. Vijayamohanan, T. Pradeep, *Langmuir* 19 (2003) 3439

134. L. Vivien, E. Anglaret, D. Richl, F. Bacou, C. Journet, C. Goze, M. Andrieux, M. Brunet, P. Bernier, F. Hache, *Chem. Phy. Lett.* 307 (1999) 317

135. Y. P. Sun, J. E. Riggs, H. W. Rollins, R. Guduru, *J. Phys. Chem. B* 103 (1999) 77

136. S. M. O'Flaherty, S. V. Hold, M. J. Cook, T. Torres, Y. Chen, M. Hanack, W. J. Blau, *Adv. Mat.* 15 (2003) 20

137. J. L. Bredas , C. Adant , P. Tackx , A. Persoons , B. M. Pierce, *Chem. Rev.* 94 (1994) 243

138. Y. Fainman, J. Ma, S.H. Lee, *Mater. Sci. Rep.* 9 (1993) 53

139. B. E. A Saleh, M. C. Teieh, *Fundamentals of Photonics*, Wiley: New York 1991

140. M. Sheik-Bahae, A.A. Said, E.W. Stryland, *Opt. Lett.* 14 (1989) 955

141. M. Sheik-Bahae, A.A. Said. T. Wei, D.J. Hagan, E.W. Van Stryland, *IEEE J. Quant. Elect.* 26 (1990) 760

142. C. G. Claessens, W. J. Blau, M. Cook, M. Hanack, R. J. M. Nolte, T. Torres, D. Wohrle, *Monatshefte für Chemie.* 132 (2001) 3

143. G. de la Torre, P. Vazquez, F. Agullo-Lopez, T. Torres, *Chem. Rev.* 104 (2004) 3723

144. M. Yüksek, A. Elmali, M. Durmuş, H G. Yaglioglu, H. Ünver, T. Nyokong, *J. Opt.* 12 (2010) 015208

145. J. S. Shirk, R. G. S. Pong, F. J. Bartoli, A. W. Snow, *J. Appl. Phys. Lett.* 63 (1993) 1880

146. J. W. Perry, K. Mansour, I. Y. S. Lee, X. L. Wu, P. V. Bedworth, C. T. Chen, D. Ng, S. R. Marder, P. Miles, T. Wada, M. Tian, H. Sasabe, *Science* 273 (1996) 1533

147. J. S. Shirk, R. G. S. Pong, S. R. Flom, H. Heckmann, M. Hanack, *J. Phys. Chem. A.* 104 (2000) 1438

148. Y. Chen, M. Hanack, Y. Araki, O. Ito, *Chem. Soc. Rev.* 34 (2005) 517

149. Y. Li, T. M. Pritchett, J. Huang, M. Ke, P. Shao, W. Sun, *J. Phys. Chem. A.* 112 (2008) 7200

150. S. O. Sanusi, E. Antunes, T. Nyokong, *J. Porphyrins Phthalocyanines* 17 (2013) 920

151. S. J. Mathews, S. C. Kumar, L. Giribabu, S. V. Rao, *Opt. Commun.* 280 (2007) 206

152. S. V. Rao, P. T. Anusha, T. S. Prashant, D. Swain, S. P. Tewari, *Mater. Sci. Appl.* 2 (2011) 299

153. E.W. Van Stryland, M. Sheik-Bahae, in: Characterization Techniques and Tabulations for Organic Nonlinear Materials, M.G. Kuzyk and C.W. Dirk, Eds., Marcel Dekker, Inc. (1998) pp. 655-692.

154. M. Hanack, T. Schneider, M. Barthel, J.S. Shirk, S.R. Flom, R.G.S. Pong, *Coord. Chem. Rev.* 235 (2001) 219

155. D. Dini, M. Hanack, In the Porphyrin Handbook: Physical Properties of Phthalocyanine-Based Materials; K. M. Kadish, K. M. Smith, R. Guilard, Eds; Academic Press: USA. (2003) Vol 17 pp 22-31.

156. W. Stopford, J. Turner, D. Cappellini, T. Brock, *J. Environ. Monit*. 5 (2003) 675

157. X. F. Zhang, Y. Di, F. Zhang, *J. Photochem. Photobiol. A:* 203 (2009) 216

158. C. Xia, Y. Wang, W. Chen, W. Yu, B. Wang, T. Li, *Mol.* 16 (2011) 1389

159. G. K. Karaoglana, G. Gümrükçü, A. Koca, A. Gül, *Dyes Pigm.* 88 (2011) 247

160. S. D' Souza, E. Antunes, T. Nyokong, *Inorg. Chim. Acta* 367 (2011) 173

161. S. D' Souza, E. Antunes, C. Litwinski, T. Nyokong, *J. Photochem. Photobiol. A*: 220 (2011) 11

162. Y. An, M. Chen, Q. Xue, W. Liu, *J. Col. Inter. Sci.* 311 (2007) 507

163. M. Ortega-Munoz, J. Lopez-Jaramillo, F. Hernandez-Mateo, F. Santoyo-Gonzalez, *Adv. Synth. Catal.* 348 (2006) 2410

164. B. Malvi, B. R. Sarkar, D. Pati, R. Matthew, T. G. Ajithkumar, S. S. Gupta, *J. Mater. Chem.* 19 (2009) 1409

165.   Campidelli, B. Ballesteros, A. Filoramo, D. D. Dı´az, G. de la Torre, T. Torres, G. M. A. Rahman, C. Ehli, D. Kiessling, F. Werner, V. Sgobba, D. M. Guldi, C. Cioffi, M. Prato, J. P. Bourgoin, *J. Am. Chem. Soc.* 130 (2008) 11503

166.   Z. Guo, A. Lei, X. Liang, Q. Xu, *Chem. Commun.* 43 (2006) 4512

167.   R. P. Bagwe, C. Yang, L. R. Hilliard, W. Tan, *Langmuir* 20 (2004) 8336

168.   L. V. Stebounova, E. Guio, V. H. Grassian, *J Nanopart Res* 13 (2011) 233

169.   G. Nallathambi, T. Ramachandran, V. Rajendran, R. Palanivelu, *Mater. Res.* 14 (2011) 552

170.   R.M. Silverstein, G.C. Bassler, T.C. Morrill, Spectrometric Identification of Organic Compounds, 4th ed., John Wiley and Sons, New York, 1981.

171.   B. Malvi, B. R. Sarkar, D. Pati, R. Matthew, T. G. Ajithkumar, S. S. Gupta, *J. Mater. Chem*. 19 (2009) 1409

172.   S. F. Wang, Y. F. Hsua, T. Yanga, C. M. Changa, Y. Chena, C. Y. Huang, F. S. Yen. *Materials Science and Engineering A* 395 (2005) 148

173.   L.C. Klein, *Ann. Rev. Mater. Sci.* 15 (1985) 227

174.   J. Mack, M. J. Stillman. *J. Am. Chem. Soc*. 116 (1994) 1292

175.   T. T. Tasso, Y. Yamasaki, T. Furuyama, N. Kobayashi, *Dalton Trans*. 43 (2014) 5886

176.   J. F. B.Barata, A. L. Da-Silva, M. Garcia, P. M. S. Neves, J. A. S. Cavaleiro, T. Trindade, *RSC. Adv.* 3 (2013) 274

177.   E. Herz, T. Marchincin, L. Connelly, D. Bonner, A. Burn, S. Switalski, U. Wiesner, *J. Fluoresc.* 20 (2010) 67.

178. E. Secret, M. Maynadier, A. Gallud, M. Gary-Bobo, A. Chaix, E. Belamie, P. Maillard, M. J. Sailor, M. Garcia, J.-O. Durand, F. Cunin, *Chem. Commun.* 49 (2013) 4202

179. O. Hocine, M. Gary-Bobo, D. Brevet, M. Maynadier, S. Fontanel, L. Raehm, S. Richeter, B. Loock, P. Couleaud, C. Frochot, C. Charnay, G. Derrien, M. Smaihi, A. Sahmoune, A. Morere, P. Maillard, M. Garcia, J.O. Durand, *Int. J. Pharm.* 402 (2010) 221

180. R. Zugle, C. Litwinski, N. Torto, T. Nyokong, New J. Chem. 35 (2011) 1588.

181. N.E. Triggs, J. J. Valentini, *J. Phys. Chem.* 96 (1992) 6922.

182. D. Gani, P. J. Hendra, W. F. Maddams, C. Passingham, I. A. M. Royaud, H. A. Willis, V. Zichy, M. E. A. Cudby, *Analyst* 115 (1990) 1313

183. A.W. Snow, J.R. Griffith, N.P. Marullo, *Macromolecules* 17 (1984) 1614

184. S. Lowell, J. E. Shields. *Powder surface area and porosity.* Vol. 2. Springer, 1991.

185. S. Xu, S. Hartvickson, J. X. Zhao, *ACS Appl. Mater. Interfaces* 3 (2011) 1865

186. J. A. Lacey, D. Phillips, *Photochem. Photobiol. Sci.* 1 (2002) 378

187. P. R. Barber, S. M. Ameer-Beg, J. Gibey, L. M. Carlin, M. Keppler, T. C. Ng, B. Vojnovic, *J. R. Soc. Interface.* 6 (2009) S93

188. S. Z. Topal, Ü. İşci, U. Kumru, D. Atilla, A. G. Gürek, C. Hirel, M. Durmuş, J. B. Tommasino, D. Luneau, S. Berber, F. Dumoulin, V. Ahsen, *Dalton Trans.* 43 (2014) 6897

189. F. Gao, X. Chen, Q. Ye, Z. Yao, X. Guo, L. Wang. *Microchim. Acta.* 172 (2011) 327

190. S. Shimizu, A. Miura, N. Kobayashi, *Cryst. Eng. Comm.* 15 (2013) 3759

191. A.Y. Lebedev, M. A. Filatov, A. V. Cheprakov, S. A. Vinogradov, *J. Phys. Chem. A* 112 (2008) 7723

192. J. R. Lakowicz, *Analytical Biochem.* 337 (2005) 171

193. X. F. Zhang, X. Li, L. Niu, L. Sun, L. Liu, *J. Fluoresc.* 19 (2009) 947

194. M. Yamaji, H. Maeda, Y. Nanai, K. Mizuno, *Intern. Scholarly Research Network: Phys. Chem.* 103817 (2012) 7 pages, doi:10.5402/2012/103817

195. J. P. Byrne, E. F. McCoy, I. G. Ross, *Aust. J. Chem.* 18 (1965)1589

196. J. H. Brannon, D. Magde, *J. Am Chem Soc.* 102 (1980) 62

197. A. Grofcsik, P. Baranyai, I. Bitter, V. Csokai, M. Kubinyi, K. Szegletes, J. Tatai, T. Vidoczy, *J. Mol. Struct.* 704 (2004) 11.

198. E. I. Sagun, E. I. Zenkevich, V.N. Knyukshuto, A. M. Shulga, D. A. Starukhin, C. von Borczyskowski , *Chem. Phys.* 275 (2002) 211

199. T. Nyokong, E. Antunes. *Coord. Chem. Rev.* 257 (2013) 2401

200. H. Bertagnolli, W. J. Blau, Y. Chen, D. Dini, M. P. Feth, S. M. O'Flaherty, M. Hanack, V. Krishnan. *J. Mater. Chem.* 15 (2005) 683

201. X. L. Zhang, Z. B. Liu, X. C. Li, Q. Ma, X. D. Chen, J. G. Tian, Y. F. Xu, Y. S. Chen. *Opt. Express.* 21 (2013) 7511

202. C. R. Guliano, L. D. Hess, *IEEE J. Quant. Electron.* 3 (1967) 358

203. F. E. Hernandez, S. Yang, E. W. Van Stryland, D. J. Hagan. *Opt. Lett.* 25 (2000) 1180

204. M.C. Larciprete, R. Ostuni, A. Belardini, M. Alonzo, G. Leahu, E. Fazio, C. Sibilia, M. Bertolotti, *Phot. Nano. Fund. Appl.* 5 (2007) 73

205. S. Tekin, U. Kürüm, M. Durmuş, H. G. Yaglioglu, T. Nyokong, A. Elmali, *Opt. Comm.* 283 (2010) 4749

206. J. Britton, C. Litwinski, T. Nyokong, *J. Porphyrins Phthalocyanines* 15 (2001) 1239

207. K. E. Sekhosana, E. Amuhaya, J. Mack, T. Nyokong, *J. Mater. Chem. C.* 2 (2014) 5431

208. J. Britton, M. Durmus, V. Chauke, T. Nyokong. *J. Mol. Struct.* 1054-1055 (2013) 209

209. R. L. Sutherland, Handbook of Nonlinear Optics, 2nd Ed., Marcel Dekker Inc, NY, 2003.

210. K. Sanusi, E. Antunes, T. Nyokong, *Dalton Trans*. 43 (2014) 999

211. K. E. Sekhosana, E. Amuhaya, T. Nyokong, *Polyhedron.* 85 (2015) 347

212. G. J. Zhou, W.Y. Wong, *Chem. Soc. Rev.* 40 (2011) 2541

213. Y. Kojima, T. Matsuoka, N. Sato, H. Takahashi. *Macromolecules.* 28 (1995) 2893

214. B. Aneeshkwnar, P. Gopinath, C. P. G. Vallabhan, V. P. N. Nampoori, P. Radhakrishnan, *J. Opt. Soc. Am. B*. 20 (2003) 1486.

215. W. Card, D. C. Zeldin, J. C. Bonner, E. R. Nestmann, *Am. J. Physiol. Lung Cell Mol. Physiol*. 295 (2008) L400

216. M. Philip Beeston, J. T. van Elteren, V. S. Šelih, R. Fairhurst, *Analyst* 135 (2010) 351

217. S. Quignard, G. Mosser, M. Boissière, T. Coradin, *Biomaterials* 33 (2012) 4431

218. K. Finnie, D. Waller, F. Perret, A. Krause-Heuer, H. Lin, J. Hanna, B. Christophe, *J Sol-Gel Sci. Technol.* 49 (2009) 12

219. J.D. Bass, D. Grosso, C. Boissière, T. Coradin, C. Sanchez, *Chem. Mater.* 19 (2007) 4349